Investigation of Microscopic Structures in the Low-Energy Electric Dipole Response of ^{120}Sn using Consistent Experimental and Theoretical Observables
and
Digital Signal Processing for Nuclear Physics Experiments

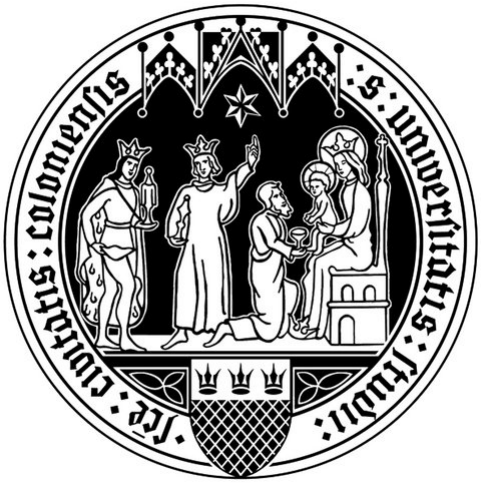

Inaugural-Dissertation
zur
Erlangung des Doktorgrades der
Mathematisch-Naturwissenschaftlichen Fakultät
der Universität zu Köln

vorgelegt von
Michael Weinert
aus Mechernich

Universität zu Köln
2022

Gutachter:	Prof. Dr. Andreas Zilges
	Prof. Dr. Peter Reiter
Tag der mündlichen Prüfung:	8.12.2022

Diese Arbeit wurde von der Mathematisch-Naturwissenschaftlichen Fakultät der Universität zu Köln im Jahr 2022 als Inaugural-Dissertation zur Erlangung des Doktorgrades im Promotionsfach Experimentalphysik angenommen.

Abstract

This thesis consists of two parts which deal with the low-energy electric dipole response (LEDR) of atomic nuclei and the development and commissioning of a digital data acquisition system for nuclear-structure experiments, respectively. A term commonly found in the literature for the overall LEDR of atomic nuclei is Pygmy Dipole Resonance (PDR), which was historically used to imply the picture of a neutron-skin oscillation. Since the underlying mechanisms in the LEDR region have been found to be diverse, the term PDR was avoided within this thesis, unless referring explicitly to a neutron-skin oscillation. Part I tries to uncover the generating nuclear-structure features at play in the LEDR of ^{120}Sn below the neutron-separation threshold via two complementary experiments and their theoretical comprehension. The conducted $^{120}\mathrm{Sn}(\alpha, \alpha'\gamma)$ and $^{119}\mathrm{Sn}(d, p\gamma)$ experiments are presented and nuclear-structure calculations performed within the Quasiparticle-Phonon-Model (QPM) are introduced, together with two corresponding reaction-theory approaches. The α-scattering experiment was performed at the Research Center for Nuclear Physics in Osaka, Japan, utilizing the combined particle and γ-ray spectrometer setup CAGRA+GR. Experimental results indicate the presence of isoscalar excitations with a surface-mode character in the LEDR of ^{120}Sn, resembling a neutron-skin oscillation. The $^{119}\mathrm{Sn}(d, p\gamma)$ transfer experiment was performed with the SONIC@HORUS setup at the University of Cologne and constitutes a novel tool to study the microscopic character of individual LEDR states. The remarkable agreement between theoretically obtained $(d, p\gamma)$ cross sections and the experimental data allows to benchmark the predictive power of the QPM and therein employed Energy-Density-Functional calculations. Furthermore, the QPM reproduces the key structural aspects of the LEDR in ^{120}Sn suggested by previous experiments, including the summed $\mathrm{B}(E1)\uparrow$ strength and a transition to more complex configurations at higher excitation energies. It was enforced that theory and experiment are consistently compared via identical observables and striking agreement is found for several experimentally accessible values on a quantitative level. The microscopic information, obtained for the first time in this thesis, complements the knowledge on the relevant nuclear-structure phenomena present in the LEDR of ^{120}Sn.

Part II covers a state-of-the-art digital data acquisition system which was designed and commissioned within this thesis. The flexible system exhibits significantly reduced dead time and reaches excellent energy resolution for γ-ray spectroscopy. It fully replaces the predecessor system and is suitable for all nuclear-physics experiments performed today and in the near future at the 10 MV FN-Tandem accelerator laboratory of the University of Cologne.

"There is not a discovery in science, however revolutionary, however sparkling with insight, that does not arise out of what went before.

. . .

And to learn that which goes before does not detract from the beauty of a scientific discovery but, rather, adds to it; just as the gradual unfolding of a flower, as seen by time-lapse photography, is more wonderful than the mature flower itself, caught in statsis."

from *Adding a Dimension* by Isaac Asimov

Contents

Part I

Investigation of Microscopic Structures in the Low-Energy Electric Dipole Response of ^{120}Sn using Consistent Experimental and Theoretical Observables

1 Introduction

Atomic nuclei are a challenging, yet fascinating laboratory for the behavior of nuclear matter on nearly the smallest scales known today. The nuclear force, which rules the interactions between protons and neutrons inside a nucleus, makes it possible that nuclear matter displays various pronounced features throughout the isotopic chart. Ranging from the lightest nuclei, which can be described by ab-initio methods today, to the heaviest nuclei reaching nucleon numbers that demand a more statistical description, nuclear matter obeys the rules of many-body quantum systems. It chooses to exhibit different features depending, at times acutely, on the number of nucleons available and their basic interaction. On a vastly different scale, astrophysical objects such as neutron stars are understood as nuclear matter too, underlining the importance of the nuclear interaction over several orders of magnitude. The transitional regime between few-body systems and the statistical regime poses one of the challenges that the field of nuclear physics has been facing over the last century and still is today. Building on the pioneering works performed by the likes of Sir James Chadwick [1], Hans Bethe [2], or Maria Goeppert-Mayer [3] in the early 20^{th} century, immense knowledge about the nuclear landscape has since been obtained.

The atomic nucleus consists of positively charged protons and uncharged neutrons. These nucleons embody the largest mass in an atom, albeit being concentrated in an object five orders of magnitude smaller than the overall atom. The nuclear interaction between nucleons has been found to be dominantly attractive and of short range type, overcoming the Coulomb repulsion of protons inside the nucleus. A highly repulsive behavior is exhibited at very small distances which, in combination with the Pauli

principle, causes the general incompressibility of nuclear matter. Especially the latter enables a quasi-free movement of nucleons in the mean-field potential of the nucleus that is being generated by all nucleons simultaneously, allowing the development of both single-nucleon and collective motion inside the system. The gross features of (stable) atomic nuclei, such as their masses, binding energies, overall stability, and even the rough magic numbers, are largely dictated by the mean field. It is the residual interaction, extending beyond the average behavior, that gives rise to distinct phenomena in the excitation spectra of nuclei and opening the field of nuclear-structure physics.

Common types of excitation in nuclei are rotations and vibrations, in which the motion is shared among many, sometimes all, nucleons. This collective behavior was historically described in macroscopic models, such as the rigid-rotor or harmonic-oscillator model. In the case of rotation, a deformation of the nucleus is essential, since a spherical quantum system cannot be rotated. Depending on the amount of deformation and the rigidity of the nuclear rotor body, characteristic rotational bands form in the excitation spectrum. Special attention is attracted when a given nucleus exhibits different levels of deformation, which form distinct rotational bands built on top of each underlying deformation and express a so-called *shape coexistence* in the nucleus. The interplay between rotational forces and the nuclear force can be investigated by considering excitation energies of rotational-band members and transition strengths of the corresponding γ decays de-exciting the initial rotation. Likewise, studies can be performed on vibrational bands, which follow rules similar to a harmonic oscillator.

A prime example of collective nuclear excitation are quadrupole vibrations. For spherical even-even nuclei above a certain mass, this typically manifests in a low-lying state with spin of $J = 2$ and positive parity, commonly the first excited $J^\pi = 2^+$ state. The picture quickly becomes more complex for nuclei with odd nucleon numbers. On the other side of the collective excitation spectrum are giant resonances, typically well above the particle threshold [4, 5]. Different types of resonances have been found in nuclei, distinguished by their multipole order and isospin character, i.e., whether protons and neutrons oscillate in-phase or out-of-phase. A common example for such pure resonances is the IsoVector Giant Dipole Resonance (IVGDR), which was first observed in 1937 by Bothe and Gentner [6] and interpreted as a giant resonance by Migdal in 1944 [7]. Other resonances were later discovered thanks to the advent of high-energy cyclotron beams in the 1970s. Well-studied examples are the IsoScalar Giant Monopole Resonance (ISGMR) [8] and the IsoScalar Giant Dipole Resonance (ISGDR) [9]. In all three cases, the entire proton and neutron bodies vibrate in-phase or out-of-phase in a motion corresponding to their multipole order. A dynamic dipole moment is generated by the out-of-phase oscillation of all protons against all neutrons (IVGDR), and

the compressional in-phase oscillation of all protons and neutrons inside the nucleus (ISGDR). The ISGMR is also called *breathing mode*, relating to the in-phase expansion of both nucleon bodies without generation of a multipole field. For the IVGDR case, the strength exhausted by it in medium to heavy-mass nuclei is typically more than 90 % of the Thomas-Reiche-Kuhn sum rule [10, 11]. The latter had been introduced in atomic physics to estimate the electric dipole interaction of atoms.

Below the neutron-separation threshold (S_n), and typically well below the IVGDR, a secondary accumulation of electric dipole ($E1$) strength is commonly found in nuclei above a certain mass. For the case of even-even nuclei, this manifests in an accumulation of discrete excited $J^\pi = 1^-$ states around and below S_n and forms the center of attention in this thesis. It was first reported on in 1961 by Bartholomew *et al.* and has historically been referred to as the *Pygmy* Dipole Resonance (PDR) [12]. The term pygmy here denotes the small summed strength, compared to the IVGDR, of only a few percent. Early interpretations described it as an oscillation of the excess-neutron skin against an $N = Z$ core within the *three-fluid-model* [13]. Alternative approaches for the cause of low-lying $E1$ strength in atomic nuclei include toroidal nucleon motion [14, 15] and the formation of α clusters at the nuclear surface [16, 17]. However, the precise generation mechanisms at play in the PDR region are diverse and not completely understood [18, 19]. Still today, the term PDR is often used in the literature to imply the picture of a neutron-skin oscillation. It was, thus, chosen to use the term Low-energy Electric Dipole Response (LEDR) throughout this thesis when referring to the general $E1$ strength below S_n and to avoid the term PDR, unless referring explicitly to a neutron-skin oscillation.

The nature of LEDR strength has attracted a lot of interest over the past two decades, not only due to its relevance for nuclear structure, but also thanks to its connection to astrophysical applications [18]. Independent of the underlying structure of the LEDR, its importance for neutron-capture reactions has been pointed out already in the 1960s [20]. The effect for rapid neutron-capture nucleosynthesis (*r* process) is even more pronounced. As the *r* process drives matter away from the valley of stability, neutron-separation energies decrease and the LEDR is then expected to be just above S_n and to have higher total strength due to the large neutron excess, impacting the resonant capture of neutrons. It has been shown that calculations using only IVGDR strength underestimate *r* process production rates and that additional LEDR strength has to be taken into account for reactions on exotic neutron-rich nuclei in astrophysical applications [21–25]. Furthermore, specific (n, γ) reaction rates become important during the late and cooler stages of the *hot r* process, once a statistical equilibrium between $(n, \gamma) \rightleftharpoons (\gamma, n)$ reactions is no longer valid [26]. For these scenarios, the experimentally unaccessible (n, γ) cross sections are statistically modelled based on the general photon-strength

distributions exploiting the β-*Oslo* method [27] or γ-*ray strength-function* method [28]. However, a pronounced dependence on nuclear-structure effects might have significant impact on (n, γ) reactions which is not reflected in the photon-strength function alone. In general, a more direct access to radiative neutron-capture cross sections is desired for nuclei with lifetimes or natural abundances unfeasible for direct (n, γ) studies [29]. Only recently, the (d, p) reaction has been established as a *surrogate* reaction for the determination of (n, γ) cross sections for astrophysical applications [30, 31].

Secondly, the formation of a neutron skin provides valuable guidance for parameters of the equation-of-state for nuclear matter around saturation density [32–35]. Especially the slope parameter of the nuclear symmetry-energy has been shown to be correlated to the dipole polarizability α_D of nuclear matter and the neutron-skin thickness $(r_n - r_p)$ [36]. While α_D can be determined from the $E1$ photoabsorption cross section [37], the neutron-skin thickness is only unambiguously measurable around ground-state density, e.g., in parity-violating electron scattering experiments [38, 39]. Such scattering experiments are sensitive to the weak interaction between electrons and neutrons and, therefore, suffer from considerably low cross sections and statistics. It is, thus, desirable to identify the neutron-skin content in the overall LEDR strength and find a quantitative description for it both experimentally and from theory.

The overall strength and distribution of states in the LEDR region below S_n is typically investigated in real-photon scattering (γ, γ') experiments, exploiting the cleanness of the probe compared to hadronic scattering experiments. Since real photons interact with the whole nucleus irrespective of the structure of excited states and purely via the electromagnetic interaction, they allow to chart the general $E1$ strength of a nucleus in a model-independent way. The necessary photon beam is commonly generated via a high-energy electron beam impinging on a dedicated radiator target, which produces a continuous bremsstrahlung spectrum with the endpoint energy equal to the electron beam energy, i.e., in the order of several MeV. By collimating the bremsstrahlung radiation onto the target material of interest, nuclear states are excited in it and their decay is observed with γ-ray detectors. Hence, the method is known as Nuclear Resonance Fluorescence (NRF), in analogy to the similar process within the atomic shell. The continuous nature of the initial photon beam induces unwanted background in the recorded γ-ray spectra due to atomic scattering and weak transitions can be difficult to observe. However, NRF experiments have the advantage of delivering the majority of $E1$ strength within one experiment. Dedicated ^{11}B flux-calibration targets allow to determine absolute values by calibrating the beam shape and accumulated beam flux. Feeding and decay branching can be partially identified by measuring at different electron-beam endpoint energies and comparing extracted yields. How-

ever, bremsstrahlung NRF experiments deliver the most reliable information for strong $E1$ excitations with a dominant decay back to the ground-state. Detailed information on other γ-decay branches and also genuinely weaker excitations are investigated in (γ, γ') experiments using quasi-monoenergetic photons beams produced by Laser-Compton-Backscattering. In these modern experiments, an optical laser collides with ultra-relativistic electrons of several GeV and is boosted to several MeV via Compton scattering around 180°. Depending on the chosen electron energy and scattering angle, γ-ray beams with a fine-tunable centroid energy and narrow bandwidth are obtained and used to sample the target material in incremental regions of excitation energy. However, such experiments need calibration information from a preceding bremsstrahlung measurement and are more complex and time consuming. Both types of experiments are, among others, used in the field of nuclear photonics. Further details can be found in a recent review article on the topic [40]. Especially the bremsstrahlung NRF method has been used for decades in studies on nuclear dipole excitations and is responsible for the abundant information on the LEDR strength available today throughout the valley of stability.

The first experimental evidence for a manifold structure in the LEDR was found about 15 years ago [41] when comparing data from high-resolution $(\alpha, \alpha'\gamma)$ coincidence experiments to existing (γ, γ') NRF data. The α-scattering experiments were performed with a comparably high beam energy of $\mathrm{E}_\alpha = 136\,\mathrm{MeV}$ and scattering under forward angles around 3.5° with the Big-Bite spectrometer of the Kernfysisch Versneller Instituut (KVI) at the University of Groningen in the Netherlands. The ground-state γ decay of excited and identified $J^\pi = 1^-$ states was observed via large volume High-Purity-Germanium (HPGe) detectors. An energy splitting in the response to (α, α') was found in several nuclei between ^{94}Mo and ^{140}Ce, which separated the LEDR states into two groups. The lower-energy group could be excited in both (α, α') and (γ, γ'), while the higher-energy group was only observed in NRF. This behavior was soon related to an isoscalar and neutron-skin character of the lower group and a more complex structure, related to the IVGDR, of the higher-lying group [42, 43]. This so-called *isospin* splitting was most clearly observed in ^{124}Sn and is shown in Fig. 1 for reference.

The α particles, being both an isoscalar probe and sensitive to surface excitations under the employed kinematics [4], helped to identify the PDR-like content within the overall LEDR. From this point on, the searing question for the number and types of underlying structures in the LEDR arose. Shortly after, experiments using ^{17}O scattering as an isoscalar surface probe found the same behavior [44, 45], as well as $(p, p'\gamma)$ at intermediate energies of $\mathrm{E}_p = 80\,\mathrm{MeV}$ [46]. All experiments probed the surface character of the excitations which reflected the macroscopic and somewhat collective picture of a

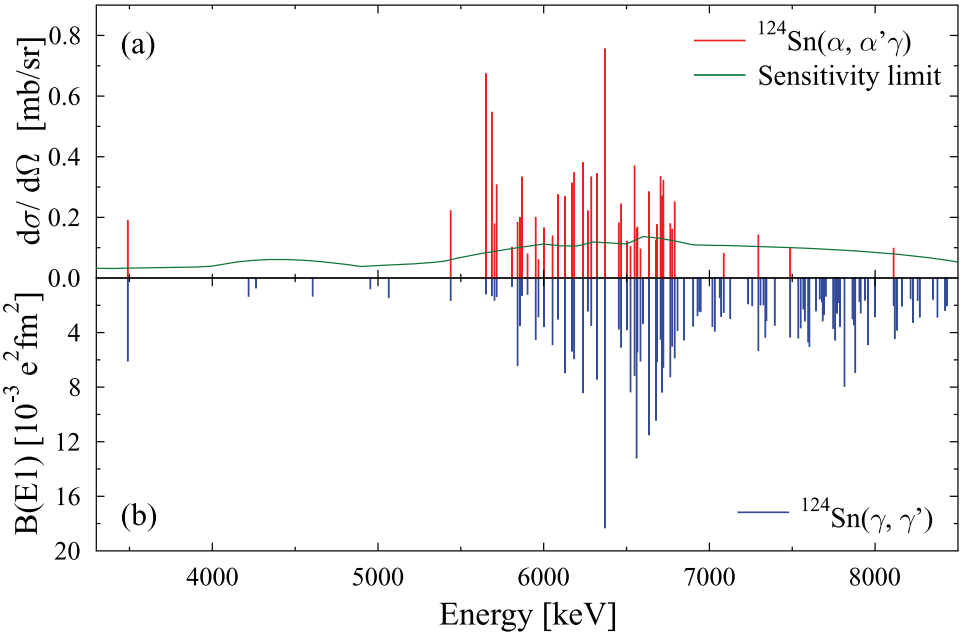

Figure 1: (*a*) Singles cross sections for the excitation of $J^\pi = 1^-$ in ^{124}Sn deduced from the $(\alpha, \alpha'\gamma)$ experiment at $\mathrm{E}_\alpha = 136$ MeV. The solid line represents the sensitivity limit. (*b*) The $\mathrm{B}(E1)\uparrow$ strength distribution obtained in NRF. Reprinted figure with permission from J. Endres *et al.*, Phys. Rev. C **85**, 064331 (2012) [42]. Copyright (2012) by the American Physical Society.

neutron-skin oscillation. However, the possible contribution from strong single-particle configurations within the LEDR suggested by theory [47, 48] was not observed experimentally so far. The current picture of the LEDR is that there are at least two kinds of nuclear-structure mechanisms apparent below S_n and the degree of collectivity of both kinds is still a matter of debate. A recent overview of studies on nuclear dipole strength with focus on the isospin character of the LEDR is given in Ref. [19].

It is the scope of this thesis to investigate the surface-mode character of the LEDR in ^{120}Sn using $(\alpha, \alpha'\gamma)$ data and to search for new structural information on the microscopic character of the LEDR through a ^{119}Sn$(d, p\gamma)$ experiment. The $(d, p\gamma)$ reaction was employed already in the 1960s and found an increased γ-ray strength below S_n in several nuclei [49]. However, it was performed with modern instruments within this thesis and could be established as a new tool to study the fine structure and single-particle content of the LEDR. Both experiments, and the consecutive comparison to theory, profited from the rich NRF data available from a recent high-sensitivity study on ^{120}Sn(γ, γ') using bremsstrahlung [50]. Nuclear-structure calculations based on the Quasiparticle-Phonon-Model (QPM) were investigated and a novel reaction theory approach was employed to predict experimental $(d, p\gamma)$ yields. Theoretical calculations on the LEDR are typically compared to experiments based on their predicted $\mathrm{B}(E1)\uparrow$ strength, while this

value is often not directly accessible in experiments such as (γ, γ'). Similarly, early calculations performed on the ^{124}Sn$(\alpha, \alpha'\gamma)$ reaction only gave access to the isoscalar $E1$ strength in terms of $B_{IS}(E1)$, instead of realistic cross sections. Therefore, a consistent comparison to theory was performed within this thesis by enforcing that theoretical formalisms yield the same observable as accessed in the experiments. Consequently, the need for further abstraction could be eliminated in the case of ^{120}Sn.

Chapters 2 and 3 of Part I present the experimental setups employed for the ^{120}Sn$(\alpha, \alpha'\gamma)$ and ^{119}Sn$(d, p\gamma)$ measurements, respectively, and explain the necessary analysis steps. The ^{120}Sn$(\alpha, \alpha'\gamma)$ experiment was performed with the combined CAGRA+GR spectrometers at the Research Center for Nuclear Physics (RCNP) in Osaka, Japan, and the complementary ^{119}Sn$(d, p\gamma)$ experiment was performed with the SONIC@HORUS setup at the University of Cologne (UoC). An overview of performed QPM calculations and the two theoretical approaches for cross-section predictions is given in Chapter 4. Results and details of all experimental and theoretical data are discussed in Chapter 5, together with future perspectives for the novel $(d, p\gamma)$ approach and the general search for structural information on the LEDR.

Part II of this thesis presents the digital data acquisition system *NuDAQ*, which was envisioned, tested, and commissioned throughout this work. Chapter 6 introduces the general system and discusses the conducted performance tests. While it was not used to take data during the experiments presented in Part I, the design work and tests performed within this thesis establish it as a high-resolution and low-dead-time data acquisition solution for the experiments commonly performed at the 10 MV FN-Tandem laboratory at UoC.

2 ^{120}Sn$(\alpha, \alpha'\gamma)$ Experiment at the CAGRA+GR Setup

In fall of 2016, a large experimental campaign was conducted at the Research Center for Nuclear Physics (RCNP) in Osaka, Japan. Over 1100 h of beam time were accumulated during the campaign, measuring several $(\alpha, \alpha'\gamma)$, $(p, p'\gamma)$, and $(^6\text{Li}, ^6\text{Li}^*\gamma)$ reactions under forward angles. The local Grand Raiden magnetic spectrometer (GR) was coupled to the Clover Array Gamma-ray spectrometer at RCNP for Advanced research (CAGRA), consisting of twelve HPGe Clover-type detectors and four large-volume LaBr detectors. Eight HPGe Clover detectors were mounted in a ring around the target position at an angle of 90° relative to the beam axis, and four were mounted under backward angles of 135°. The four LaBr detectors were mounted under forward angles of 45° relative to the beam. During the ^{120}Sn$(\alpha, \alpha'\gamma)$ experiment, the AVF cyclotron provided a pulsed $^4\text{He}^{2+}$ beam at an energy of $\text{E}_\alpha = 130$ MeV and at a frequency of 12.4 MHz, resulting in a time between bunches of 80.65 ns. The GR was rotated to a central scattering angle of $\Theta_\alpha = 4.5°$ in order to increase sensitivity to $E1$ excitations and an average beam current of 2.5 pnA impinged on a self-supporting ^{120}Sn target of 2.7 mg/cm^2 thickness for a total measurement time of approx. 65 h. The target ladder was rotated by 22.5° around the vertical axis in order to remove unnecessary absorbing material between target nuclei and the HPGe detectors. While both the GR and CAGRA spectrometer had individual data acquisition systems (DAQs), their clocks were synchronized and the CAGRA DAQ could be set to coincidence mode with a trigger on detected particles in the GR spectrometer in order to reduce data readout.

The following chapter describes the experimental setup, explains the available information from both the particle and γ-ray spectrometer, and shows the analysis steps necessary to perform a precise coincidence analysis of the recorded data. Finally, absolute cross sections will be presented. A detailed discussion and comparison to other experiments will be given in Chapter 5. A theoretical prediction of (α, α') excitation cross sections based on the same QPM input used for ^{119}Sn(d, p) will be presented in Chapter 4.3.

2.1 The Grand Raiden Magnetic Spectrometer

Located at the West Experimental Hall of the AVF and RING cyclotron facility at RCNP, the GR has been established as a high precision tool for studies of inelastic scattering and charge exchange reactions at small angles including 0°. Employing the dispersion matching mode of the spectrometer, an excitation energy resolution of few keV can be reached independent of the excitation energy, exceeding even the energy resolution commonly obtained with HPGe detectors at higher energies [51]. During scattering

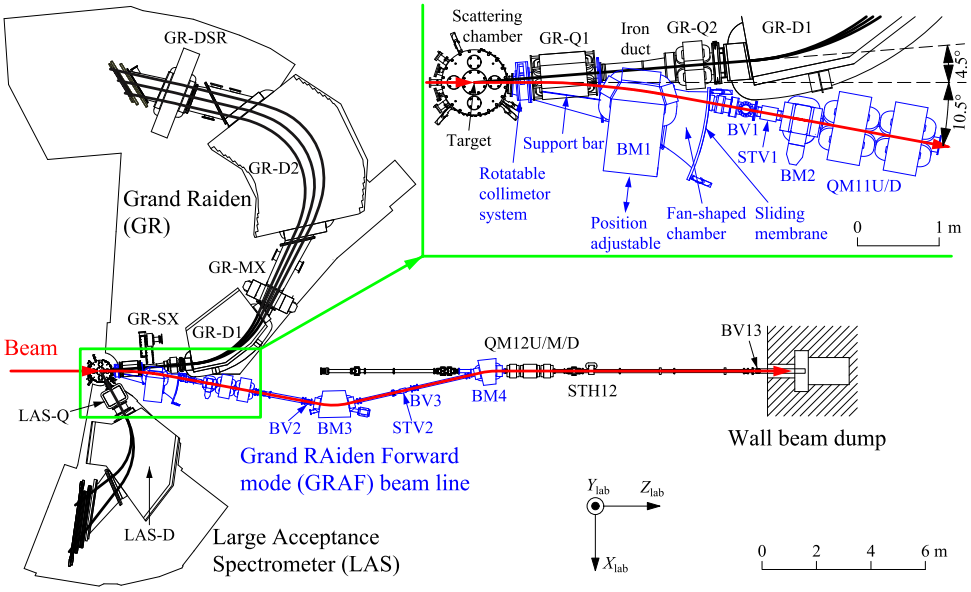

Figure 2: Sketch of the Grand RAiden Forward mode (GRAF) beamline. The un-scattered beam is transported about 25 m downstream from the target position and is stopped in a shielded Faraday cup. Reprinted figure with permission from Ref. [52]. Copyright (2019) by Springer Nature.

experiments including 0°, ions which were not scattered from the target are transported to a Faraday cup within the spectrometer where they are prevented from reaching the focal plane detector system and the accumulated charge can be read out. However, the transportation mode used during the CAGRA+GR campaign was changed in order to increase the acceptance of the spectrometer while maintaining a sufficient excitation energy resolution in the order of 100 keV and to transport the un-scattered beam to a shielded beam dump about 25 m downstream from the target position. The latter is especially important when using γ-ray detectors close to target position, as these would otherwise suffer from the γ and neutron radiation produced in the beam dump. The extended Grand RAiden Forward mode (GRAF) beamline was, thus, implemented for the CAGRA+GR campaign, see Ref. [52] for further details. Figures 2 and 3 show the the complete GRAF beamline and the configuration used during the experiment with the CAGRA array coupled to the GR spectrometer at target position. To make space for both the CAGRA array and the GRAF beamline, the first sextupole magnet of the GR spectrometer (GR-SX in Fig. 2) could not be used, which affected the scattered particle transport through the spectrometer and the determination of the precise scattering angle within the GR acceptance (see Chapter 2.2.3).

The GR spectrometer consisted of three dipole magnets, two quadrupole magnets and a multipole magnet in a QQDMDD configuration, with the focal plane detection system located behind the last dipole magnet. In addition, the Large Acceptance Spectrometer

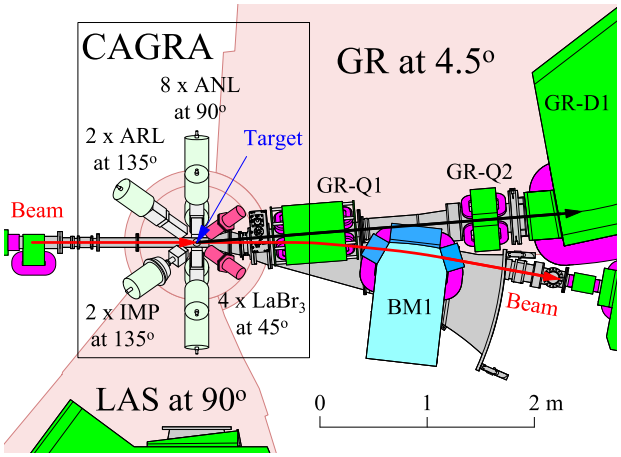

Figure 3: Sketch of the CAGRA γ-ray spectrometer coupled to the GR magnetic spectrometer and the GRAF beamline at target position. Reprinted figure with permission from Ref. [52]. Copyright (2019) by Springer Nature.

(LAS) was coupled to the target chamber at a larger scattering angle and was used for online monitoring of the beam position. The focal plane detection system was rotated at 45° relative to the ideal ion track and consisted, in the order in which particles passed the detectors, of two multi-wire drift chambers (MWDC1, MWDC2) and two plastic scintillation counters (PS1 and PS2). A coincidence between PS1 and PS2 was used to generate an online trigger for the GR data acquisition and also the CAGRA data acquisition when set to coincidence mode. The local MyRIAD system was used to distribute synchronized timestamps among both data acquisitions. An overview of the overall signal path and triggering logic of both GR and CAGRA spectrometers is shown in Appendix A.1 and a more detailed explanation of the explicit signal read out and routing can be found in Ref. [53].

Figure 4 shows in a simplified way how scattering at target position affects the ion track through the spectrometer. After correction for kinematic and ion-optical effects, the α particle energy E_α will later be determined from the position X on the focal plane. The precise determination of the penetration point of each particle on the focal plane (X, Y) and its angle relative to the ideal ion track in the dispersive (Θ_d) and the non-dispersive (Φ_d) direction, as well as particle identification based on the energy loss in PS1 and PS2 ($\Delta\mathrm{E}_1$ and $\Delta\mathrm{E}_2$) is possible with the combined information from MWDC1, MWDC2, PS1, and PS2. The time difference RF between the triggering PS detector and the AVF cyclotron pulse can be used to determine the time-of-flight of detected particles through the spectrometer. A designated angle calibration measurement called *sieve-slit* measurement allows to determine each α particle's scattering angle at target position in the rotation direction of the spectrometer (Θ_{tgt}) and perpendicular to it (Φ_{tgt}).

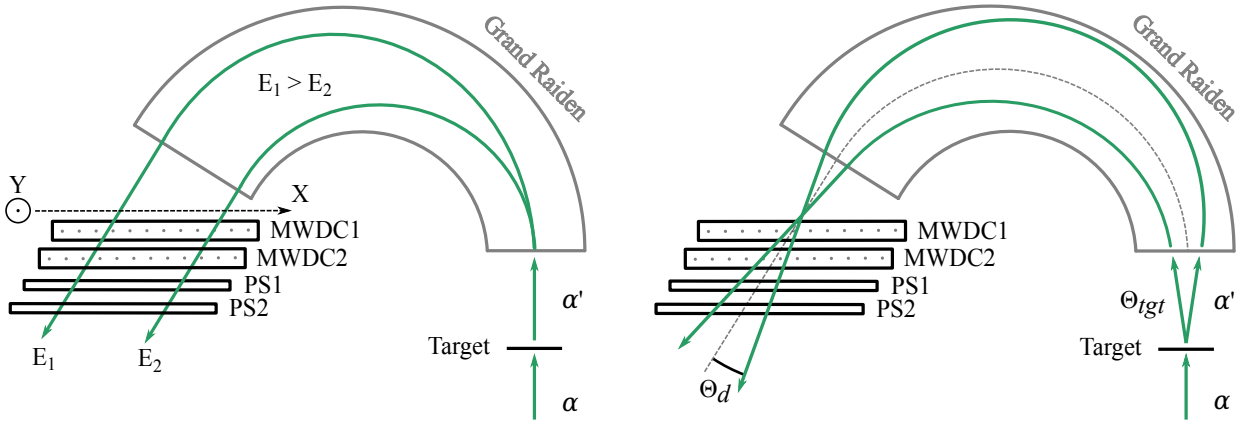

Figure 4: Schematic α particle tracks within GR. Both MWDC systems give intersection of particle track with MWDC plane in X (along the focal plane) and Y (perpendicular to the dispersive plane). *Left*: Determination of different scattered α particle energies E_1 and E_2 based on X position on focal plane. *Right*: Correlation of target scattering angle Θ_{tgt} and detection angle Θ_d. Interpolation between intersection points in MWDC detectors gives Θ_d relative to the central particle track. PS1 and PS2 are used for particle identification via $\Delta\mathrm{E} - \mathrm{E}$ method.

2.2 Kinematic and Ion-Optical Corrections

2.2.1 MWDC Drift Time Calibration

Each MWDC contains a vertical wire plane (X) and a tilted wire plane (U) at an angle of 48.19° relative to the vertical X plane, with an active area of 1150 mm by 120 mm and a thickness of 20 mm. The spacing between sense wires is 6 mm on the X plane and 2 mm on the U plane, while the largest possible drift distance perpendicular to the X and U

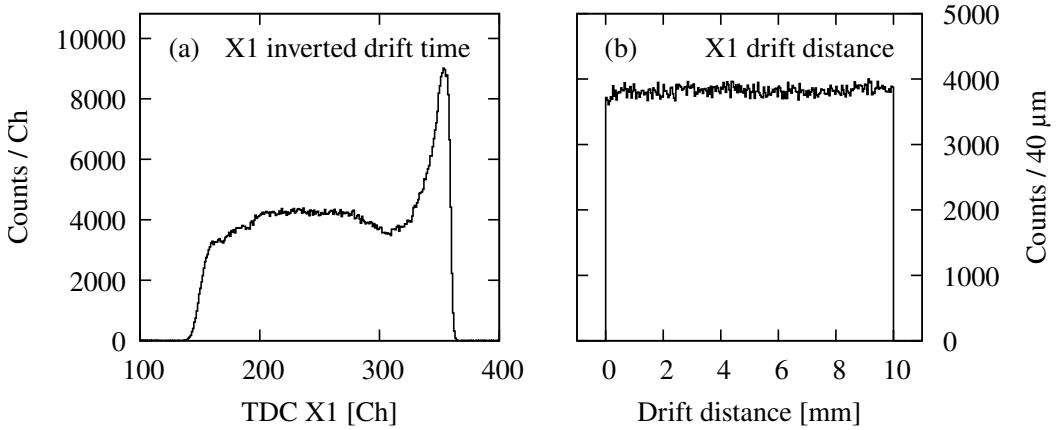

Figure 5: (*a*) Calibration of drift time to distance on the X1 plane based on the distribution of measured drift times. (*b*) After the correction, the distribution of drift distances is flat and a precise determination of X1 is possible. Identical calibrations were performed for the Y1, X2, and Y2 planes.

planes is 10 mm in both directions (see Ref. [51] for a detailed explanation of the MWDC setup). A more precise position information on each plane can be determined based on the time difference between signals on two or more adjacent sense wires and the triggering PS detector, which were measured using a Time-to-Digital Converter (TDC).

Due to the increased electric field strength close to the sense wires, the distribution of measured drift times peaks at high TDC values, representing short drift times. Figure 5 (*a*) shows the TDC drift time distribution for the X1 plane. Assuming a flat distribution of physical drift times over all sense wires, a look-up table can be generated via the GRUTINIZER analysis software provided by the CAGRA collaboration. The drift time TDC values are then transformed to physical drift distances between the α particle's track and the sense wires based on the generated look-up table, which is shown for the X1 plane in Fig. 5 (*b*). From the drift distances relative to two or more adjacent sense wires, the precise crossing point of the ion track and each wire plane is determined within GRUTINIZER. Using the interaction points on all four wire planes, a precise position on the focal plane and the penetration angle can later be determined, even if the exact focal plane is not parallel to the orientation of the MWDCs. This flexibility is crucial for a high-resolution measurement as the excitation energy is eventually determined from the ion's position on the focal plane.

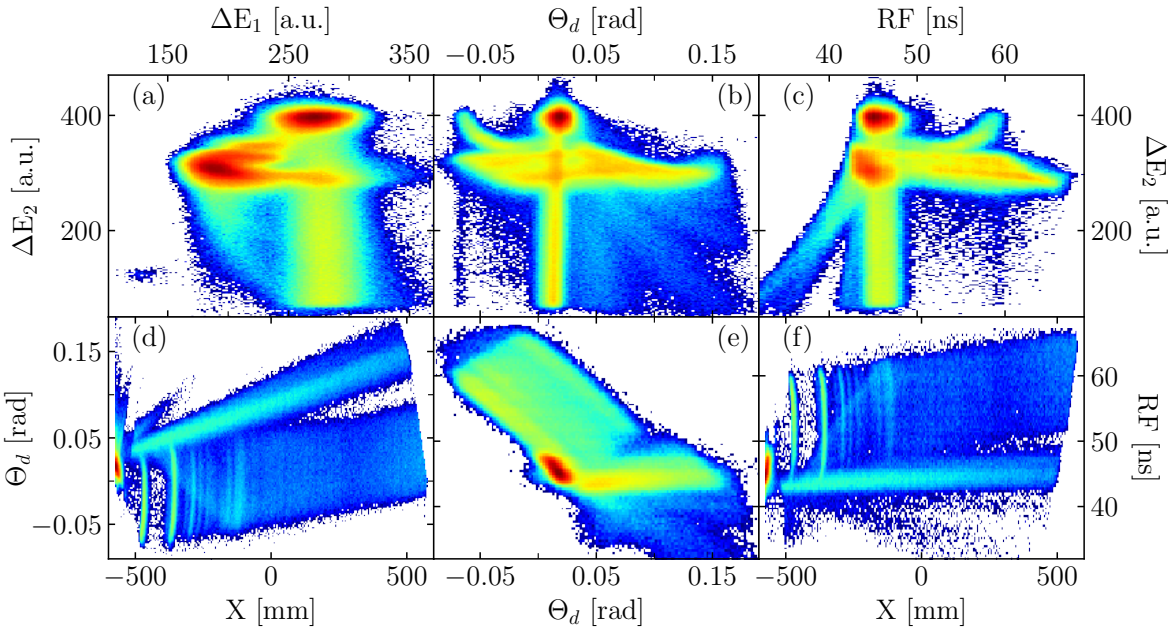

Figure 6: Correlated ^{120}Sn(α, α') spectrometer data. (*a*) Energy ΔE_1 and ΔE_2 deposited in PS1 and PS2. (*b*) α detection angle Θ_d and energy ΔE_2 deposited in PS2. (*c*) RF time and energy ΔE_2 deposited in PS2. (*d*) X position on focal plane and α detection angle Θ_d. (*e*) α detection angle Θ_d and RF time. (*f*) X position on focal plane and RF time.

2.2.2 Time-of-Flight Correction

To identify valid spectrometer hits induced by α particles that stem from target position and have not been scattered, e.g., on the inside walls of the spectrometer, a number of correlated information were investigated based on recorded ^{120}Sn(α, α') data. Since the spectrometer data are rather complex, Figs. 6 to 9 try to visualize the embedded correlations and break down the iterative data preparation procedure.

Figure 6 shows the six different correlations relevant for particle identification and the following time-of-flight correction. The vertical and slightly bent shapes visible in Panels (*d*) and (*f*) of Fig. 6 already reveal discrete excitations in ^{120}Sn at negative X values. All panels of Fig. 6 show a contamination from part of the elastically scattered beam that could not be prevented from entering the spectrometer, located at approx. $\Delta E_2 = 400$ a.u. in Fig. 6 (*a*) - (*c*), below X $= -500$ mm in Fig. 6 (*d*) and (*f*), and at approx. $\Theta_d = 0$ in Fig. 6 (*e*). This contamination amounts to about 45 % of the statistics. The weak distribution of events in Fig. 6 (*a*) below $\Delta E_1 = 150$ a.u. represents deuterons that are produced in a ^{120}Sn$(\alpha, \mathrm{d})^{122}$Sb reaction at target position.

Fig. 7 shows the same data after a X > -500 mm condition was applied in order to remove the unwanted contamination. The strong concentration of hits at $\Delta E_2 = 400$ a.u. and the vertical bands in Fig. 7 (*a*) - (*c*) have vanished and Fig. 7 (*e*) now only shows valid events contaminated by a horizontal band. The latter is caused by a significant

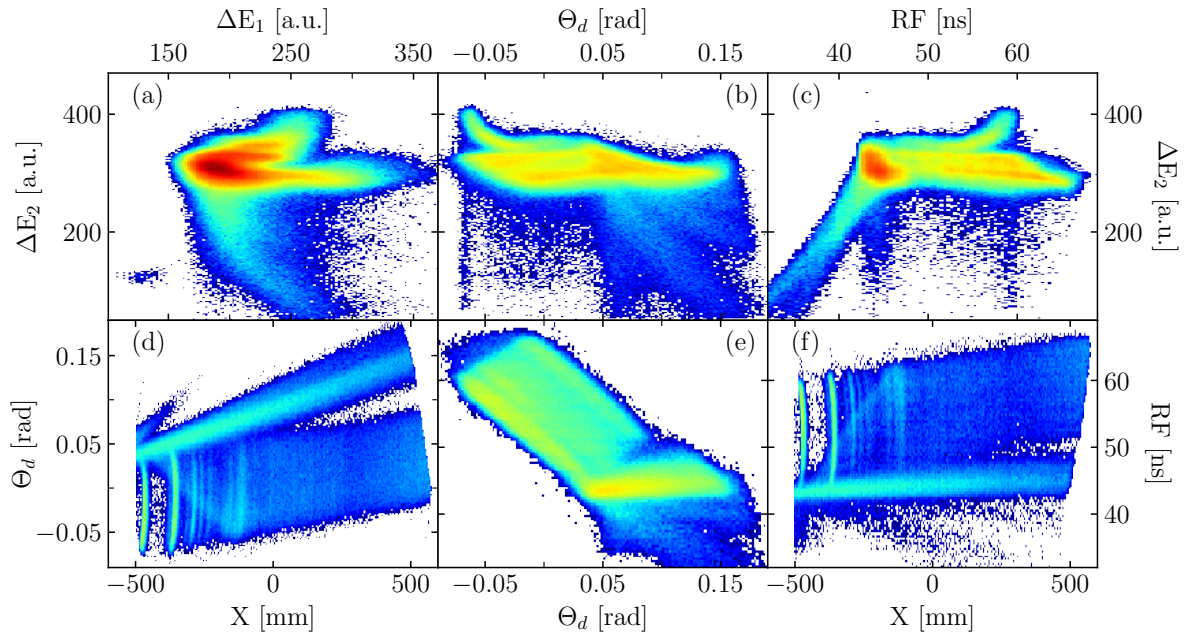

Figure 7: Correlated ^{120}Sn(α, α') spectrometer data after applying a cut on X > -500 mm. Labeling in Panels (*a*) to (*f*) identical to Fig. 6

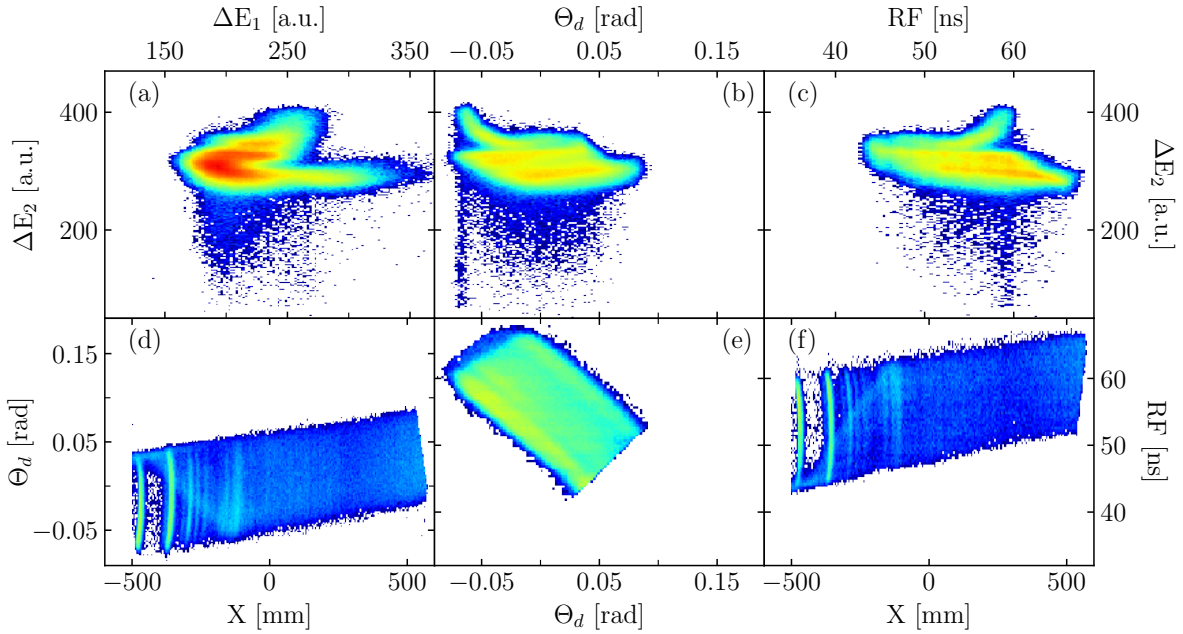

Figure 8: Correlated ^{120}Sn(α, α') spectrometer data after applying a cut on X $>$ −500 mm and a graphical cut on clean events in Θ_d−RF matrix (compare Fig. 6 (*e*) and Fig. 7 (*e*)). Labeling in Panels (*a*) to (*f*) identical to Fig. 6

part of the elastically scattered beam that reached the focal plane detectors by scattering on the inside walls of the spectrometer. These events also cause continuous diagonal distribution in Fig. 7 (*d*). To eliminate these misleading events, a polygon cut was applied on the tilted shape in Fig. 7 (*e*), after which Fig. 8 is obtained.

After applying the two conditions mentioned above, the majority of contaminations have been ruled out and only 31 % of the initial statistics remains as physically relevant data. A second polygon gate on $\Delta E_1 - \Delta E_2$ can then be determined from Fig. 8 (*a*) for a clean particle identification in the final $\alpha-\gamma$ coincidence analysis. However, the polygon cut on Θ_d−RF (Fig. 8 (*e*)) is unfavorable for the coincidence analysis, since the precise placement of the cut may affect the treatment of events depending on the excitation energy and the proximity to the polygon edges. Therefore, in addition to the particle identification using $\Delta E_1 - \Delta E_2$, an independent time-of-flight value $\mathrm{ToF}(\mathrm{RF}, \Theta_d, \mathrm{X})$ was determined for an additional condition to be placed on the coincidence data. Figure 9 (*a*) and (*b*) show the dependence of RF on Θ_d and X and are identical to Fig. 8 (*e*) and (*f*). In a first correction step, a linear dependence of RF on Θ_d was fitted to the diagonal bands seen in Fig. 9 (*a*), resulting in the corrected intermediate time-of-flight:

$$\mathrm{ToF}'(\mathrm{RF}, \Theta_d)[ns] = \mathrm{RF}[ns] - 148.3588 \cdot \Theta_d[rad] \tag{2.1}$$

After the first correction, the tilted bands are horizontal in Fig. 9 (*c*) and the broad diagonal has transformed to a narrow band in Fig. 9 (*d*). Again, a linear dependence of $\mathrm{ToF}'(\mathrm{RF}, \Theta_d)$ on X can be fitted for the final time-of-flight correction:

$$\mathrm{ToF} \equiv \mathrm{ToF}(\mathrm{RF}, \Theta_d, \mathrm{X})[ns] = \mathrm{ToF}'(\mathrm{RF}, \Theta_d)[ns] + 0.01514791 \cdot \mathrm{X}[mm] \tag{2.2}$$

Fig. 9 (*e*) and (*f*) show the time-of-flight information now independent of Θ_d and X. Using the corrected ToF, a cut on 53.7 ns $\leq$ ToF $\leq$ 59.4 ns is later applied in the coincidence analysis.

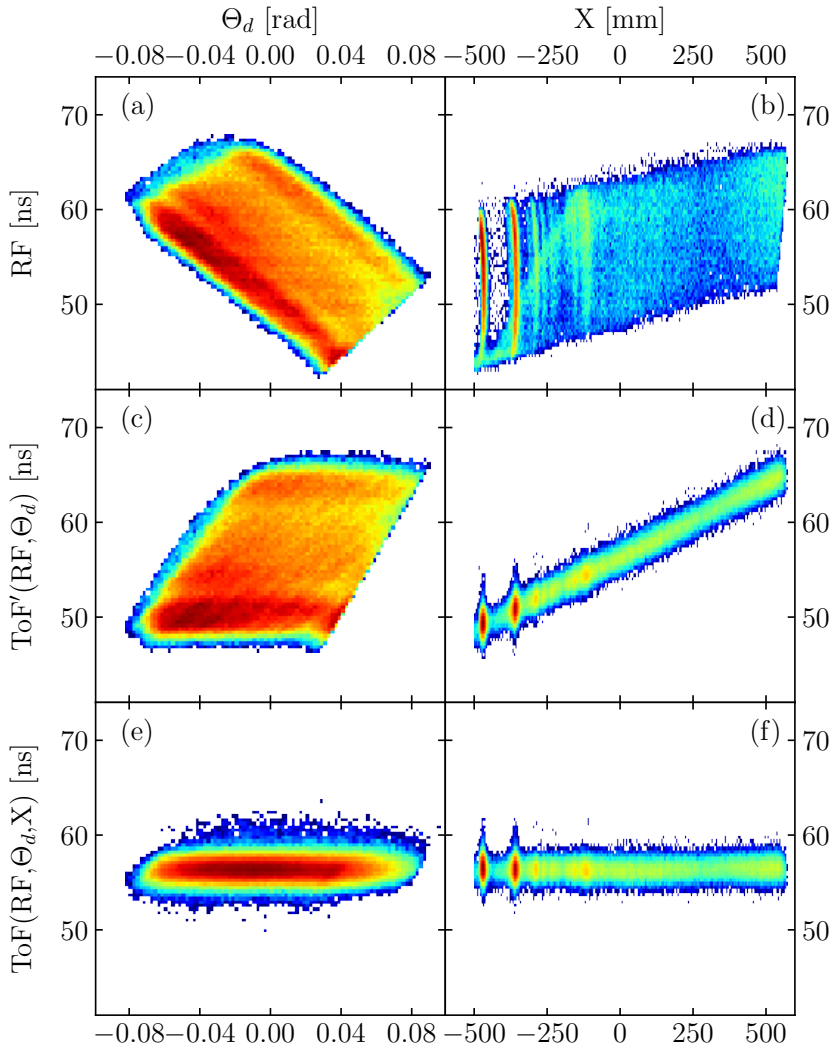

Figure 9: Time-of-flight (ToF) determination based on RF time and X position on the focal plane. Panels (*a*) and (*b*) show the initial data after applying conditions shown in Fig. 8. Panels (*c*) and (*d*) show the corrected time-of-flight $\mathrm{ToF}'(\mathrm{RF}, \Theta_d)$ correlated to Θ_d and X, respectively. Panels (*e*) and (*f*) show the final corrected time-of-flight $\mathrm{ToF}(\mathrm{RF}, \Theta_d, \mathrm{X})$, now independent of Θ_d and X.

2.2.3 Sieve-Slit Calibration

The α-scattering angle at target position relative to the beam axis (Θ_{tgt}) can be determined from the detection angle Θ_d and the Y position on the focal plane, as described in more detail in Ref. [51]. A 5 mm thick brass plate, the so-called *sieve-slit*, was mounted at the entrance of the spectrometer and the calibration measurement was conducted with a ^{64}Ni target and beam settings identical to the ^{120}Sn coincidence measurements. Figure 10 shows the sieve-slit with its five-by-five grid of boreholes at known distances, representing relative scattering angles of $\Delta\Theta_{tgt} = 0°, \pm 0.45°, \pm 0.9°$ and $\Delta\Phi_{tgt} = 0°, \pm 1.08°, \pm 2.16°$. The central borehole represents α scattering at a horizontal angle of $\Theta_{tgt} = 4.5°$, equal to the central angle of the spectrometer, and a vertical scattering angle $\Phi_{tgt} = 0°$, i.e., within the horizontal plane.

In order to calibrate the target scattering angles Θ_{tgt} and Φ_{tgt}, the dependence of Θ_d on X has to be corrected first. Figure 11 (*a*) shows the uncorrected data with five prominent diagonal bands representing the five Θ_{tgt} angles dictated by the sieve-slit. Figure 11 (*b*) shows the corrected data which have been calibrated to the horizontal target scattering angle via

$$\Theta_{tgt}[°] = 22.6266 \cdot \Theta_d[\mathrm{rad}] - 0.001242 \cdot \mathrm{X}[\mathrm{mm}] + 4.348. \tag{2.3}$$

Fig. 11 (*c*) shows the correlation between Y and the uncorrected detection angle Θ_d. Since the data are not yet aligned in terms of Θ_{tgt}, there are no sharp peaks forming. After calibration to the known scattering angles of the sieve slit, Fig. 11 (*d*) shows distinct accumulations which correspond to the five Θ_{tgt} and Φ_{tgt} angles expected in the sieve-slit measurement. The GR-SX sextupole magnet, which is part of the GR standard configuration, had to be removed from the spectrometer in order to fit the CAGRA array and GRAF forward beamline. Consequently, the data are strongly compressed in Y, making a precise calibration difficult. However, for four of the five Θ_{tgt} groups all of the five expected Φ_{tgt} peaks could be identified and the single accumulation showing for $\Theta_{tgt} = 3.6°$ was used for $\Phi_{tgt} = 0°$. Using a polynomial correction following the approach presented in Ref. [51], the Y position can be calibrated to the vertical scattering angle Φ_{tgt} via Eq. 2.4 with the parameters p_{ij} listed in Appendix A.2.

$$\Phi_{tgt} = \sum_{i=0}^{2} \sum_{j=0}^{2} p_{ij} \cdot \Theta_{tgt}^{i} \cdot \mathrm{Y}^{j} \tag{2.4}$$

Fig. 11 (*e*) and (*f*) show the calibrated target scattering angles for the ^{64}Ni sieve-slit measurement and the ^{120}Sn production data, respectively. Due to the missing GR-SX magnet and the induced compression of the data towards smaller Θ_{tgt} values, a pre-

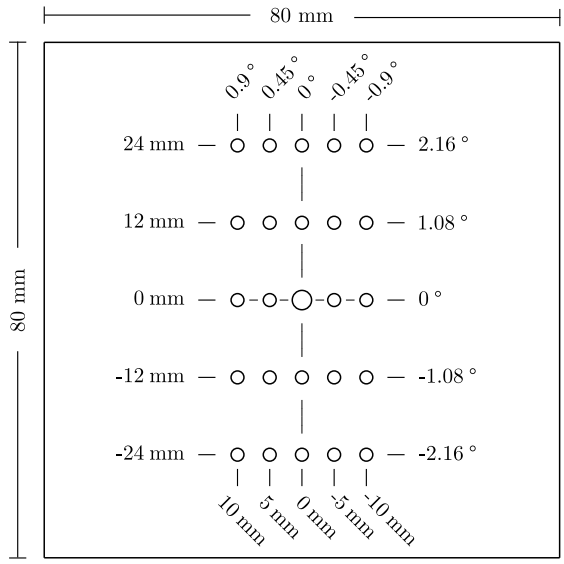

Figure 10: Sketch of the Sieve-Slit plate with a grid of five-by-five boreholes used for the calibration of scattering angles. The plate was mounted at the spectrometer entrance at a distance of 638 mm from target position. The distance between the boreholes is given as well as the resulting angle $\Delta\Theta_{tgt}$ (horizontal) and $\Delta\Phi_{tgt}$ (vertical) relative to the central spectrometer angle and the corresponding ideal scattering plane.

cise expansion of the Y values in this region is difficult. However, an estimation of the spectrometer acceptance is possible for the comparison to theoretical cross sections presented in Chapter 4.3. For the $\alpha-\gamma$ coincidence analysis, an artificial cut on the target scattering angles was chosen with $3.5° \leq \Theta_{tgt} \leq 5.5°$ and $\Phi_{tgt} \leq \pm 2°$, as shown in Fig. 11 (*f*). Due to the orthogonal nature of the $(\Theta_{tgt}, \Phi_{tgt})$ coordinate system and the small angles, the spectrometer solid angle can be determined via

$$\Delta\Omega_\alpha = \Delta\Theta_\alpha \times \Delta\Phi_\alpha = 2.51\,\text{msr}.$$

In a later analysis step, the α-scattering angle Θ_α and its rotation around the beam axis Φ_α will be determined from the calibrated target scattering angles. On the $\Phi_{tgt} = 0°$ plane, the α-scattering angle Θ_α is identical to the horizontal angle Θ_{tgt}. For other Φ_{tgt} angles, the rotation of Θ_α around the beam axis has to be taken into account. Figure 12 shows the geometrical definition of the two coordinate systems and Eqs. 2.5a and 2.5b describe the transformation.

$$\Theta_\alpha = \arccos\left(\cos\left(\Theta_{tgt} + \Theta_{\text{GR}}\right) \cdot \cos\Phi_{tgt}\right) \tag{2.5a}$$

$$\Phi_\alpha = \arctan\left(\frac{\tan\Phi_{tgt}}{\sin\left(\Theta_{tgt} + \Theta_{\text{GR}}\right)}\right) \tag{2.5b}$$

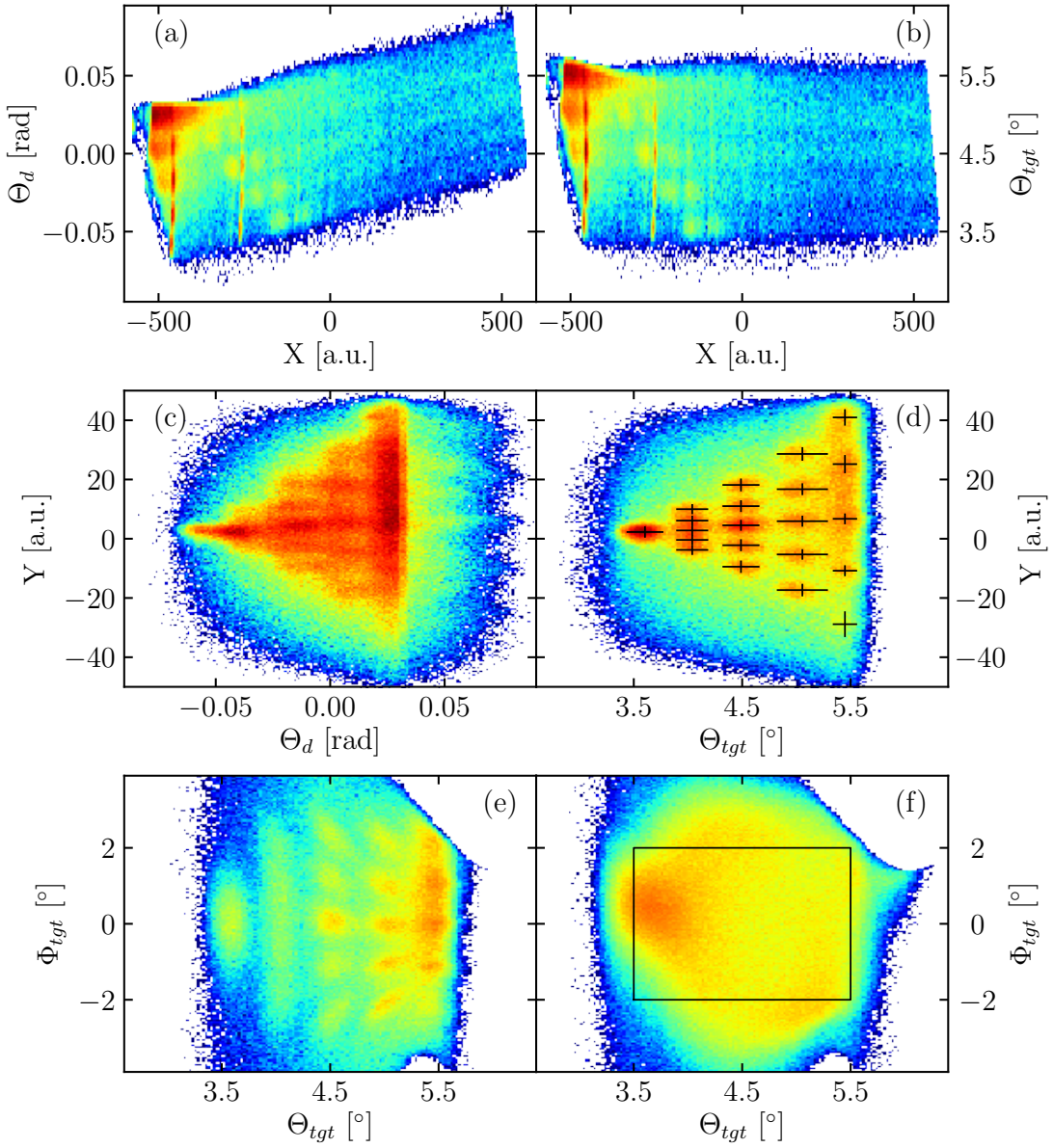

Figure 11: Sieve-Slit data taken with a ^{64}Ni target and the sieve plate shown in Fig. 10 placed between target and spectrometer. Panels (*a*) and (*b*) show the effect of the $X(\Theta_d)$ correction necessary to align the data and obtain the target scattering angle Θ_{tgt}. Panel (*c*) shows the correlation between Θ_d and Y before the correction. Panel (*d*) shows the aligned data calibrated to Θ_{tgt} and in correlation to Y with the points used for the polynomial sieve-slit correction marked in black. Panels (*e*) and (*f*) show the calibrated scattering angles at target position Θ_{tgt} and Φ_{tgt} for the ^{64}Ni sieve data and production ^{120}Sn data, respectively. The black box in (*f*) indicates the software acceptance of $3.5° \leq \Theta_{tgt} \leq 5.5°$ and $\Phi_{tgt} \leq \pm 2°$ used in coincidence analysis.

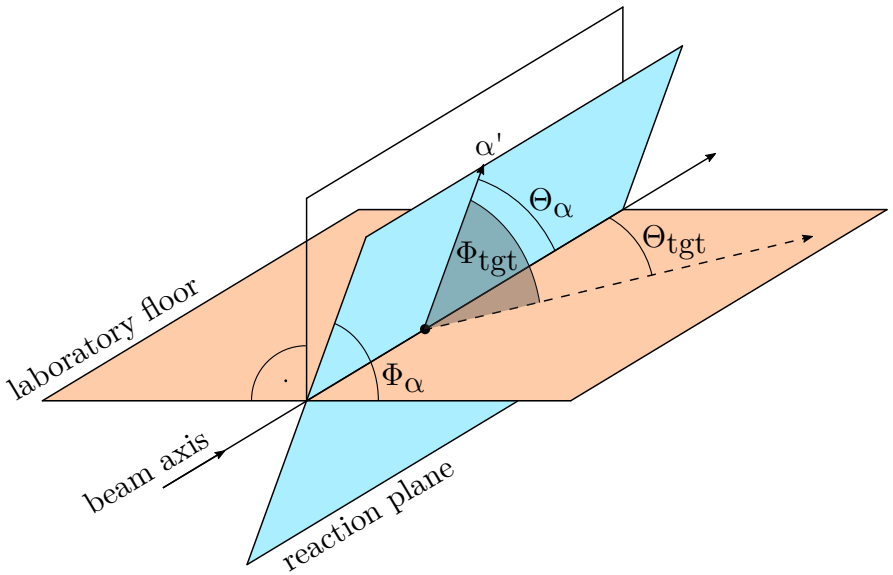

Figure 12: Coordinate system definition. The α-scattering angle Θ_α is determined by the direction of the scattered α particle and the beam axis, which also span the reaction plane. Its rotation around the beam axis is given by Φ_α. For the sieve-slit calibration, a different coordinate system was used. The target scattering angle Θ_{tgt} is given by the projection of the scattered α particles direction on the laboratory floor frame. It is equal to Θ_α when the reaction plane is parallel to the laboratory floor, i.e., $\Phi_\alpha = 0$. Φ_{tgt} is spanned by the α particle direction and its projection onto the laboratory floor frame. Coordinates in the $(\Theta_{tgt}, \Phi_{tgt})$ system can be converted to the $(\Theta_\alpha, \Phi_\alpha)$ system via eqs. 2.5a and 2.5b.

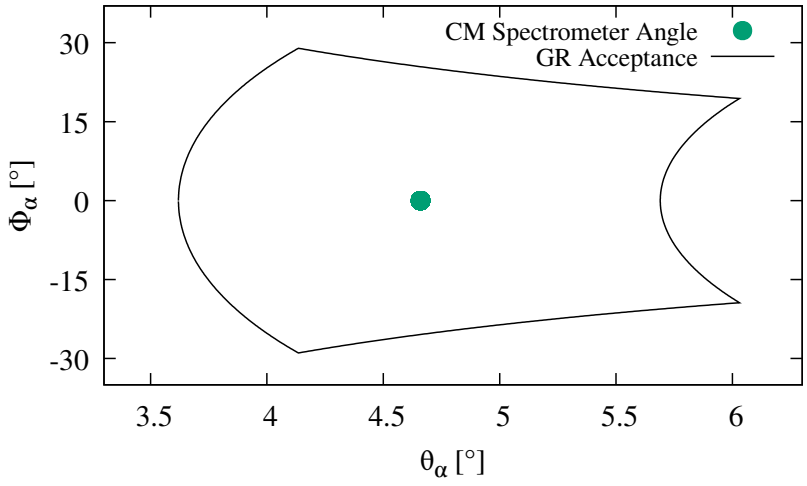

Figure 13: GR software acceptance in the center-of-mass frame in terms of Θ_α^{CM} and Φ_α^{CM}. The rectangular acceptance of $3.5° \leq \Theta_{tgt} \leq 5.5°$ and $\Phi_{tgt} \leq \pm 2°$ is transformed via Eqs. 2.5a and 2.5b and shifted to the center-of-mass frame in order to translate the rectangular acceptance to the coordinate system that is used for the DWBA calculations presented in Chapter 2.4.

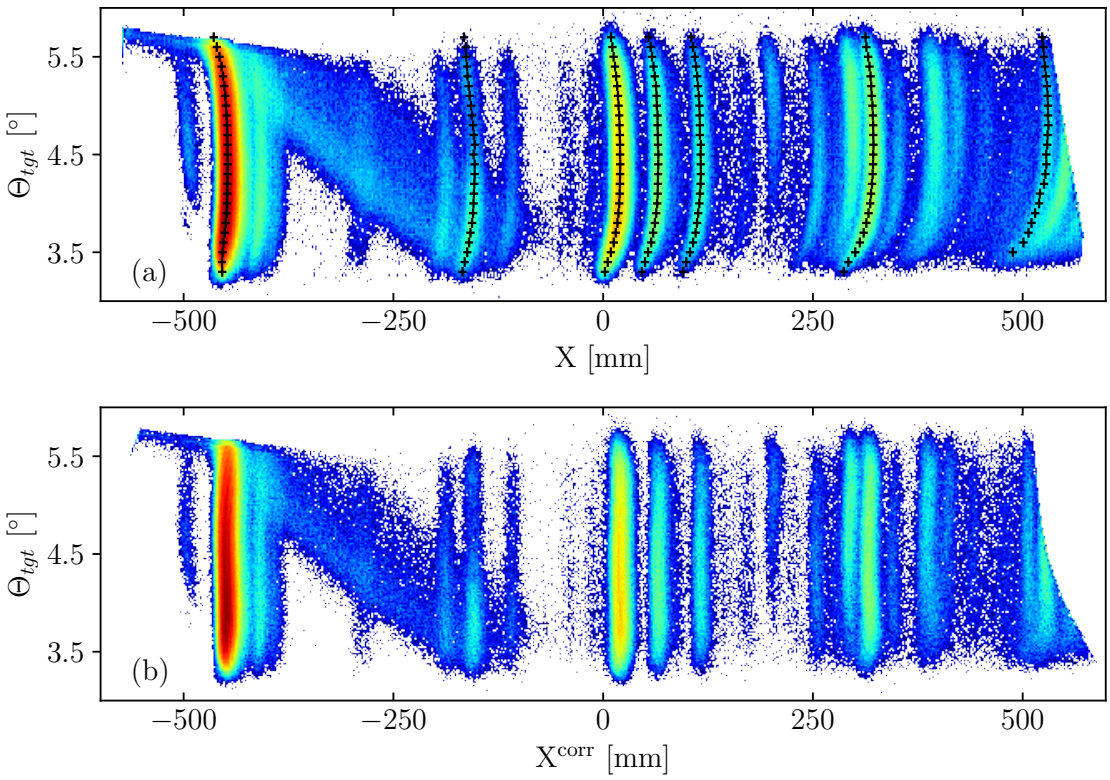

Figure 14: NatSi(α, α') data used for calibrating the $X^{corr}(\Theta_{tgt})$ correction given by Eq. 2.6. Panel (*a*) shows the uncorrected X and Θ_{tgt} data with the points used for calibration marked by black crosses. All data points were calibrated to the value at $\Theta_{tgt} = 4.5°$. Panel (*b*) shows the corrected data, now independent of Θ_{tgt}.

2.2.4 Correction of $X(\Theta_{tgt})$

Due to the ion optics of the spectrometer and the different flight paths of scattered α particles depending on Θ_{tgt}, the resolution in the final excitation energy spectrum can be greatly improved by correcting the X position for its dependence on Θ_{tgt}. A calibration measurement using a NatSi target was conducted with beam settings identical to the ^{120}Sn measurement. Figure 14 (*a*) shows the recorded NatSi data with several isolated excitations throughout the spectrometer X range, mostly stemming from ^{28}Si, the Si isotope with the highest natural abundance of 92.2 %. The marked shapes in Fig. 14 (*a*) were used to generate a set of parameters that minimize the spread in X using Eq. 2.6 with the parameters listed in Appendix A.3. The resulting corrected data are shown in Fig. 14 (*b*).

$$X^{corr} = \sum_{i=0}^{3} \sum_{j=0}^{3} p_{ij} \cdot X^i \cdot \Theta_{tgt}^j \tag{2.6}$$

2.2.5 Calibration to Excitation Energy

For the sake of brevity, the calibration procedure will only briefly be described here. A rough calibration of the excitation energy was performed based on the known excited states of ^{28}Si [54] in the NatSi measurement, which could be used for a first analysis of the $\alpha-\gamma$ coincidence data. However, due to the different target-nucleus mass a different energy loss in inside the target, a more precise calibration was necessary for the ^{120}Sn data. Several ground-state transitions of known excited states in ^{120}Sn were identified in the γ-ray coincidence spectra and were used to calibrate the corrected $\mathrm{X}^{\mathrm{corr}}$ information to excitation energy. The known states at 1171.25 keV, 2420.9 keV, 2930.5 keV, 3158.0 keV, 3284.6 keV, and 4006.5 keV [55] were identified unambiguously. In addition, an excited state at 4524 keV was used for calibration, as it was also observed in the ^{119}Sn$(d, p\gamma)$ experiment presented in Chapter 3. The excitation energy $\mathrm{E_X}$ in ^{120}Sn was then calibrated assuming a linear dependence on $\mathrm{X}^{\mathrm{corr}}$ given by

$$\mathrm{E_X[keV]} = 6343.579 + 11.03605 \cdot \mathrm{X}^{\mathrm{corr}}[\mathrm{mm}]. \tag{2.7}$$

The justification of a simple linear calibration throughout the accessible energy range was validated by investigating the residual energies determined from the NatSi calibration. These deviated only within $\pm$5 keV from the calibrated values, which is negligible within the corrected spectrometer resolution of FWHM$(\mathrm{E_X}) \approx 120$ keV throughout the energy range.

2.3 The CAGRA Clover-Array

The following section describes the data preparation needed for the best possible energy and time resolution of the γ-ray detectors, as well as the full-energy-peak efficiency and dead time determination. The mounting rig of the CAGRA array was designed especially for the CAGRA+GR campaign and detectors were brought to RCNP by members of the *Clover Share* collaboration. Eight of the twelve HPGe Clover detectors were provided by Argonne National Laboratory (ANL, USA), two by the U.S. Army Research Laboratory (ARL, USA), and two by the Institute for Modern Physics (IMP, China). All twelve Clover detectors were mounted inside active BGO Anti-Compton shields. Four additional 3"x8" $LaBr_3$:Ce detectors were supplied by the Instituto Nazionale di Fisica Nucleare (INFN) in Milano, Italy. The LaBr detector positions at 45° relative to the beam axis were labeled as CAGRA positions 1–4 , the HPGe Clover positions at 90° were labeled as positions 5–12 , and the detectors at 135° were labeled as positions 13–16 Each Clover leaf was then labeled A, B, C, or D. A complete list of all detector positions is given in Appendix A.4. While the LaBr detectors were read out by the resident GR data

acquisition system, the 48 Clover crystal signals were sampled by digitizers developed for the GRETINA spectrometer [56] with a special firmware used for Gammasphere [57]. These featured a 100 MHz 14 bit analog-to-digital converter (ADC) per channel and an onboard digital filter algorithm that allowed to store individual timestamps, filter sums, and additional sample information used for offline energy determination of each detector hit. During the ^{120}Sn$(\alpha, \alpha'\gamma)$ experiment, the Clover crystals were operating at average count rates of approx. 15 kHz per crystal, while the overall trigger rate in coincidence with the GR spectrometer was 4–5 kHz. All γ-ray detectors were shielded with passive Pb and Cu absorbers of varying thickness in order to reduce the overall detector rate. For an independent dead time determination, a pulser signal at a rate of 103 Hz was connected to the test input of 30 Clover crystal preamplifiers and the CAGRA DAQ trigger input. Out of the 48 available HPGe crystals, 44 were functioning properly and 42 of them could be calibrated and used in the analysis.

2.3.1 γ-ray Energy Resolution

All experiments performed during the CAGRA+GR campaign suffered from suboptimal HPGe energy resolution in the order of 10–12 keV at 1 MeV γ-ray energy, as has been reported in the results published since the campaign [58–60]. In the following, a procedure to obtain the best possible resolution will be presented together with an explanation for the cause of the deteriorated resolution.

Figure 15 shows the information stored by the digitizer firmware and available in the offline analysis. A digitial leading-edge trigger provides a timestamp for each hit and triggers the read out of two continuously acquiring filter sums which integrate over the signal before and after the rising edge (pre_sum and post_sum). The length of the integration window is shown as $\mathrm{T_{shape}}$ in Fig. 15, in analogy to conventional analog filter amplifiers, and was set to 3.5 µs during data taking. The separation window between the two filter sums results from additional time windows that position the summing windows relative to the trigger. It is simplified as $\mathrm{T_{pause}}$ here and amounted to 1.26 µs. For very low rate scenarios, the pulse height E of the signal can be obtained by simply subtracting the two filter sums:

$$\mathrm{E} = \mathrm{post\_sum} - \mathrm{pre\_sum} \tag{2.8}$$

At realistic count rates of several kHz, however, pulses will stack on top of each other and additional corrections have to be applied. Assuming two pulses close in time, but separated well enough to process both of them, the second pulse is in reference to an exponentially decaying baseline instead of a constant one, as shown in Fig. 15. Thus,

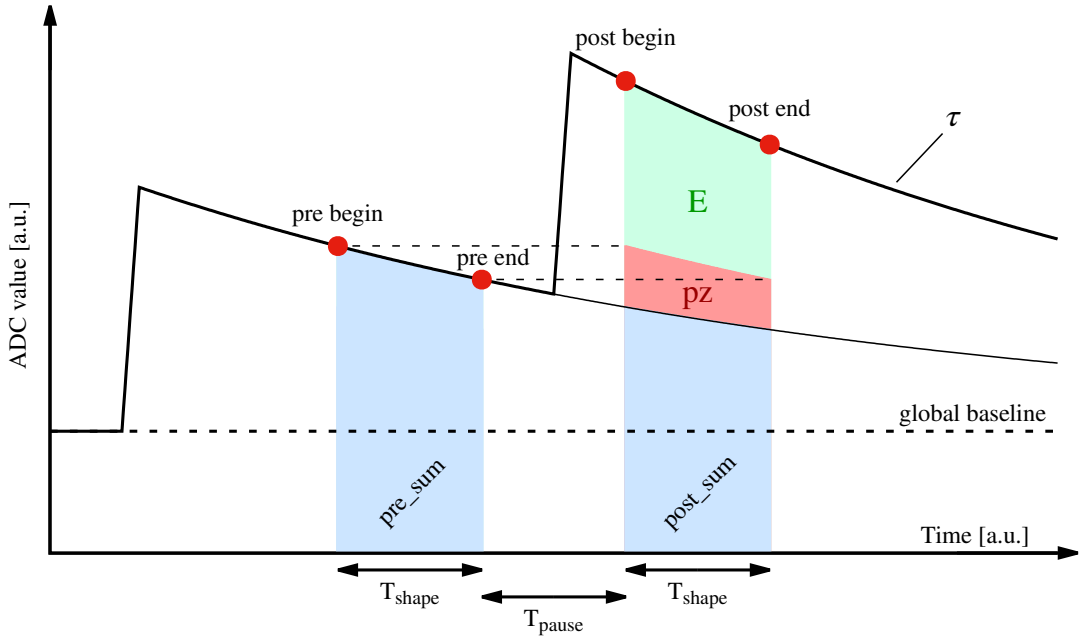

Figure 15: Pulse height determination for the second shown pulse with the information available in the CAGRA raw data. The digitizer firmware stores the timestamp of the leading-edge discriminator (not shown here), the two filter sums before and after the rising edge of the detector signal (pre_sum and post_sum), the ADC values at the beginning and end of each summing window (pre/post begin/end), and the average global baseline determined from the online filter algorithm. Both filter sums integrate the full signal over a time window $\mathrm{T_{shape}}$ and are separated by the time $\mathrm{T_{pause}}$. Note that the areas *pz* and *E* are calculated during the offline analysis.

when subtracting the two filter sums, the energy is underestimated by the area labeled as pz in the figure, again in analogy to the pole-zero correction used in analog signal processing. This underestimation can be corrected for based the exponential decay time τ of the preamplifier signal, the average global baseline (bl), and the time between the two summing windows Δ_T:

$$\mathrm{pre} = \mathrm{pre\_sum} - \mathrm{bl}$$

$$\mathrm{post} = \mathrm{post\_sum} - \mathrm{bl}$$

$$\Delta_\mathrm{T} = \mathrm{T_{pause}} + \mathrm{T_{shape}}$$

$$\mathrm{pz} = \exp\left(\frac{\Delta_\mathrm{T}}{\tau}\right) \tag{2.9a}$$

$$\mathrm{E} = \mathrm{post} - \mathrm{pre} \cdot \mathrm{pz} \tag{2.9b}$$

For an optimal compensation of this rate effect, the τ parameter has to be optimized. Recorded detector traces from a $^{206}\mathrm{Pb}(\alpha, \alpha'\gamma)$ measurement were investigated and the exponential decay time τ was fitted. However, the fitted parameters did not yield the

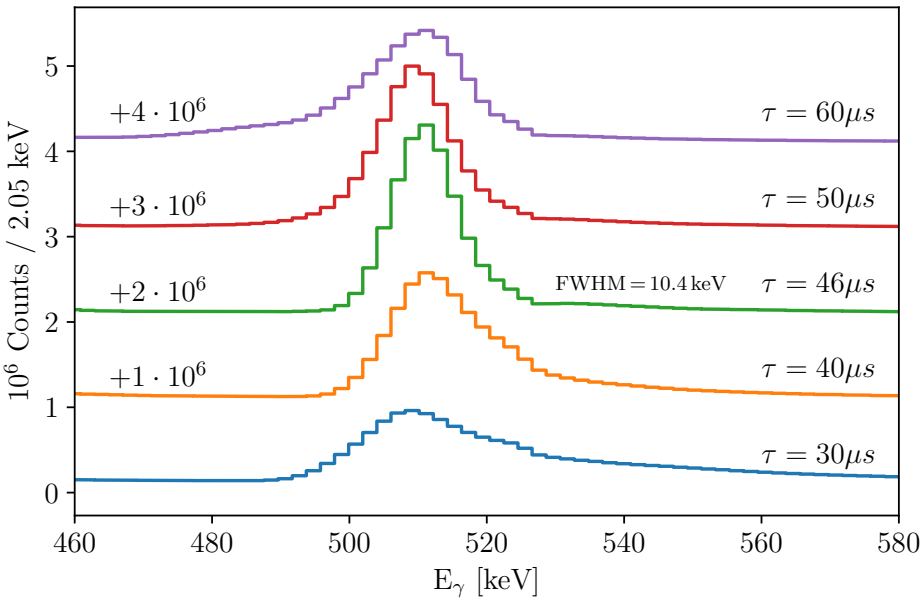

Figure 16: Parameter scan for Clover crystal 8D. Resulting peak shapes at 511 keV are shown for exemplary τ parameters including the optimal value of 46 µs. The best resolution achievable is FWHM = 10.4 keV for this crystal and is representative for all other crystals.

best possible energy resolution. Instead, a parameter scan for each crystal was performed over a range of τ = 30–60 µs in steps of 0.5 µs using ^{120}Sn$(\alpha, \alpha'\gamma)$ data. Figure 16 shows exemplary peak shapes for the 511 keV peak of one crystal. The optimal τ value for each crystal was chosen based on the best FWHM and the most symmetrical peak shape.

Even though the τ parameter was optimized and the rate and baseline dependence was diminished, the obtained energy resolution of all crystals was approx. 11 keV at 511 keV and stayed rather constant at higher energies (13 keV at 1171 keV, 15 keV at 3152 keV). This behavior could be traced back to an improperly set time window for the separation between the trigger and the second filter window. Since the digitizer firmware was set up to store a number of samples, the beginning of the post_sum window was found to be too close to the rising edge of the signal. Figure 17 shows a signal of detector 12A with negative polarity from the ^{206}Pb$(\alpha, \alpha'\gamma)$ measurement. No such traces were recorded during the ^{120}Sn$(\alpha, \alpha'\gamma)$ measurement. It has to be concluded that this unfortunate setting, which affects all measurements of the campaign, cannot be corrected in the offline analysis and a high-resolution state-by-state analysis of the data in the high-energy region is not possible.

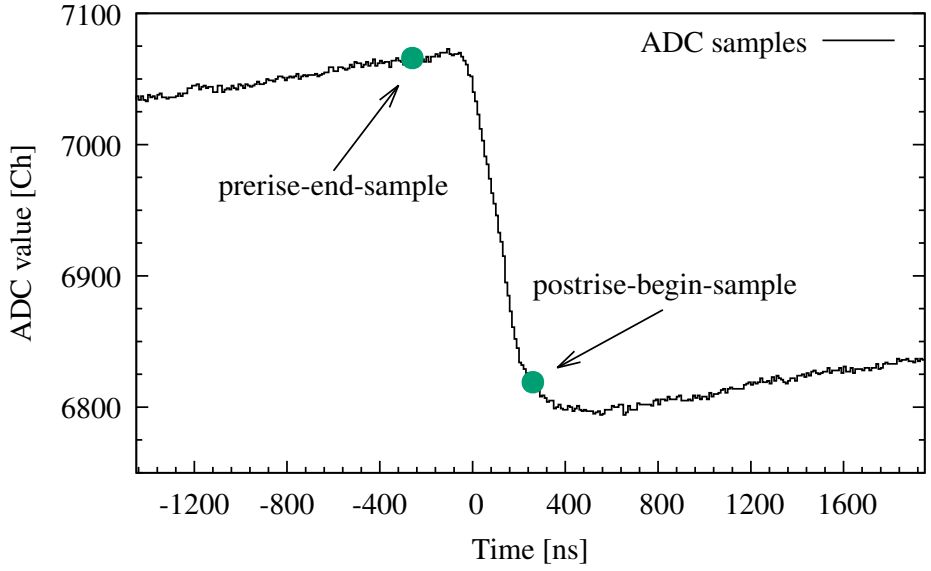

Figure 17: Recorded signal trace of detector 12A with negative polarity from the ^{206}Pb$(\alpha, \alpha'\gamma)$ measurement. Time is given relative to the trigger timestamp of the signal. An improper placement of the beginning of the second filter window on the rising edge is observed.

2.3.2 Time-Walk Correction

A common effect of data acquisition systems using leading-edge triggers is the pulse height dependent time-walk or amplitude walk [61]. Assuming two signals are emitted at the same time with different pulse heights, the smaller pulse will exceed the trigger threshold later than the larger pulse, causing a shift towards later timestamps and a broadened prompt peak in the coincidence time spectrum. A similar effect can be induced by different signal shapes of the rising edge depending on the interaction point of the γ-ray inside the detector, but is not accounted for here. In order to quantify and correct the pulse height dependent time-walk, the time difference between each Clover crystal and the RF signal from the AVF cyclotron ($\Delta_\mathrm{T} = \mathrm{T}_\gamma - \mathrm{T}_\mathrm{RF}$) was investigated in correlation to the pulse height (q) using ^{120}Sn$(\alpha, \alpha'\gamma)$ data. Figure 18 shows the original and corrected time-pulse-height matrices calibrated to γ-ray energy. However, the time walk correction depends only on the pulse height in channels, regardless of the physical γ-ray energy. A simple exponential dependence has been fitted to the data in order to correct the time-walk effect:

$$\Delta^\mathrm{corr}(\mathrm{q}) = a + b \cdot \exp \frac{-(c + \mathrm{q})}{d} \tag{2.10}$$

The corrected time difference $\Delta_\mathrm{T}^\mathrm{corr} = \Delta_\mathrm{T} - \Delta^\mathrm{corr}(\mathrm{q})$ was used to apply a prompt and background gate in the coincidence analysis presented in Chapter 2.5.

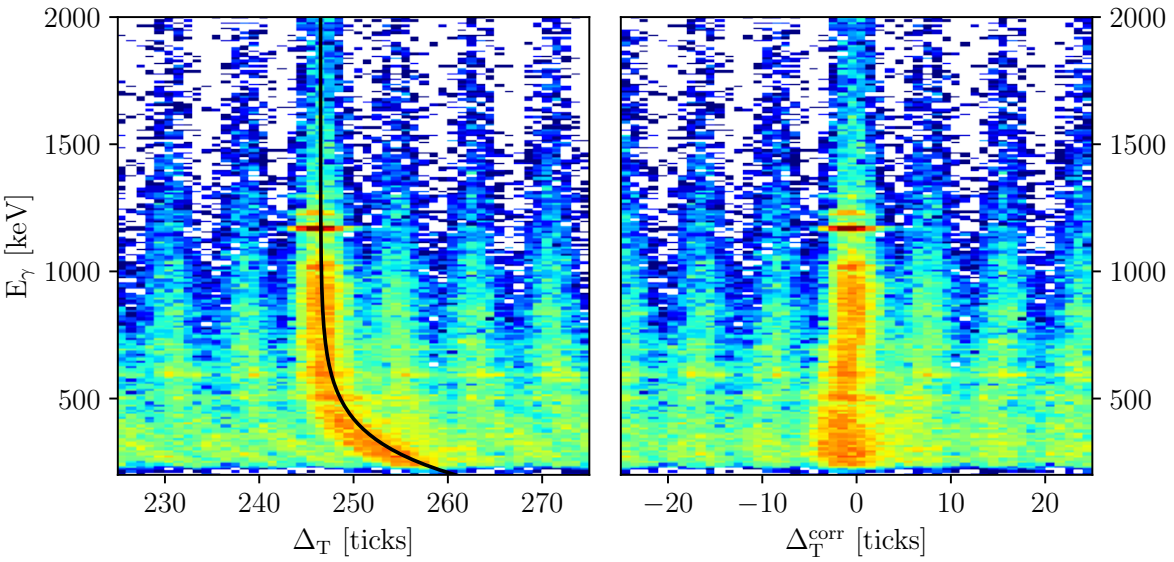

Figure 18: HPGe time walk of detector 8D calibrated to γ-ray energies for visualization. *Left*: original dependence of trigger time on pulse height. The black line indicates the fitted exponential correction (Eq. 2.10). *Right*: Corrected timing with no dependence on pulse height and adjusted for the constant offset of 247 ticks = 2.47 µs. The accumulation of hits at 1171 keV originates from the decay of the first excited state in ^{120}Sn.

2.3.3 γ-ray Efficiency Determination

The absolute Full-Energy-Peak (FEP) efficiencies of each γ-ray detector have been determined up to 3.45 MeV using a ^{60}Co source of known activity and a ^{56}Co source. The activity of the ^{56}Co source was scaled to the ^{60}Co source assuming identical efficiencies for the two transitions at nearly identical energies of 1173.2 keV and 1175.1 keV. The summed efficiency of all 42 operating HPGe detectors was $\epsilon_{\mathrm{FEP}} = 1.405\,\%$ at 1.332 MeV and $\epsilon_{\mathrm{FEP}} = 0.277\,\%$ at 6 MeV. The extrapolation for energies above 3.45 MeV was performed using a simple exponential behavior, which is validated by the distinct γ-ray angular distributions observed at high energies (see Chapter 2.4). Since only the ^{60}Co measurement is giving absolute efficiencies, a dead time correction is desirable and the dedicated pulser was connected to the crystals during the measurement. The analysis of integrated pulser counts yielded a dead time of approx. 95 % for each crystal and it is thus assumed that the pulser settings listed in the log books were incorrect. However, the average count rate per crystal was rather low at approx. 300 Hz and a negligible dead time is assumed for this measurement. Chapter 2.4 explains how the dead time correction for coincidence data was performed.

2.4 DWBA Prediction of $\alpha-\gamma$ Angular Correlations and Dead Time Correction

The calculation of $\alpha-\gamma$ angular correlations based on Distorted-Wave-Born-Approximation calculations (DWBA) is a standard procedure for spin and parity assignment in α-scattering experiments at forward scattering angles [41, 62–64]. In this work, the codes CHUCK3 [65, 66] and AngCor [67, 68] have been used to determine the expected γ-ray intensities for each detector and, thus, identify the electric dipole character of transitions in the high energy region. In addition, a dead time correction has been implemented based on the expected γ-ray distribution for the first excited state in ^{120}Sn and the excitation cross section known from the GR singles data. A collection of both codes, analysis scripts, and documentation has been published online recently [68].

DWBA calculations have been used extensively to investigate the angular dependence of direct scattering and transfer reactions, as well as to correlate, e.g., the scattering angle to the emission angle of any decay product (γ-ray or particle) [69–71]. Here, the simplified case of inelastic scattering of α particles and γ-ray emission into the $J^\pi = 0^+$ ground state of an even-even nucleus is assumed [72, 73]. After the scattering reaction, excited nuclei are polarized and the magnetic m-substates describe the projection of the nuclear spin to the quantization axis, which is chosen to be perpendicular to the reaction plane. CHUCK3 was used to calculate the scattering amplitudes T^{jm}, which describe both the population of an excited state with spin j and the m-substate distribution depending on the α-scattering angle Θ_α:

$$T^{jm} = p^j_m \sqrt{\left(\frac{d\sigma}{d\Omega_\alpha}\right)_j} \tag{2.11}$$

Here, p^j_m describes the m-substate population of a state with spin j. The optical-model potential parameters needed for DWBA calculations were adopted from a global parametrization [74]. ANGCOR was then used to take the scattering amplitudes and, especially, the p^j_m populations to calculate the correlation function of γ-rays in the center-of-mass frame:

$$W(\Theta_\gamma, \Phi_\gamma) = \sum_\sigma \left[\sum_m (-1)^m \, p^j_m \, e^{-im\Phi_\gamma} \, d^j_{m\sigma}(\Theta_\gamma) \right]^2 \tag{2.12}$$

The sum over σ relates to the possible polarization of the γ-rays which was not observed by the γ-ray detectors and the polar and azimuthal angles Θ_γ and Φ_γ are defined in analogy to the $(\Theta_\alpha, \Phi_\alpha)$ system shown in Fig. 12. ANGCOR takes into account the finite opening angle of γ-ray detectors via angular-correlation attenuation factors [75] and generates a $W(\Theta_\gamma, \Phi_\gamma)$ distribution for a given Θ_α. Due to the finite opening angle of the GR spectrometer, the output of ANGCOR has to be averaged over the acceptance

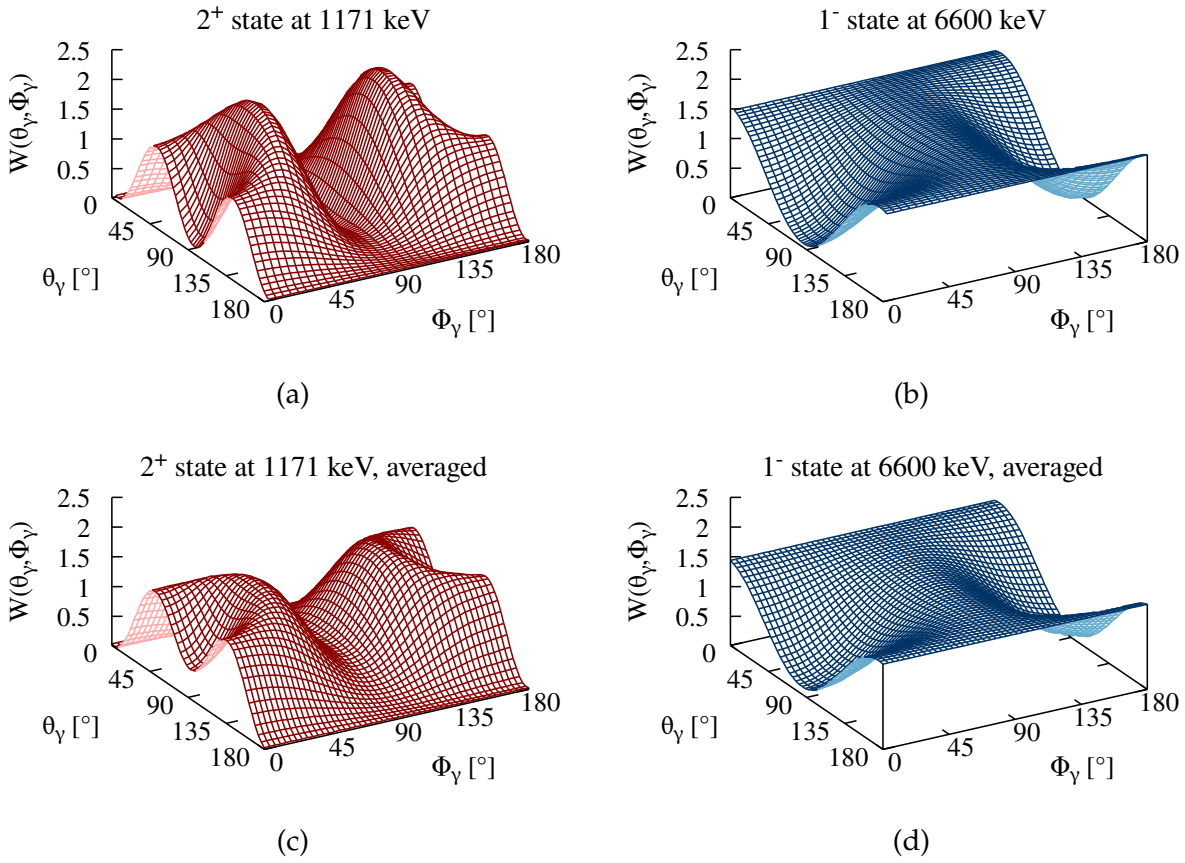

Figure 19: DWBA γ-ray angular distributions in the laboratory frame for the first excited ($J^\pi = 2^+$) state of ^{120}Sn at 1171 keV (*a*) and a generic $J^\pi = 1^-$ state at 6600 keV (*b*). Panels (*c*) and (*d*) show the distributions averaged over the acceptance of the spectrometer. Note that the dampening effect is more pronounced for the $J^\pi = 2^+$ state.

(see Fig. 13). While Θ_α can simply be adopted from the transformed acceptance, each Φ_γ value was shifted by the rotation of the α particle direction around the beam axis Φ_α to account for the different relative placement of each γ-ray detector. The averaging procedure samples over the rectangular acceptance in the $(\Theta_{tgt}, \Phi_{tgt})$ system and weights each point by the DWBA cross section given by CHUCK and by $\sin(\Theta_\alpha)$ due to the transformation to the spherical coordinate system $(\Theta_\alpha, \Phi_\alpha)$. Figure 19 shows the final γ angular distributions in the laboratory frame for the first excited $J^\pi = 2^+$ state in ^{120}Sn at 1171 keV and a generic $J^\pi = 1^-$ state at 6600 keV. Since the α particles are not polarized, the distributions are mirror symmetric to the reaction plane and only the range from $\Phi_\gamma = 0$–$180°$ is shown. The dampening effect due to the GR acceptance is evident for the $J^\pi = 2^+$ state, but less pronounced for the $J^\pi = 1^-$ state. Figure 20 shows the expected distributions for the $\Theta_\gamma = 90°$ and 135° Clover detector rings, which are clearly distinguishable. Due to the ground-state decay gate applied in the coincidence analysis and the favored excitation of natural-parity states in α scattering, only these

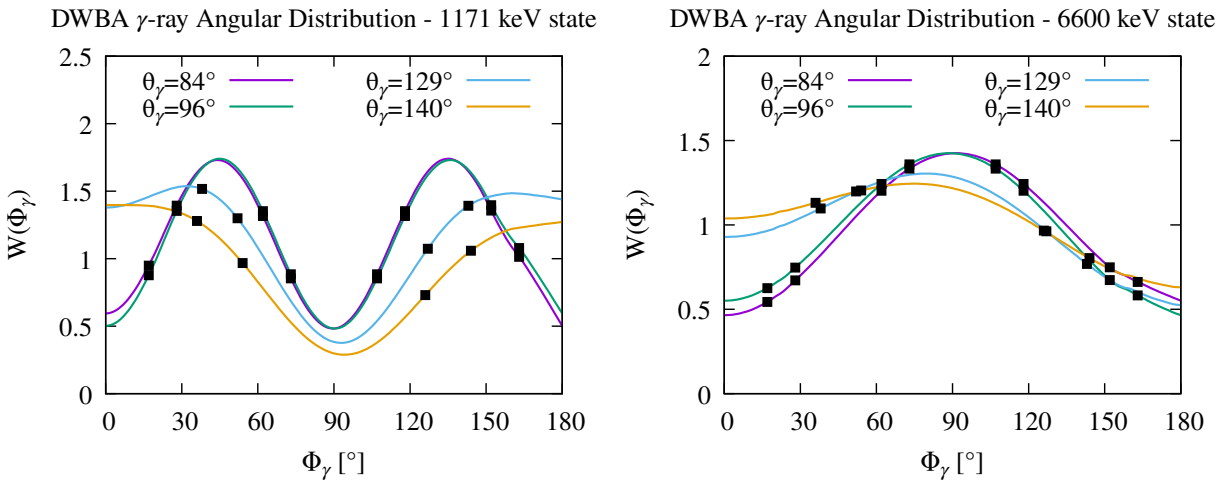

Figure 20: Averaged DWBA γ-ray angular distributions at precise Clover detector positions at $\Theta_\gamma = 84°, 96°, 129°, 140°$ for ground-state decays of the first $J^\pi = 2^+$ state at 1171 keV (*left panel*) and a generic $J^\pi = 1^-$ state at 6600 keV (*right panel*). Black squares indicate individual positions at respective Θ_γ angles for all 48 Clover leafs.

two types of states have to be investigated. Even though the averaged distributions differ slightly for the actual Clover leaf positions ($\Theta_\gamma = 84°, 96°, 129°, 140°$), all leafs in a ring were analyzed using the precise angles, but are added to groups of detectors labeled with $\Theta_\gamma = 90°$ or $\Theta_\gamma = 135°$ in the analysis in order to increase statistics per angle group.

Dead time determination

A reliable dead time information was not available for all HPGe crystals. The DWBA γ angular distributions were, thus, used to scale the efficiency corrected γ-ray yield of the direct excitation and decay of the first $J^\pi = 2^+$ state at 1171 keV in the coincidence analysis. The excitation cross section within the GR acceptance could be determined from a singles analysis of the same ^{120}Sn$(\alpha, \alpha'\gamma)$ data set and amounted to $\sigma^{2^+_1}_{\mathrm{GR}}$ =75.7 mb. Since the first $J^\pi = 2^+$ state can only decay to the ground state, the cross section determined from each γ-ray detector $\sigma^{2^+_1}_{\gamma}$ has to be equal to $\sigma^{2^+_1}_{\mathrm{GR}}$, when taking into account the dead-time free efficiency ϵ and angular distribution $W(\Theta_\gamma, \Phi_\gamma)$. The deviation ($\tilde{\sigma}^{2^+_1}_{\gamma}$) was then attributed to dead time effects and the live time τ_i^{live} of detector i was determined from the integrated counts A_i via

$$\tau_i^{\mathrm{live}} = \frac{\tilde{\sigma}^{2^+_1}_{\gamma,i}}{\sigma^{2^+_1}_{\mathrm{GR}}} \equiv \frac{A_i \cdot {\epsilon_i}^{-1} \cdot W(\Theta^i_\gamma, \Phi^i_\gamma)^{-1}}{A^{2^+_1}_{\mathrm{GR}} \cdot {\tau_{\mathrm{GR}}}^{-1}}, \tag{2.13}$$

where $A_{\mathrm{GR}}^{2_1^+}$ are the integrated counts of the 2_1^+ state in the GR singles data and τ_{GR} is the GR live time. Since no dead time correction could be performed for the ^{60}Co efficiency calibration measurement, τ^{live} values greater than 1 can occur and indicate that the ^{60}Co measurement was affected by dead time effects.

The experimental γ-ray angular distributions obtained with the normalization procedure described above are depicted in Fig. 25 an will be discussed in Section 2.5.

2.5 Coincidence Analysis

With the data conditioning described in the previous sections, a coincidence analysis was performed for the full ^{120}Sn$(\alpha, \alpha'\gamma)$ data set. The time difference Δ_{T} between γ-rays and spectrometer hits was used to select *prompt* and *background* events. Figure 21 shows the time difference spectrum with the prompt range chosen as $\Delta_{\mathrm{T}} \leq \pm 50\,\mathrm{ns}$ and the background range as $-200\,\mathrm{ns} \leq \Delta_{\mathrm{T}} \leq -100\,\mathrm{ns}$. The background range was chosen to be only on the negative side of the spectrum to exclude possible false background events from long-lived isomeric states. Valid spectrometer events inside the chosen software acceptance and γ-ray hits are then sorted into spectra and matrices with a weight of +1 for prompt events and -1 for background events. Figure 22 shows the background-subtracted coincidence matrix with the excitation energy on one axis

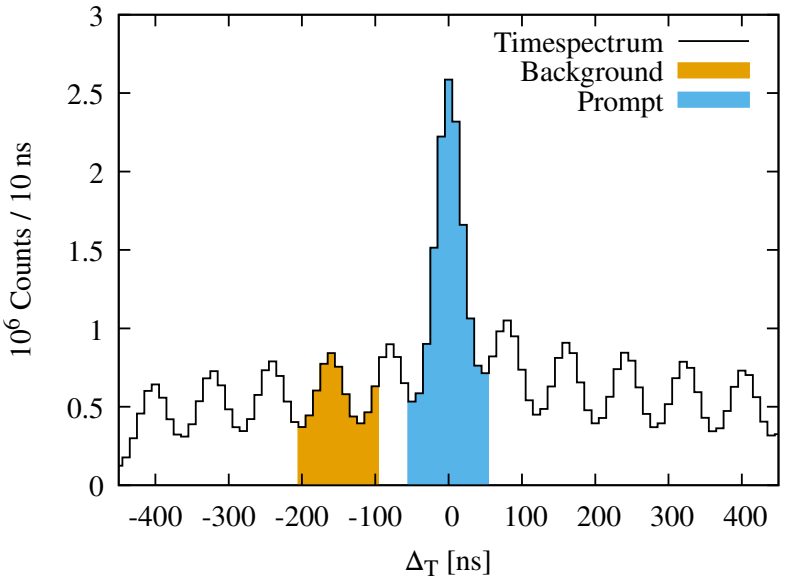

Figure 21: Time difference spectrum between γ-rays and spectrometer hits after time-walk correction. Coloured regions mark the *prompt* and *background* range of equal width. The pulsed cyclotron beam causes the oscillating structure with a time between bunches of 80.65 ns.

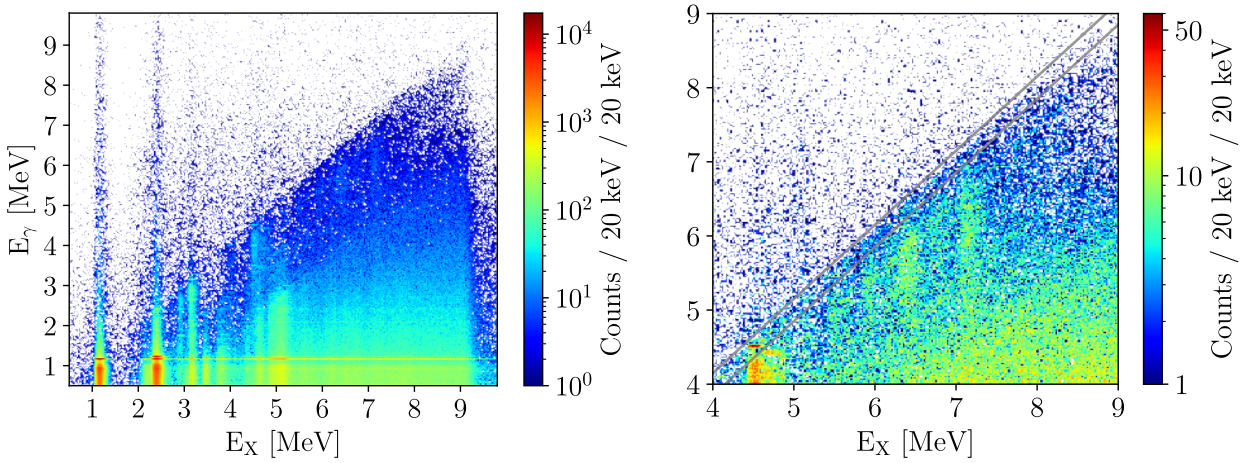

Figure 22: *Left*: Complete ^{120}Sn$(\alpha, \alpha'\gamma)$ coincidence matrix for all HPGe detectors. *Right*: Same matrix in the region above 4 MeV. Grey lines indicate the $\pm$150 keV wide diagonal gate on ground-state γ decays.

and the γ-ray energy on the other. Statistics drop off sharply at the neutron-separation threshold of $S_n = 9.1$ MeV. A projection of the full matrix to the excitation energy axis can be found in Fig. 23, which shows the excitation of discrete states at lower energies and the excitation of a region with much higher level density above 5 MeV up to S_n. The center diagonal in Fig. 22 represents the direct excitation of a given state and consecutive γ decay back to the ground state. It is, thus, called the *ground-state diagonal*. Off-diagonal events represent a given excitation and γ-decay branching to intermediate

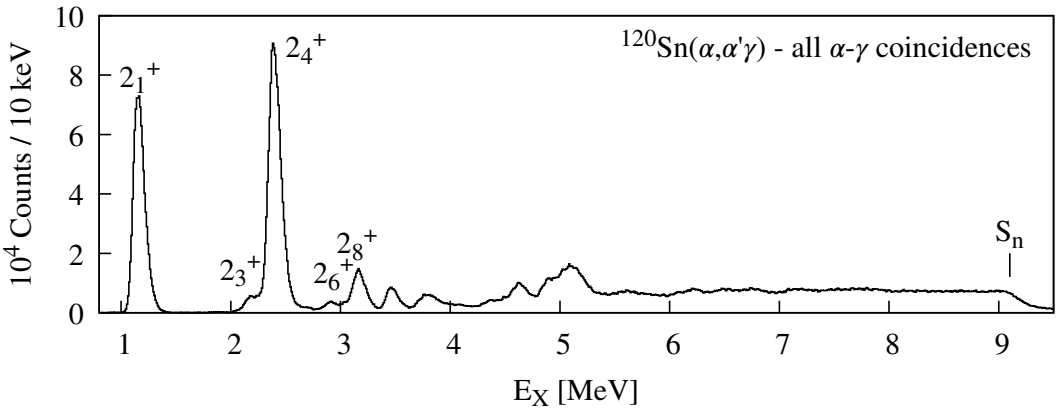

Figure 23: ^{120}Sn$(\alpha, \alpha'\gamma)$ Excitation energy spectrum of all $\alpha-\gamma$ coincidences after time-background subtraction. This spectrum is equal to the projection of the coincidence matrix to the excitation-energy axis. Strong excitations of known states in ^{120}Sn and the neutron-separation threshold are marked.

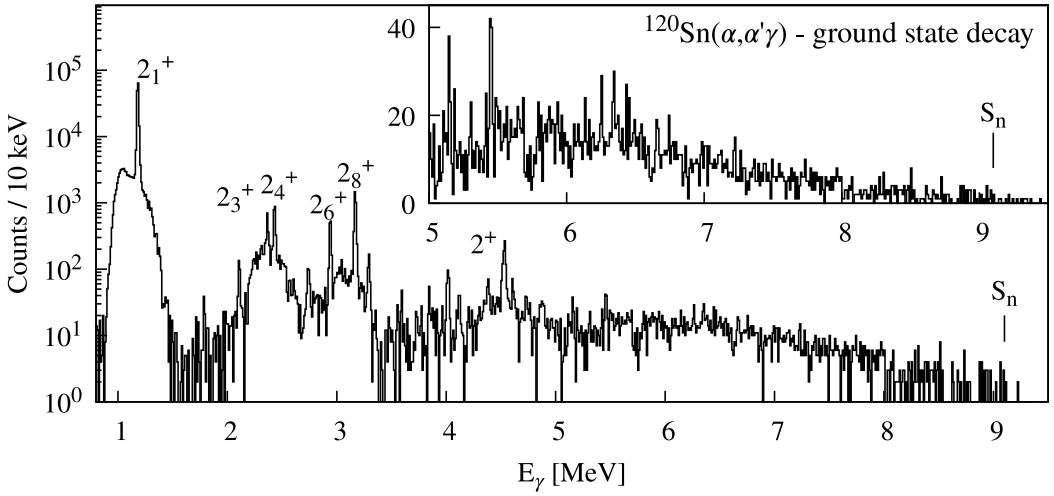

Figure 24: γ-ray spectrum gated on ground-state decays and after time-background subtraction. Known states in ^{120}Sn and the neutron-separation threshold are labeled. The inset shows the statistics in the high-energy region.

states. A diagonal gate in this matrix was applied with the condition

$$|\mathrm{E_X} - \mathrm{E}_\gamma| \leq 150\,\mathrm{keV} \tag{2.14}$$

to exclude decays to intermediate states and Compton-edge events in the HPGe detectors. The remaining events were then projected to the γ-ray energy axis. This analysis filter has proven to be very useful for the investigation of high-energy $J^\pi = 1^-$ states in particle-γ coincidence experiments [42, 44, 46, 60, 76] as it picks out decays from $J = 1, 2$ states in even-even nuclei. At high excitation energies, a given $J^\pi = 2^+$ state is expected to have a high decay branching to intermediate states, so the contribution to the ground-state diagonal gate is much reduced. In addition, the (α, α') reaction favors the excitation of $J^\pi = 1^-$ states at the chosen conditions [4]. It can be concluded that, if no distinct nuclear-structure features are present in the high-energy region that generate $J^\pi = 2^+$ states with a dominant ground-state decay, the complete high-energy region of the ground-state diagonal can be attributed to the decay of $J^\pi = 1^-$ states.

The full ground-state decay spectrum is shown in Fig. 24. At lower energies, it shows decays of known $J^\pi = 2^+$ states. At 4524 keV, a distinct peak is found which was observed as well in the ^{119}Sn$(d, p\gamma)$ experiment and shows the γ angular distribution of a $J^\pi = 2^+$ state in both experiments. In the region above 5 MeV only a continuous distribution is observed due to the suboptimal HPGe resolution and the expected high level density. The inset of Fig. 24 shows the high energy region with only about 0.5–2 counts/keV. However, due to the random-background subtraction and the narrow diagonal gate, all counts in this region can be attributed to ground-state decay γ-rays.

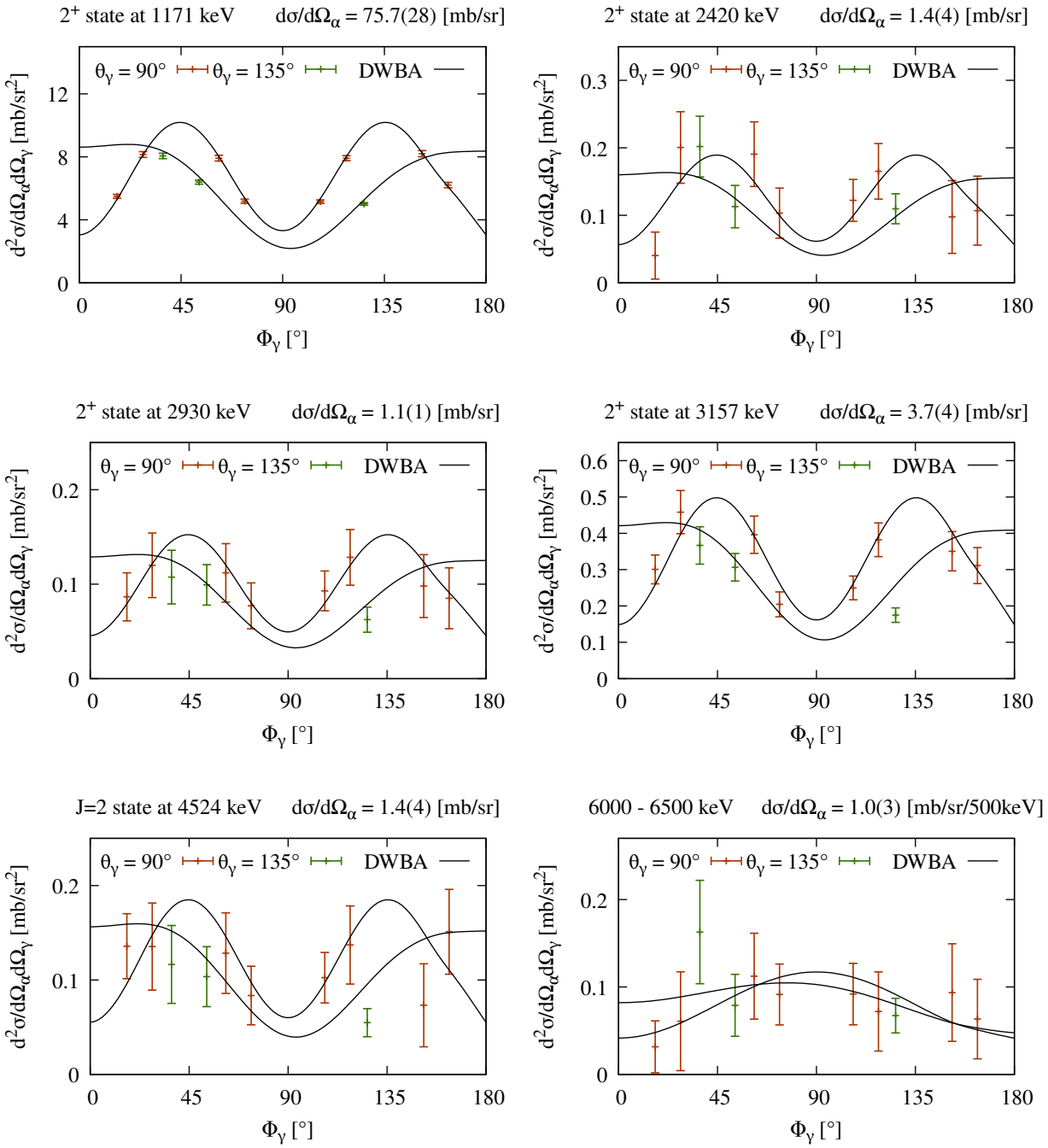

Figure 25: Experimental γ-ray angular distributions for ground-state decays compared to the expected DWBA distributions for $J^\pi = 2^+$ states at 1171 keV, 2420 keV, 2930 keV, 3157 keV, 4524 keV, and integrated between 6000 and 6500 keV where pure $E1$ decay is assumed. The 1171 keV state was used to normalize detector live times. The state at 4524 keV was identified as a $J^\pi = 2^+$ state in the ^{119}Sn$(d, p\gamma)$ experiment. Error bars show the statistical error in each angle group. Average distributions above 5 MeV can be found in Appendix A.5.

A similar analysis of the ground-state decays has been performed using the four LaBr detectors mounted under forward angles. However, they were placed at angles where the γ-ray distributions of $E2$ and $E1$ decays cannot be distinguished. They were intended to observe intermediate γ-rays due to decay branching instead of ground-state transitions. It was, thus, decided to not further investigate the ground-state decays with these detectors.

The γ angular distributions for five discrete $J^\pi = 2^+$ states and the range from 6000 keV to 6500 keV are shown in Fig. 25. The decent agreement to the expected DWBA distributions confirms the validity of the efficiency and dead time determination presented in Chapter 2.4, even above the energy range accessible in the ^{56}Co calibration measurement. Absolute values for double differential cross sections, folded with the average ground-state decay branching in the integrated energy region $\langle \mathrm{b}_0 \rangle = \langle \frac{\Gamma_0}{\Gamma} \rangle$, were determined via

$$\left\langle \mathrm{b}_0 \frac{d^2\sigma}{d\Omega_\alpha d\Omega_\gamma} \right\rangle = \frac{A_i}{N_t \; N_\alpha \; \Delta\Omega_\alpha \; \epsilon_i(E_\gamma) \; \tau_{\mathrm{GR}}^{\mathrm{live}}} \tag{2.15}$$

where A_i are the integrated counts in detector i, N_t is the effective target thickness taking into account target rotation, N_α is the accumulated number of beam particles, and $\Delta\Omega_\alpha$ and $\tau_{\mathrm{GR}}^{\mathrm{live}}$ are the opening angle of the spectrometer and its live time. Finally, $\epsilon_i(E_\gamma)$ is the DWBA normalized efficiency of detector i which encapsulates the dependence on the HPGe detector opening angle ($\Delta\Omega_\gamma$) and the respective detector live time (τ_i^{live}). The angular distributions shown in Fig. 25 can then be determined by averaging over the double differential cross sections within each angle group.

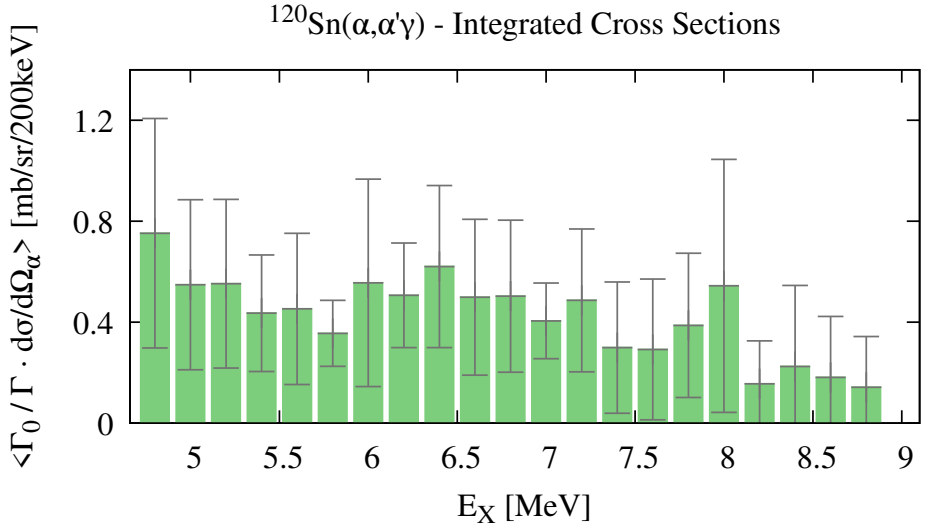

Figure 26: ^{120}Sn$(\alpha, \alpha'\gamma)$ integrated ground-state decay cross sections in 200 keV bins between 4.8 MeV and 9.1 MeV. Error bars indicate statistical errors only.

The final integrated differential cross section, folded with the ground-state decay branching b_0, is given by normalizing to the DWBA distribution $W(\Theta_\gamma, \Phi_\gamma)$ and averaging over all detectors:

$$\left\langle \mathrm{b}_0 \frac{d\sigma}{d\Omega_\alpha} \right\rangle = \sum_i^{N_{\mathrm{det}}} \frac{1}{N_{\mathrm{det}}} \left[\left\langle \mathrm{b}_0 \frac{d^2\sigma}{d\Omega_\alpha d\Omega_\gamma} \right\rangle \right]_i \cdot \frac{1}{W(\Theta_\gamma^i, \Phi_\gamma^i)} \tag{2.16}$$

Fig. 26 shows the integrated ground-state decay strength determined via Eq. 2.16 in bins of 200 keV from 5 to 9 MeV. See Appendix A.6 for a version with 500 keV wide bins. Due to the aforementioned conditions and assumptions on the ground-state diagonal, the observed strength is interpreted as pure $E1$ strength. Due to the low statistics, the errors are comparatively large and no sharp drop above approx. 7 MeV is observed, as could be expected from the data on ^{124}Sn [42]. However, the strength does decrease towards higher energies. A detailed discussion of these results and a comparison to other measurements will be given in Chapter 5.

3 ^{119}Sn$(d, p\gamma)$ Experiment with SONIC@HORUS

A preliminary analysis of the data set discussed in this Chapter was presented in a previous work [77]. In this thesis, however, and resulting from the development of the employed analysis software *psonar* [78], major improvements were made in the analysis. A Doppler correction was implemented which allowed the identification of three times as many individual transitions as in the previous work. The novel approach to γ-ray angular distributions developed in this work enabled, for the first time with SONIC@HORUS, the identification of spin $J = 1$ for states in the LEDR region. Due to recent (p, p') and (γ, γ') measurements on ^{120}Sn [79, 80], an $M1$ contribution in the region below 8 MeV could be excluded and a pure $J^\pi = 1^-$ character of the states observed in this experiment can be assumed. The setup and analysis steps identical to the previous work will only briefly be covered here and the improved steps will be explained in more detail. Final results were published in Ref. [76], together with the theoretical description presented in Chapters 4.2 and 4.4. A detailed discussion of the experimental results and a comparison to other data sets and the theoretical prediction is given in Chapter 5.

3.1 Setup and Measurement

The SONIC@HORUS setup has proven to be a powerful tool for nuclear-structure experiments [81–88]. A detailed explanation of the setup can be found in Refs. [89] and [90]. The ^{119}Sn$(d, p\gamma)$ experiment was performed with an average deuteron beam current of 20 nA at $\mathrm{E}_d = 8.5$ MeV impinging for 137 h on a self-supporting ^{119}Sn target of 0.39 mg/cm^2 thickness and an isotopic enrichment of 93.2 %. The Q value of the reaction was $Q = 6.88$ MeV, resulting in a maximum proton energy of 15.38 MeV. The SONIC chamber was in its initial configuration (SONIC-V1) with four silicon telescope-detectors mounted in two groups under backward angles of 122° and 131° relative to the beam axis and at a distance of 45 mm to target position. In order to perform particle identification using the $\Delta\mathrm{E} - \mathrm{E}$ technique, the first layer silicon detectors ($\Delta\mathrm{E}$ detectors) were 300 µm thick and the second layer detectors 1500 µm (E detectors). Since the active area (150 mm^2) and distance of the second silicon detector (55 mm) within each telescope determines the opening angle after successful particle identification, the overall angular coverage for detected protons was 1.57 % or 197 msr. The HORUS γ-ray spectrometer was equipped with 14 single-crystal HPGe detectors, of which six were mounted inside active Anti-Compton BGO shields. The summed full-energy-peak efficiency of the γ-ray detectors was 1.86 % at 1.3 MeV and 0.48 % at 6 MeV. Both silicon and HPGe detectors were read out using a digital data acquisition built around the DGF-4C, Rev. F modules by XIA LLC, the predecessor of the system presented in Chapter 6. An online multiplic-

ity filter was used with an $\mathrm{M} \geq 2$ filter condition, allowing only hits to be written to disk when at least two channels triggered within a coincidence window of 1 µs, regardless of the triggering detector type. A detailed explanation of the data acquisition system can be found in Ref. [84].

3.2 Data Preparation

The following section explains the data preparation performed before the coincidence analysis. As a first step, the raw data were corrected for differential non-linearities in the digitizer ADCs. This correction is necessary for all data taken with the XIA acquisition system and is especially important in high dynamic energy-range conditions, i.e., when measuring γ-rays at energies around and above 6 MeV with HPGe detectors. The initially severe full-energy-peak distortion could be restored by employing a previously developed correction procedure, which uses additional pulse-shape information stored by the digitizer firmware. The correction procedure is explained in more detail in Refs. [81, 91]. After restoring the HPGe energy resolution, an energy-shift tracking was performed in which the gain shift of each detector over time is determined and all data are aligned to the initial gain via a linear recalibration. This, again, improved the resolution in the accumulated spectra of each detector and the summed spectra. Since short prompt time windows are favorable in any coincidence analysis, a time-walk correction was applied similar to the case explained in Chapter 2.3.2. Since a continuous beam was used during the experiment, one of the $\Delta\mathrm{E}$ detectors was used as a reference detector for generating the time-energy matrices used for time-walk calibration of the HPGe detectors. The amplitude-dependent time walk $\Delta^{\mathrm{corr}}(\mathrm{q})$ was calibrated via the function

$$\Delta^{\mathrm{corr}}(\mathrm{q}) = \frac{a}{\sqrt{b \cdot \mathrm{q}}} + c, \tag{3.1}$$

where q is the uncalibrated pulse height and a, b, c are fitted parameters. In a second step, a time-walk-corrected HPGe detector was chosen as a reference detector for the generation of the time-energy matrices of all silicon detectors. Thereby, the time response of all detectors was corrected and the coincidence window used during the event building could be halved from ±375 ns to ±187.5 ns. The prompt window for the coincidence analysis of built events could be reduced from ±150 ns to ±62.5 ns.

Following the event building, proton events were identified via the $\Delta\mathrm{E} - \mathrm{E}$ technique and calibrated to excitation energy, as was presented in [77]. Despite the linear gain of silicon detectors, the excitation energy was calibrated with a polynomial of 3^{rd} order due to the non-negligible energy losses already inside the target and in the dead layers of both detectors, especially at low proton energies or high excitation energies. The ob-

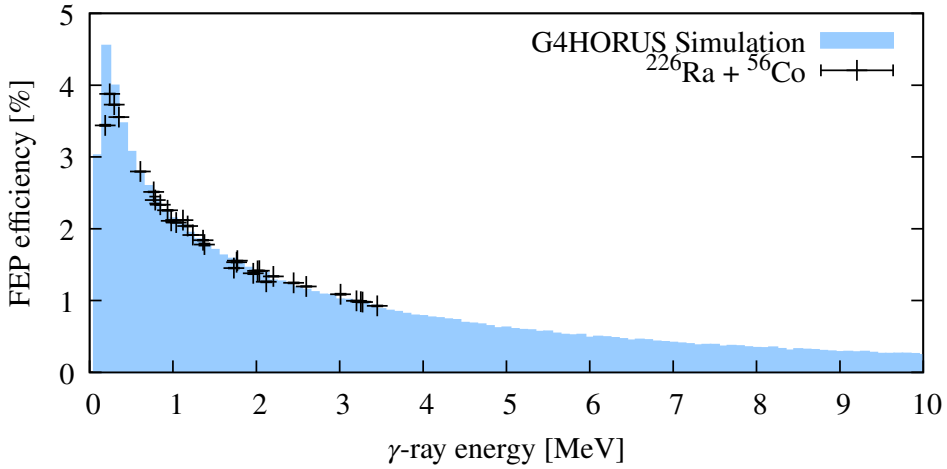

Figure 27: Summed FEP γ-ray efficiency of the HORUS array measured with ^{226}Ra and ^{56}Co sources. The filled area represents the optimized simulation of the efficiency performed with G4HORUS [93].

tained excitation-energy resolution (FWHM) was 88 keV at $E_X = 1.117$ MeV and 105 keV at $E_X = 6.6$ MeV. The γ-ray energy resolution after Doppler correction is discussed in Section 3.4 and the final coincidence matrix is shown in Appendix B.2.

3.3 Efficiency Simulation

Full-energy-peak γ-ray efficiencies were determined with a ^{226}Ra source of known activity and a ^{56}Co source. The ^{56}Co data were scaled to the ^{226}Ra source data to account for the decreasing activity of the source with a half-live of $T_{1/2} = 77.2$ d throughout the measurement. For the extrapolation to higher energies, a GEANT4 [92] based simulation was performed using the G4HORUS simulation package [93], which implements the SONIC@HORUS setup and precise detector geometries. Pb and Cu absorbers in front of HPGe detectors were added to the simulation and detector distances from target position were adjusted slightly to optimize the shape and height of the simulated efficiency of each detector. Figure 27 compares the measured and simulated total efficiencies up to 10 MeV.

3.4 Doppler Correction and Ground-State Decay Gate

A significant improvement in γ-ray energy resolution was obtained by implementing a correction for the Doppler shift of γ-rays depending on the emission angle relative to the direction of the recoiling nucleus, i.e., the Doppler angle θ_D. The SONIC@HORUS data set contains the complete reaction kinematics, i.e., the energy and direction of the beam, the reaction ejectile, and the emitted γ-ray. Therefore, the direction of the recoiling

nucleus can be calculated event-by-event. A detailed derivation of the formalism for calculating the Doppler shift depending on the excitation energy and detection angles is given in Appendix B.1. The relation between the lifetime of an excited state and the time scale of the slowing-down process is expressed by the experimental attenuation factor $F(\tau)$, which can be between 0 and 1. This value is commonly used to determine nuclear level lifetimes in Doppler-Shift-Attenuation (DSA) experiments [83, 94]. A value of $F(\tau) = 1$ means that the recoiling nucleus still has the full initial kinetic energy, while $F(\tau) = 0$ means that the nucleus is fully stopped at the time of γ-ray emission. For the correction applied in this work, it is assumed that the excited states have very short lifetimes compared to the slowing-down process, i.e., $F(\tau) = 1$. This assumption is validated for the high-lying $J^\pi = 1^-$ states by the great improvement of the energy resolution after Doppler correction, but is incorrect for the lower-lying $J^\pi = 2^+$ states with lifetimes in the order of ps to ns [55]. The lifetimes of excited $J^\pi = 1^-$ states in the LEDR region can be approximated from their width Γ. Typical values in ^{120}Sn were found to be in the order of 50–500 meV, resulting in lifetimes in the order of a few fs [50].

The unshifted γ-ray energy E_γ^0 can be determined via

$$\mathrm{E}_\gamma^0 = \frac{\mathrm{E}_\gamma(\theta_D)}{\left(1 + F(\tau) \cdot \frac{\mathrm{v}_R}{c} \cdot \cos\theta_D\right)}, \tag{3.2}$$

where $\mathrm{E}_\gamma(\theta_D)$ is the observed γ-ray energy, θ_D is the Doppler angle, and v_R is the initial velocity of the recoiling nucleus. Assuming a ^{119}Sn$(d, p\gamma)$ reaction at the given beam energy of 8.5 MeV, an ejectile (proton) detection angle of 130°, and an excitation energy of $\mathrm{E_X} = 6$ MeV, the recoiling nucleus has a kinetic energy of 354 keV ($\beta = 0.0025$) and is traveling in a direction 20.8° relative to the beam. The resulting Doppler shift of a γ-ray with $\mathrm{E}_\gamma = 6$ MeV emitted in-flight is then up to ±5 keV, depending on the emission angle. This strongly affects the summed γ-ray energy resolution when adding up spectra from different detectors.

Figure 28 illustrates the effect of the Doppler correction on the summed γ-ray spectra after gating on ground-state decays. The energy resolution (FWHM) is greatly improved from approx. 20 keV to below 10 keV at approx. 6.5 MeV γ-ray energy, which is close to the nominal resolution of single HPGe detectors at such energies. In several cases, individual peaks only appear after the correction and could not be analyzed in the previous work [77]. This Doppler correction was integrated into the analysis software *psonar* developed in this work [78] and is now a standard procedure for all SONIC@HORUS experiments investigating high-lying $J^\pi = 1^-$ states, as the energy shift is also evident

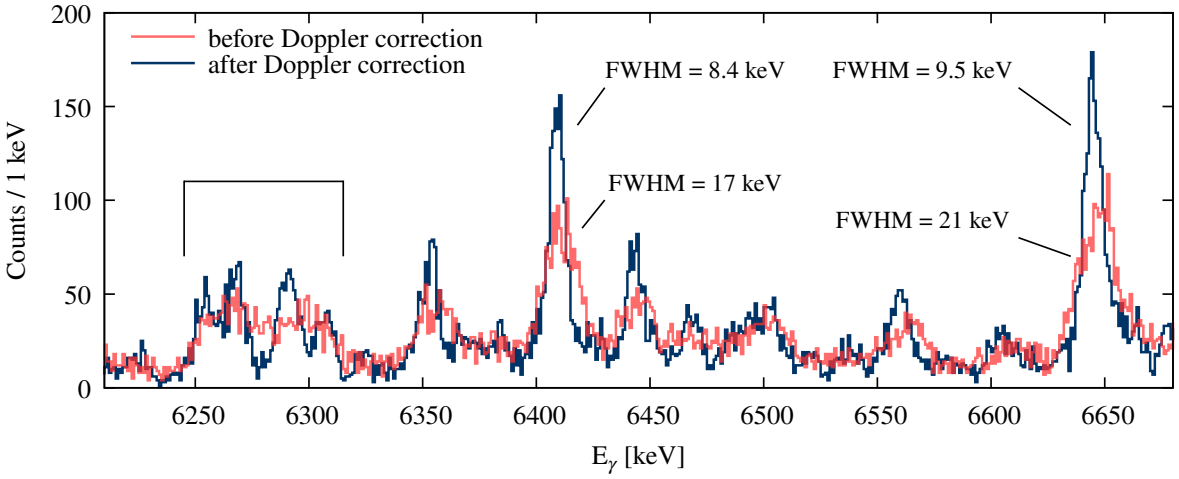

Figure 28: Effect of the Doppler correction on ^{119}Sn$(d, p\gamma)$ ground-state decays. In the marked region below 6300 keV four transitions emerge only after the correction. The FWHM of the two strongest transitions at 6408 keV and 6644 keV are marked before and after correction. These two lines were used to recalibrate and align all HPGe spectra before and after the correction, respectively.

in $(p, p'\gamma)$ experiments. In addition, the correction procedure can be used to determine experimental $F(\tau)$ values unequal to 1 for very weak transitions via the alternative DSA method recently developed [95].

The full data set has been sorted into an $E_X - E_\gamma$ coincidence matrix with a prompt window of ±62.5 ns, similar to the analysis presented in Chapter 2.5. The full matrix with all its details can be found in Appendix B.2. Figure 29 presents the final ground-state decay γ-ray spectrum obtained with the condition that $|E_X - E_\gamma| \leq 100$ keV after Doppler correction and random-background subtraction. At low energies, several known $J^\pi = 2^+$ states and a $J^\pi = 1^+$ state can be observed. Starting at approx. 5 MeV, a resonance-like accumulation of discrete transitions is found, which is most pronounced between 5.5 MeV and 7.5 MeV but extends up to the neutron-separation threshold at $S_n = 9.1$ MeV. While this bell-shaped structure was already observed in the previous analysis, in this work a total of 92 single transitions could be identified in the summed spectrum, instead of the previous 31. From these transitions, 69 were also observed and assigned with $J = 1$ in a recent high-sensitivity (γ, γ') experiment using bremsstrahlung [50]. The residual 23 transitions were likely not observed in the NRF experiment due to their low strength.

Note that at around 8.5 MeV, the sensitivity decreases for approx. 300 keV because the detected low-energy protons do not pass the first silicon detector and are stopped in its dead layer. For even higher excitation energies, the protons are fully stopped inside the

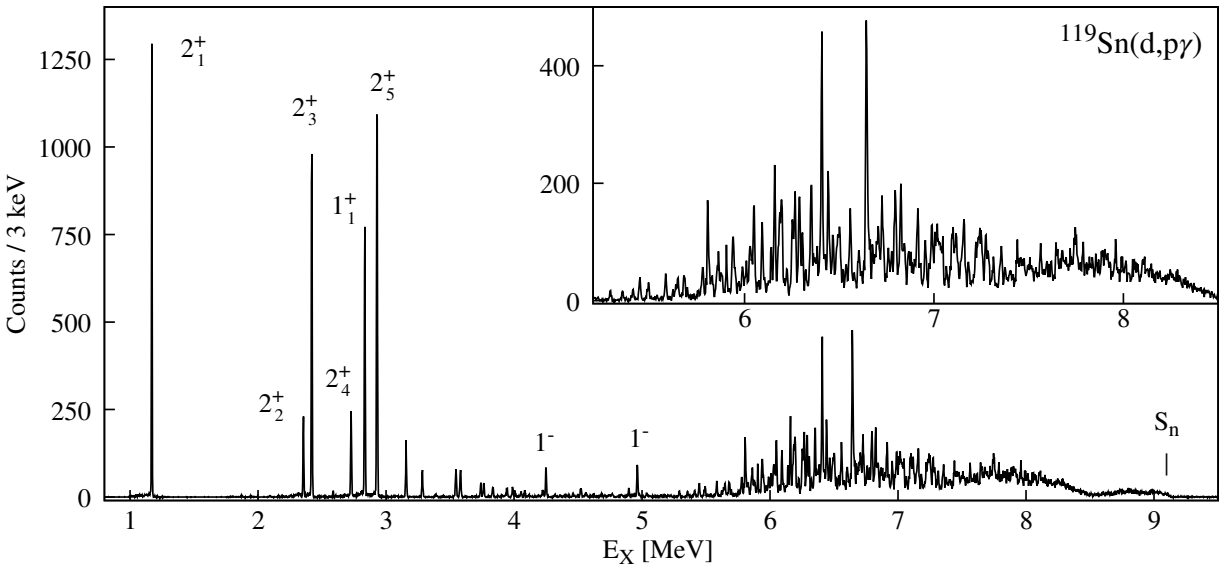

Figure 29: ^{119}Sn$(d, p\gamma)$ total ground-state decay spectrum after Doppler correction. Data from $\Delta\mathrm{E}{-}\gamma$ coincidences were scaled and included above 8.5 MeV. At lower energies, known transitions are labeled and above 5 MeV a resonance-like accumulation of discrete transitions emerges. The neutron-separation energy of $S_n = 9.1$ MeV is marked and the inset marks the region of interest. Figure adopted from Ref. [76].

active detection volume of the first detector and a coincidence analysis was performed without particle identification for these events. No discrete transitions could be identified in the ground-state decay gate. However, the summed spectrum was scaled according to the slightly different solid angle of the first-layer silicon detectors and added to Fig. 29.

Due to the very selective conditions imposed on the data (particle identification, random-background subtraction, Q value and $\mathrm{E_X}{-}\mathrm{E}_\gamma$ condition), the ground-state decay spectrum is completely free from contaminations and decays that stem from nuclei other than ^{120}Sn. For example, typical contaminations from elastic scattering on ^{12}C and ^{16}O are excluded due to the particle identification. Due to the target enrichment and the reaction Q value, contaminations from other Sn isotopes can be excluded. Finally, the excitation-energy resolution is good enough to impose a very narrow diagonal gate on ground-state transitions, which removes the detector response, i.e., Compton edges and escape peaks, from the spectrum. It can, thus, be concluded that every count in the spectrum is related to a high-lying excitation in ^{120}Sn and a potential $J^\pi = 1^-$ LEDR state in ^{120}Sn, even if no pronounced peak is formed. This combination of the ground-state diagonal gate and the (d, p) reaction allows a level of selectivity which exceeds the previous PDR studies with hadronic probes [44, 46, 96].

3.5 Angular Distributions

To further investigate the nature of the observed transitions, p-γ angular correlations were investigated in a novel approach. In previous works, angular correlations were calculated for SONIC@HORUS data sets with the DWBA codes CHUCK3 and ANGCOR in an attempt to identify spin and parity of excited states in several nuclei [97, 98]. However, a constant shift was observed between the calculated and experimental correlations and an assignment of J^π was only possible for transitions with high statistics since each detector combination had to be investigated separately. In order to be independent of a theoretical prediction and the reduced statistics at higher excitation energies, the data were sorted according to the Doppler angle θ_D of ground-state decay γ-rays in this work. Thus, the two-dimensional angular correlations are reduced to one-dimensional γ-ray angular distributions within a reference frame that changes for each event. These distributions were obtained for several states with known spin and parity to calibrate the characteristic distributions in a qualitative manner, as will be discussed later.

Since velocity and direction of a recoiling nucleus change depending on the excitation energy, a given detector combination observes a γ decay under a Doppler angle that, as well, depends on the excitation energy. For a final one-dimensional distribution, the number of possible detector combinations per angle group have to be determined. Figure 30 shows a finely binned normalization matrix generated by *psonar* [78] which can be used to normalize the summed efficiency and deadtime corrected yields in each angle group. It illustrates how the setup covers slightly different angles depending on the excitation energy.

Absolute γ-ray efficiencies are known from source measurements and simulation, but detector deadtimes during the ^{119}Sn$(d, p\gamma)$ experiment could not be determined due to the way the XIA acquisition system generates statistics information when using an online multiplicity filter [84]. Therefore, a deadtime normalization was performed assuming a mostly isotropic emission of the γ-ray de-exciting the 2_1^+ state when not in correlation with a detected proton, as the state is strongly fed from higher excitations. Since singles data were not available, the necessary spectra were filled by demanding that the time difference between γ-ray and proton was outside the prompt window. The γ-ray is uncorrelated to any proton and, thus, represents the distribution in the (non-existing) singles data. The intensities of the 1171 keV γ-ray were corrected for the (deadtime free) absolute γ-ray efficiency and normalization factors were determined for each HPGe detector. Due to their identical sizes and average count rates, silicon detector deadtimes were assumed to be similar among the four telescopes and, thus, irrelevant for a spin assignment via γ-ray distributions. However, this normalization procedure cannot yield

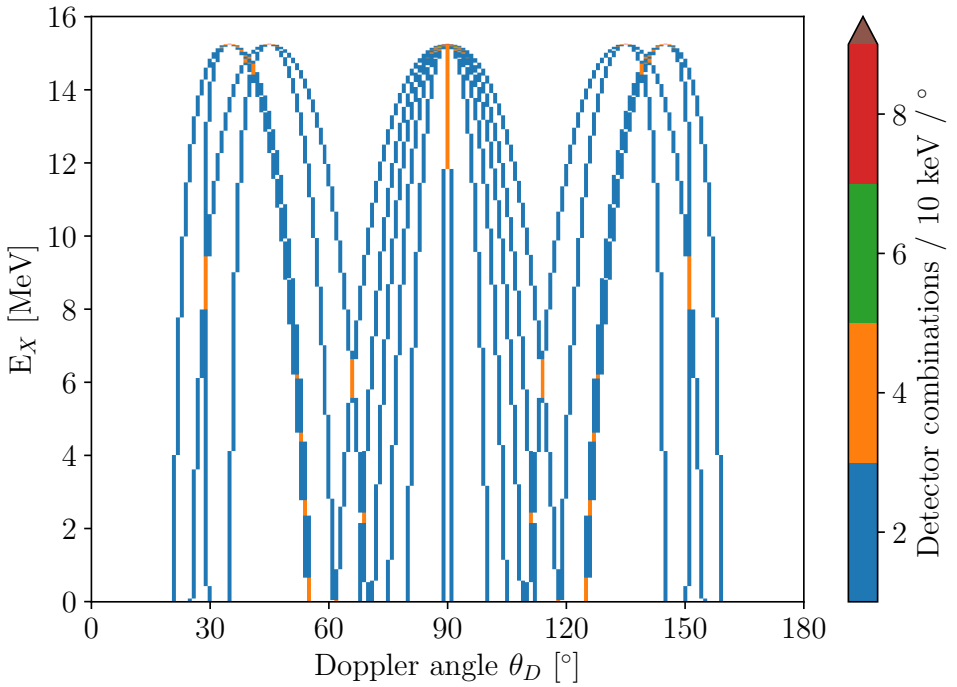

Figure 30: Distribution of $\Delta E - E$ and HPGe detector combinations observing γ decay under the Doppler angle θ_D. For a given beam energy and reaction, the direction of the recoiling nucleus and, thus, the Doppler angle of a γ-ray detected by a given detector, changes with the transferred kinetic energy. The latter can be related to the excitation energy E_X due to the measured complete kinematics of the reaction. This matrix is necessary to normalize the observed yield in each detector combination and determine the experimental γ angular distributions. See Appendix B.3 for this matrix with a θ_D binning of 10°.

absolute values for excitation cross sections, especially since the accumulated beam current cannot be read out with SONIC.

Figure 31 presents the obtained Doppler-angle γ-ray distributions for known states in ^{120}Sn with an angle binning of 10° obtained with the normalizations described above. Within each distribution, the yields per angle group are normalized to the highest yield, respectively. For known states with $J^\pi = 2^+$ and $J^\pi = 1^{+/-}$, clearly distinguishable shapes are observed which prove the capability to identify $J = 1$ and $J = 2$ states in the ground-state diagonal gate via this procedure. However, the procedure does not allow to separate states with positive and negative parity, as the distributions for $J^\pi = 1^+$ and $J^\pi = 1^-$ appear identical. Note that these distinct distributions were observed on the ground-state diagonal, where only decays from low-spin states are observed. Less distinguishable distributions are obtained for decays to the first excited state at 1171 keV and for decaying states with higher spin up to $J = 4$, which can be found

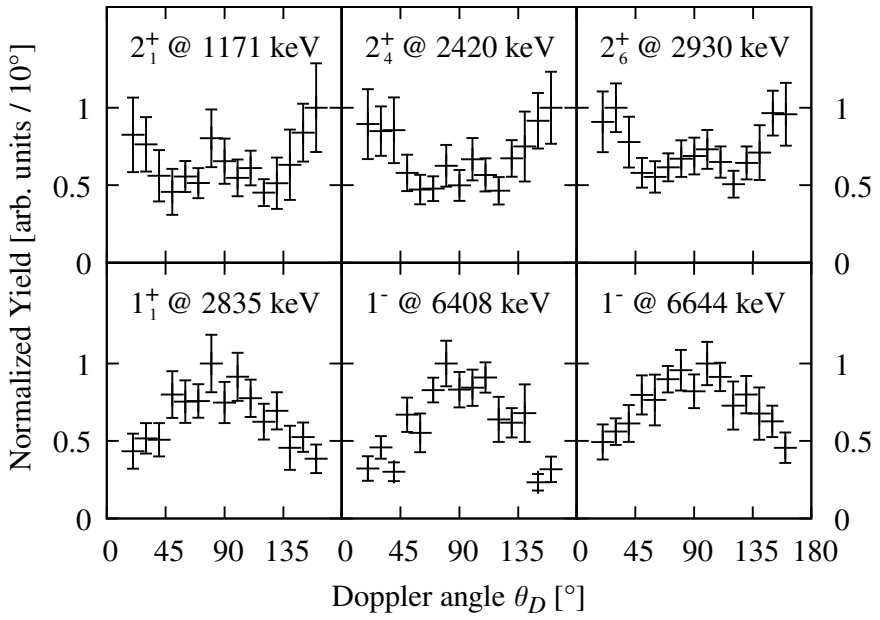

Figure 31: γ-ray angular distributions for discrete ground-state transitions of known states with $J = 1, 2$. The distributions were normalized to the highest yield, respectively, and allow to unambiguously distinguish between $J = 1$ states and $J = 2$ states. The parity of the excited state does not influence the distribution in terms of the Doppler angle. Figure adopted from the supplemental material of Ref. [76].

in Appendix B.4. The characteristic shape for $J = 1, 2$ states may depend highly on the populating reaction. Distributions obtained from, e.g., a $(p, p'\gamma)$ reaction may differ strongly and are currently investigated [99, 100].

Furthermore, distributions in terms of the tilt angle ϕ_t between the reaction plane and the γ-ray emission plane were investigated. However, due to the symmetry of the SONIC@HORUS setup, the available angles cover only a range from 60° to 90° and are, thus, deemed insensitive to any spin or parity dependence. The tilt angles ϕ_t possible with the used SONIC-V1 target chamber are depicted in Appendix B.3.

The γ-ray distributions shown in Fig. 32 were obtained in a continuous manner in 200 keV wide bins for ground-state decays between 5.2 MeV and 8.3 MeV. A dominant $J = 1$ character is observed up to approx. 7.5 MeV, while the distributions are less pronounced towards higher energies. The majority of the discrete transitions have been observed in the (γ, γ') experiment as well and were assumed to be of $E1$ character there. Furthermore, the $M1$ contribution below 8 MeV in ^{120}Sn was found to be negligible in a (p, p') experiment using Coulomb excitation [79] and a recent ^{120}Sn(γ, γ') experiment using a linearly-polarized monochromatic γ beam [80]. Therefore, it can be assumed that all transitions observed up to 7.5 MeV originate from $J^\pi = 1^-$ states.

The less pronounced distributions and the generally decreased spectral quality above 7.5 MeV cannot be explained unambiguously. While the overall level density certainly increases with excitation energy, the behavior may be caused by a change in the underlying structure of the excited states towards higher energies, as was suggested in Ref. [79]. However, it is also possible that the kinetic energy remaining after such high excitation is too low for a sufficient alignment of the recoiling nuclei within the solid angles covered by detectors, which deteriorates the measured angular distributions. A sudden increase in $E2$ strength is, however, unlikely in the ground-state decay gate as no considerable amount of such strength was observed in the monochromatic (γ, γ') experiment [80].

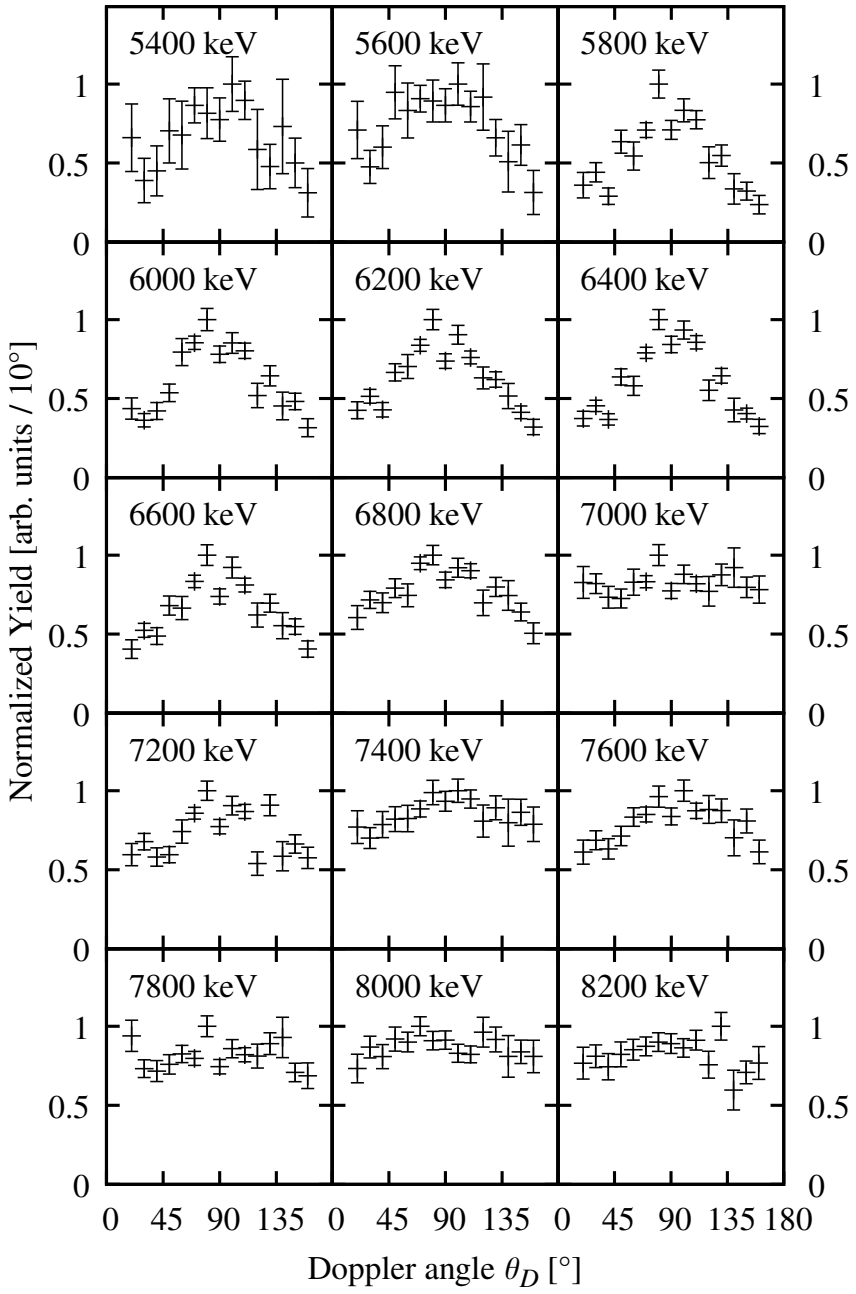

Figure 32: γ-ray angular distributions for ground-state decays of excited states between 5.3 MeV and 8.3 MeV in bins of 200 keV. The distributions were normalized to the highest yield, respectively. The distributions show a dominant $J = 1$ character up to approx. 7.5 MeV. Above 7.5 MeV, a less pronounced distribution is observed. As shown in Refs. [79] and [80], the $M1$ contribution below 8 MeV is negligible and pure $E1$ character of the observed ground-state transitions can be assumed. Figure adopted from the supplemental material of Ref. [76].

3.6 Relative Cross Sections

After the dominant $E1$ character was identified in the previous section, relative yields can be determined for the discrete transitions which represent the excitation cross section $\sigma_{(d,p)}$ folded with the ground-state γ-decay branching ratio b_0. The integrated peak areas were corrected for detection efficiency and normalized to the strongest transition observed in the experiment at 6644 keV. Note that the yield of this transition is approx. three times higher than of the 2_1^+ state. Figure 33 depicts the relative yield of all 92 transitions observed in $(d, p\gamma)$ as well as the energy integrated cross section I_S from (γ, γ') [50]. A list of all transitions observed in the ^{119}Sn$(d, p\gamma)$ experiment and their determined relative yields can be found in Appendix B.5. The sensitivity limit given in the figure was determined with a 30 % uncertainty limit, as it was derived in Ref. [63] and is common in this type of analysis. A detailed discussion and comparison of the relative yields to the (γ, γ') and $(\alpha, \alpha'\gamma)$ data presented earlier is given in Chapter 5.

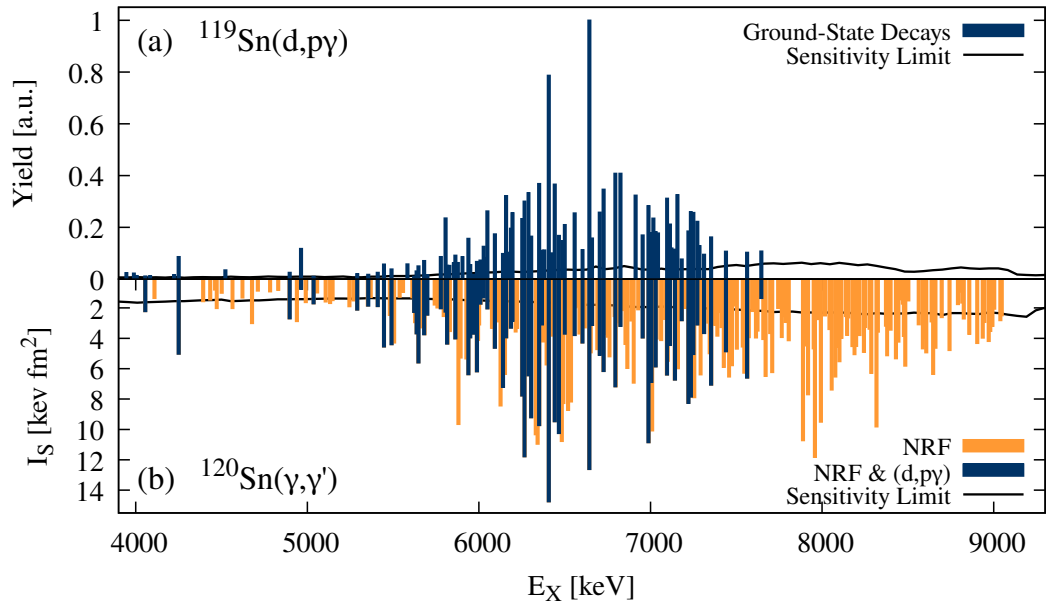

Figure 33: (*a*) Experimental ^{119}Sn$(d, p\gamma)$ yields normalized to the strongest transition at 6644 keV. (*b*) Energy integrated cross sections from NRF taken from Ref. [50]. The sensitivity limit given in both panels marks the 30 % uncertainty limit, as described in [63]. Transitions observed in both experiments are marked in blue in Panel (*b*) as well.

4 Theoretical Predictions of Nuclear Structure and Reaction Cross Sections

The following sections address a selection of theoretical concepts that are commonly used to describe certain nuclear-structure features and observables in the low-energy electric dipole response (LEDR) of even-even nuclei. An overview of general theoretical concepts for nuclear structure can be found in Refs. [101, 102] and in-depth details on the approaches used in LEDR studies are collected in Ref. [103]. The results presented in Chapter 5 were obtained from these concepts and the explicit calculations are courtesy of Nadia Tsoneva, Edoardo G. Lanza, Gregory Potel, and their collaborators. The output of QPM nuclear-structure calculations introduced in Chapter 4.2 is coupled to two different reaction theory approaches in order to extract absolute cross sections for individual QPM states in Chapters 4.3 and 4.4. Both combined approaches are labeled as QPM+Reaction theory in the following.

4.1 General Considerations

Atomic nuclei are mesoscopic quantum systems that are governed by the complex nuclear and Coulomb interactions between nucleons that form them. Ab-initio approaches are able to describe nuclear-structure features up to the Sn region nowadays [104, 105] and very recently reached the description of bulk nuclear properties of ^{208}Pb [106]. However, the model space needed to describe the LEDR in typical medium to heavy mass isotopes still exceeds the available computational capabilities. A formalism that has historically proven to be helpful in approximating the nuclear interaction is the *mean-field* approach, in which the forces imposed on each nucleon are conveyed by an average potential generated by all nucleons inside the system [102]. This concept was developed already in the 1920s to describe the motion of electrons in the central Coulomb field of the nucleus by Hartree and Fock [107, 108] and soon evolved into the *independent particle model* for atomic nuclei. The latter is already capable of describing the rough nuclear ground-state properties, such as binding energies, masses, and a general shell structure [101].

However, to better describe nuclear excitations, additional interactions between nucleons had to be included and were encapsulated in the so-called *residual interaction*, that contains all other, potentially weaker, yet important, interactions. In this approach, the Hamiltonian describing the system is split up into the central mean-field part H_0 and the residual part H_1

$$H = H_0 + H_1 = (T + V_0) + V_1. \tag{4.1}$$

Here, T describes the classical kinetic energy and V_0 is the average mean-field potential. V_1 is the residual interaction, which is still investigated today and can be implemented, e.g., as a Skyrme type zero-range interaction [109] or a finite-range Gogny interaction [110] between individual nucleons.

Following Eq. 4.1, the Schrödinger equation decomposes into

$$H\Psi = H_0\Psi + H_1\Psi = E\Psi. \tag{4.2}$$

A common approach to solve the Schrödinger equation and obtain final wave functions for both the ground state and excited states is to expand Ψ in terms of simpler wave functions φ_i, which form the eigenstates of the mean-field Hamiltonian H_0. In the case of an atomic nucleus, these can be the single-particle states of nucleons in the mean-field potential, i.e., omitting residual interaction. Then, the Schrödinger equation is transformed into a system of coupled equations [101]:

$$\begin{bmatrix} E_0 & V_{12} & V_{13} & \dots & V_{1N} \\ V_{21} & E_1 & V_{V23} & \dots & V_{2N} \\ \vdots & & \ddots & & \vdots \\ V_{N1} & & \dots & & E_N \end{bmatrix} \begin{bmatrix} \varphi_0 \\ \vdots \\ \varphi_N \end{bmatrix} = \begin{bmatrix} E_0 & & & \\ & \vdots & & \\ & & E_N & \end{bmatrix} \begin{bmatrix} \varphi_0 \\ \vdots \\ \varphi_N \end{bmatrix} \tag{4.3}$$

The off-diagonal matrix elements represent the interaction between two nucleons acting within a final state. The final wave functions Ψ^k are obtained within the so-called *Random Phase Approximation* (RPA) by solving a set of RPA equations [102] and diagonalizing the matrix. These RPA wave functions are called *RPA phonons* and contain a superposition of all the simpler single-particle wave functions chosen for the model space with varying contributions. They can be expressed as

$$\Psi^k = \sum_i \alpha_i^k \varphi_i, \tag{4.4}$$

based on the single-particle wave functions φ_i and the contributions α_i^k. These contributions can interfere and add up coherently, i.e., in phase, or in a more complicated manner. For the lowest excited states, e.g., in spherical even-even nuclei, a coherent contribution from many single-particle states is observed and interpreted as a strong *collective* character of the final RPA state. This provides a link to the macroscopic picture of a liquid drop performing a quadrupole vibration, e.g., for a first excited 2^+ state, describing such strong and collective excitations within the microscopic picture of coherent single-particle excitations which form one (RPA) state. The extended Quasiparticle-RPA (QRPA) approach then adds the pairing interaction between two nucleons within

the Hartree-Fock-Boguliubov theory (HFB) [102]. This addition is especially important for nuclei away from closed shells, where the interaction between the available valence nucleons has to be taken into account.

Based on the historic (Q)RPA formalism, two modern approaches are commonly used to describe the strength distribution and underlying structure of the LEDR. The first is the Relativistic-Quasiparticle-Time-Blocking-Approximation (RQTBA). It is built on a relativistic version of the QRPA and is extended by Particle-Vibration-Coupling (PVC), which couples single-particle states to low-lying vibrations, i.e., to collective (Q)RPA phonons [111–113]. By coupling 1p-1h states to these low-lying vibrational states, a higher fragmentation in the energy region of interest (5–10 MeV) is achieved while maintaining the underlying structure of the 1p-1h contributions. RQTBA+PVC calculations have successfully been used to describe the LEDR of several nuclei and especially to reproduce the mixed isospin character found in ^{124}Sn [43, 96]. However, the fragmentation obtained with the RQTBA+PVC model is much lower than experimentally observed (cf. Ref. [113]), causing the strength per state to be about an order of magnitude too large in the model. The second approach, which gives much higher fragmentation while still maintaining the microscopic structure of each state, is presented in the next section.

4.2 Nuclear-Structure Calculations – The *EDF+QPM* Approach

The nuclear-structure calculations presented in Chapter 5 were performed within the *Quasiparticle-Phonon-Model* (QPM), which builds on top of the QRPA approach. It uses modern Energy-Density-Functional (EDF) theory to determine the mean field in a self-consistent way and it reproduces nuclear ground-state properties and single-particle energies from microscopic interactions [114]. Figure 34 tries to visualize the two-stage process that constructs final QPM states from coupled QRPA phonons, which are in turn constructed from 1p-1h excitations in the single-particle picture of the EDF+QRPA formalism. Individual QRPA phonons are created by the operator

$$Q^+_{\lambda\mu i} = \frac{1}{2}\sum_{jj'} \Big(\psi^{\lambda i}_{jj'} A^+_{\lambda\mu}(jj') - \varphi^{\lambda i}_{jj'} \widetilde{A}_{\lambda\mu}(jj') \Big), \tag{4.5}$$

where the set of quantum numbers $j \equiv (nlmj\tau)$ label single-nucleon states, and $A^+_{\lambda\mu}$ and $\tilde{A}_{\lambda\mu}$ are the time-forward and time-backward two-quasiparticle operators, creating or annihilating two quasiparticles coupled to a total angular momentum λ with projection μ [115]. The time-forward and time-backward amplitudes $\psi_{jj'}$ and $\varphi_{jj'}$ are obtained together with the excitation energy by solving a set of QRPA equations [115]. Each

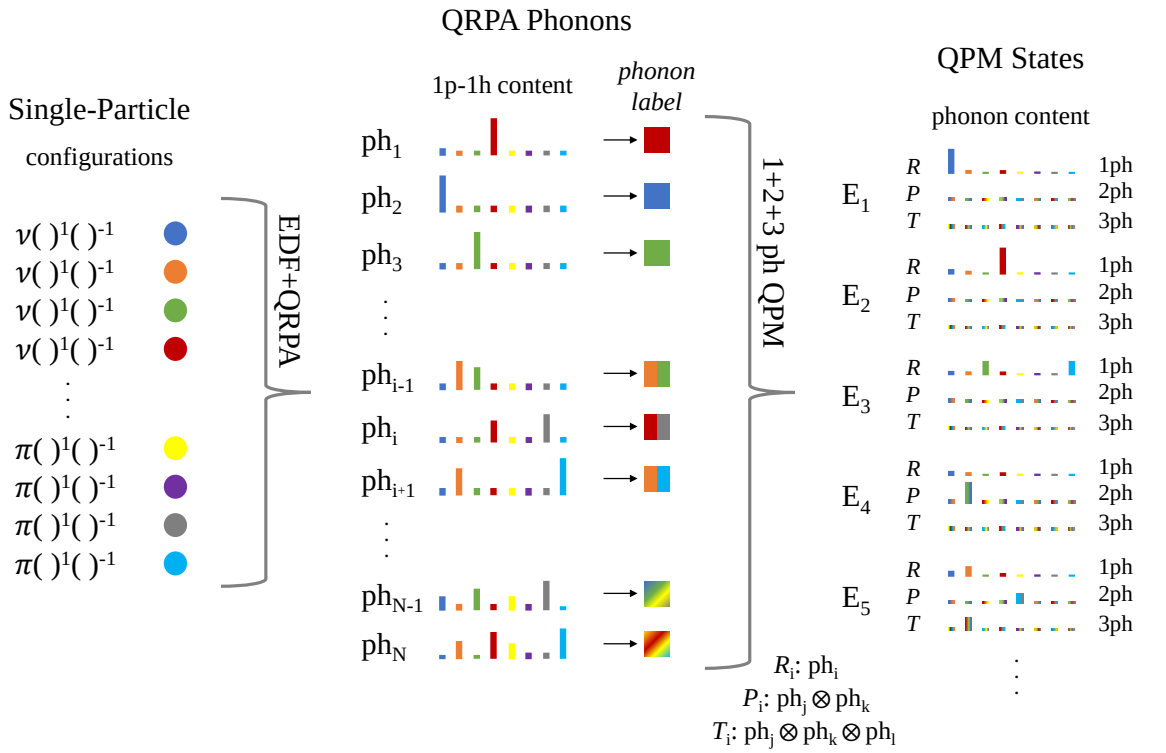

Figure 34: Schematic construction of QPM states from QRPA phonons and 1p-1h configurations. Starting on the left, a model space of pure 1p-1h configurations is chosen, here identified by colored circles. The EDF+QRPA approach constructs QRPA phonons from these and their characteristic 1p-1h content is indicated by the colored bars in the center. At this stage, certain phonons are found to be rather pure in configuration and they are labeled with the corresponding 1p-1h configuration as indicated by the colored squares. The 1+2+3 phonon QPM couples one, two, and three of these phonons to obtain final states. Each QPM state on the right is characterized by the sets of R, P, and T values representing the contribution from each possible one, two, or three phonon coupling. Note that an exact color representation is only possible for the simpler cases and that R, P, and T values can be negative.

phonon represents a strong single-particle excitation if it is dominantly generated by a specific 1p-1h configuration. Conversely, a single phonon represents a collective excitation, if several 1p-1h configurations add up coherently to generate the phonon. Within the scope of the calculations presented in Chapter 5, several QRPA states, or phonons, were assigned to their main 1p-1h constituent in order to identify the important 1p-1h configuration in the final QPM states. However, the overall EDF+QPM approach allows much more complex configurations.

From these QRPA phonons, the QPM model space is then built by the coupling of phonons and allowing one-, two-, and three-phonon (1ph, 2ph, 3ph) contributions to the individual QPM states. The final wave function of QPM state ν is then expressed

via

$$\begin{aligned}\Psi_\nu = \Bigg\{ & \sum_i R_i(\nu)\; Q^+_{1Mi} \\ & + \sum_{\substack{\lambda_1 i_1 \\ \lambda_2 i_2}} P^{\lambda_q i_1}_{\lambda_2 i_2}(\nu)\; \Big[Q^+_{\lambda_1\mu_1 i_1} \times Q^+_{\lambda_2\mu_2 i_2} \Big]_{1M} \\ & + \sum_{\substack{\lambda_1 i_1 \lambda_2 i_2 \\ \lambda_3 i_3 I}} T^{\lambda_1 i_1 \lambda_2 i_2 I}_{\lambda_3 i_3}(\nu)\; \Big[\Big[Q^+_{\lambda_1\mu_1 i_1} \times Q^+_{\lambda_2\mu_2 i_2} \Big]_{IK} \times Q^+_{\lambda_3\mu_3 i_3} \Big]_{1M} \Bigg\} \Psi_0,\end{aligned} \tag{4.6}$$

where R, P, and T are the amplitudes related to specific one-, two-, and three-phonon couplings, respectively, and Ψ_0 is the ground-state wave function.

For the calculations presented in Chapter 5, the model space for two- and three-phonon couplings includes QRPA phonons of $J^\pi = 1^\pm - 6^\pm$ up to $\mathrm{E_X} = 9\,\mathrm{MeV}$. The one-phonon space was built from single QRPA phonons up to $\mathrm{E_X} = 35\,\mathrm{MeV}$. Overall, several hundred QRPA phonons were included in the model space. All possible 1+2+3 phonon couplings resulted in approx. 50 million combinations and matrix elements to be solved. A more detailed explanation of the calculations can be found in Refs. [76, 114]. The collectivity of an excited state within the QPM is represented by the coherent coupling of many QRPA phonons. Conversely, a state is interpreted to have a strong single-particle character if a final QPM state has a dominant contribution from a single QRPA phonon, which itself is dominantly generated by one single-particle excitation on the QRPA level. As will be shown in Chapter 5, this is the case for several states in the LEDR of ^{120}Sn. The important features of the QPM are that the microscopic character of underlying single-particle configurations is transported through to the final states while a realistic level of fragmentation is achieved by coupling of phonons. In case of the QPM calculations presented in this work, a total of 475 $J^\pi = 1^-$ states were obtained below $S_n = 9.1\,\mathrm{MeV}$.

Since the QPM provides detailed access to the wave function of each excited state, both the reduced transition strength $\mathrm{B}(E1)\uparrow$ and the γ-decay behavior can be calculated based on the overlap between the wave functions considered [116, 117]. This theoretical access to experimental observables has been used to study the decay pattern of neutron-skin modes in the last years [85, 118]. For a stringent comparison to results obtained in this work, the theoretical $\mathrm{B}(E1)\uparrow$ values are converted to energy-integrated cross sections I_S for a ground-state transition observed in (γ,γ') using bremsstrahlung, as I_S is the native observable of such experiments. The following relations [40] apply to electric

dipole transitions to the 0^+ ground state:

$$\mathrm{B}(E1)\uparrow\ [e^2\mathrm{fm}^2] = 9.554 \cdot 10^{-4} \cdot g \cdot \frac{\Gamma_0\ [\mathrm{meV}]}{\mathrm{E}_\gamma^3\ [\mathrm{MeV}]} \tag{4.7}$$

$$I_S = \pi^2 \cdot \left(\frac{\hbar c}{\mathrm{E_X}}\right)^2 \cdot g \cdot \frac{\Gamma_0^2}{\Gamma} \tag{4.8}$$

with the spin factor $g = \frac{2J_i+1}{2J_0+1} = 3$. Using $1\,e^2\mathrm{fm}^2 = 1.44\,\mathrm{MeV\,fm}^3$ and $10\,\mathrm{eV\,b} = 1\,\mathrm{keV\,fm}^2$, Equations 4.7 and 4.8 can be transformed to

$$I_S\ [\mathrm{keVfm}^2] = 4.023 \cdot 10^{-6} \cdot \frac{\Gamma_0}{\Gamma} \cdot \frac{\mathrm{E}_\gamma\ [\mathrm{MeV}]}{\mathrm{B}(E1)\uparrow\ [e^2\mathrm{fm}^2]} \tag{4.9}$$

with the partial decay width to the ground state Γ_0 and the total width $\Gamma = \sum_i \Gamma_i$. The Γ_0/Γ ratio is typically expressed in terms of the ground-state decay branching-ratio $b_0 = \Gamma_0/\Gamma$. For the conversion of QPM $\mathrm{B}(E1)\uparrow$ values to I_S valus, it is assumed that the γ-ray energy is equal to the excitation energy $\mathrm{E_X}$.

Besides the observables mentioned above, the QPM gives transition densities (TRDs) for each state, which show the contribution from protons ($\rho_p(r)$) and neutrons ($\rho_n(r)$) to the density distribution as function of radius. Explicit TRDs for ^{120}Sn are presented in Chapter 5. They are used to interpret the nature of excitations, i.e., how nucleon motion is shared among protons and neutrons and whether it takes place on the surface of the nucleus or deeper inside of it. Lastly, the proton and neutron TRDs $\rho_p(r)$ and $\rho_n(r)$ are needed to calculate (α, α') excitation cross sections within the approach presented in the next section.

4.3 Theoretical Prediction of (α, α') Cross Sections

For a consistent comparison between experiment and theory, the true experimental observable in (α, α'), i.e., absolute differential cross sections $\frac{d\sigma}{d\Omega_\alpha}$ integrated over the spectrometer solid angle Ω_α and folded with the ground-state decay branching-ratio b_0, were extracted from the QPM calculations. Therefore, the semi-classical approach described in Refs. [43, 119] was employed, which solves *Coupled-Channel* equations [120] describing the elastic and all inelastic reaction channels simultaneously. The procedure allows to differentiate between isoscalar and isovector contributions to each state based on the proton and neutron TRDs [96]. If Coulomb excitation is neglected, the α particles with N=Z are assumed to be sensitive exclusively to the isoscalar part of an excitation, i.e., to only the part where proton and neutron TRDs are in phase. At the chosen beam energy of $\mathrm{E}_\alpha = 130\,\mathrm{MeV}$ and forward scattering, α particles interact with the nuclear surface

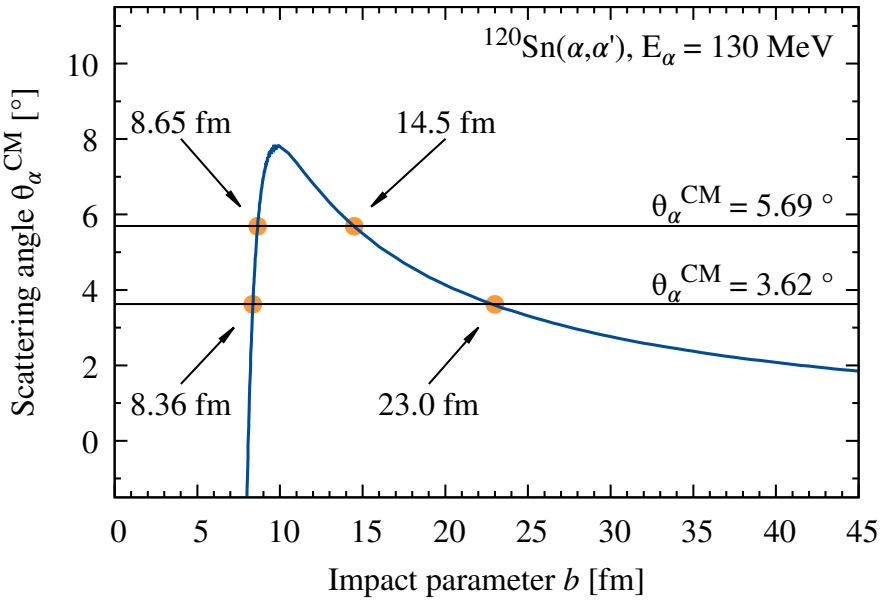

Figure 35: Deflection function for α particles at $E_\alpha = 130\,\text{MeV}$ on ^{120}Sn. The boundary center-of-mass α scattering angles Θ_α^{CM} from the experiment are marked by dashed lines, while the corresponding impact parameters b are labeled at the intersections with the deflection function.

and the experimentally available scattering angles in the center-of-mass frame Θ_α^{CM} are translated to classical impact parameters b via the deflection function shown in Fig. 35. The latter is used in the reaction theory to account for different scattering angles. Both Coulomb and nuclear interaction are taken into account and it is possible to determine cross sections for each interaction separately, neglecting interference between them, or in a combined manner for a physical result. The overall procedure depends heavily on the TRDs used, especially at the nuclear surface, but has been proven to work on a qualitative [42] and quantitative level for the comparable case of $^{124}\text{Sn}(\alpha, \alpha')$ [43] and $^{124}\text{Sn}(^{17}\text{O}, ^{17}\text{O}')$ [45]. Taking the QPM as input, the more complex 2ph+3ph configurations are expected to have only second order effects on the direct (one-step) excitation in (α, α') and are, thus, negligible [121]. Instead, TRDs are generated based on only the one-phonon contributions to each QPM state.

4.4 Theoretical Prediction of (d, p) Cross Sections

In contrast to the procedure used for (α, α'), which relies on a somewhat macroscopic input in form of TRDs, the reaction theory employed for $^{119}\text{Sn}(d, p)$ uses microscopic information about the contribution of specific QRPA phonons to final QPM states, i.e., the QPM R values. The theory has been developed in order to use the (d, p) reaction as a replacement, or *surrogate*, for experimentally inaccessible (n, γ) reactions [30, 31].

Recently, it was also used to describe the excitation of 1^- states in ^{207}Pb(d,p), studying the structure of these states in doubly magic ^{208}Pb [122]. Within this thesis, the predicted excitation was for the first time combined with the γ-decay behavior determined from the QPM in order to obtain identical observables from experiment and theory [76].

The ground state of the target nucleus ^{119}Sn is assumed to be a pure $3s_{1/2}$ neutron-hole state relative to the ^{120}Sn core, as is supported by experimental findings [123, 124]. The (d,p) reaction is assumed to excite nuclear states only via one-step processes, i.e., two- and three-phonon states cannot be excited, and the proton is treated as a spectator only. Since ground-state correlations are predicted to be negligible in ^{120}Sn [125], the time-backward amplitudes $\varphi_{jj'}$ from Eq. 4.5 vanish. Within these approximations, a $J^\pi = 1^-$ state can only be populated by the ^{119}Sn$(d,p)^{120}$Sn reaction if it contains a neutron in the $3p_{3/2}$ or $3p_{1/2}$ orbital, i.e., if it has a $(3s_{1/2})^{-1}(3p_{3/2})^{+1}$ or $(3s_{1/2})^{-1}(3p_{1/2})^{+1}$ neutron configuration. Hence, only one-phonon contributions from these two configurations, $R_{3p_{3/2}}$ and $R_{3p_{1/2}}$, are relevant. The final differential cross section for a state ν is then given by

$$\begin{aligned}\frac{d\sigma_\nu}{d\Omega}(\theta) = \quad \frac{\mu_i\mu_f}{(2\pi\hbar^2)^2}\frac{k_f}{k_i} \times \Big| \; & u_{3p_{1/2}} R_{3p_{1/2}}(\nu)\, \psi^{3p_{1/2}}_{\frac{1}{2}\frac{1}{2}}\, \mathcal{T}_{p_{1/2}}(\theta) \; + \\ & u_{3p_{3/2}} R_{3p_{3/2}}(\nu)\, \psi^{3p_{3/2}}_{\frac{1}{2}\frac{3}{2}}\, \mathcal{T}_{p_{3/2}}(\theta) \; \Big|^2 \end{aligned} \tag{4.10}$$

By calculating cross sections for the experimental detector angles and combining them with the γ-decay branching from the QPM, the theoretical yield is obtained for each state ν in units of mb/sr via

$$Y_\nu = \frac{d\sigma_\nu}{d\Omega}(\theta_{exp}) \cdot \frac{\Gamma_0}{\Gamma} \tag{4.11}$$

By employing the two combined QPM+Reaction approaches introduced above, the true observables of each experiment were obtained from theory within this work, enabling the one-to-one comparison of laboratory and theory shown in the next chapter.

5 Nuclear-Structure Insights from Combined Experimental and Theoretical Results

Deep insight into nuclear-structure phenomena can be obtained from the combined knowledge about the response to different probes in a *multi-messenger* approach [46], referencing the coincident observation of astrophysical events through different instruments [126]. With the two new experimental data sets obtained in this thesis, the detailed QPM+Reaction calculations performed for both experiments, the recent high-sensitivity (γ, γ') measurement [50], and a (p, p') measurement using Coulomb-excitation [127], a plethora of information are available on the dipole response of ^{120}Sn. The following chapter tries to break down the information newly obtained in this thesis and compares it to previously available knowledge.

First, the QPM calculations are compared to two electromagnetic-probe experiments in Section 5.1, benchmarking the overall reproduction of summed $E1$ strength and fragmentation. Of special interest is the discrepancy between the $\mathrm{B}(E1)\uparrow$ strength determined from (p, p') and the bremsstrahlung experiment. Next, detailed information on the single-particle character of the LEDR in ^{120}Sn will be discussed in Section 5.2 by comparing the experimental ^{119}Sn$(d, p\gamma)$ results to the QPM+Reaction calculations. The microscopic information available for each QPM state are analyzed and the evolution of the LEDR between 4 MeV and $S_n = 9.1$ MeV is investigated. Results obtained from the $(\alpha, \alpha'\gamma)$ experiment are put in relation to the other data sets in Section 5.3. The sensitivity to isoscalar surface modes pronounces the macroscopic features of excited states, allowing to investigate the LEDR from two contrasting points of view, i.e., within the microscopic or single-particle picture probed in $(d, p\gamma)$, and the macroscopic response to surface probes observed in α scattering. Lastly, general implications on the LEDR in the Sn region are discussed in Section 5.4, together with future possibilities to deepen the understanding of especially the $(d, p\gamma)$ probe.

5.1 Benchmarking the QPM – Electromagnetic Response

A common measure for the accuracy of LEDR calculations is the summed $\mathrm{B}(E1)$ strength up to S_n. Since usually the $\mathrm{B}(E1)\uparrow$ values representing the excitation are determined from theory, it is advisable to compare it to experimental data that also probe the excitation directly, independent of the γ-decay behavior. Such an experiment was performed using high-energy proton scattering at $\mathrm{E}_p = 295$ MeV and forward angles at RCNP, Osaka, where states are excited via Coulomb excitation (CoulEx) [127]. After a multipole decomposition analysis (MDA), the $E1$ strength is extracted in a continuous

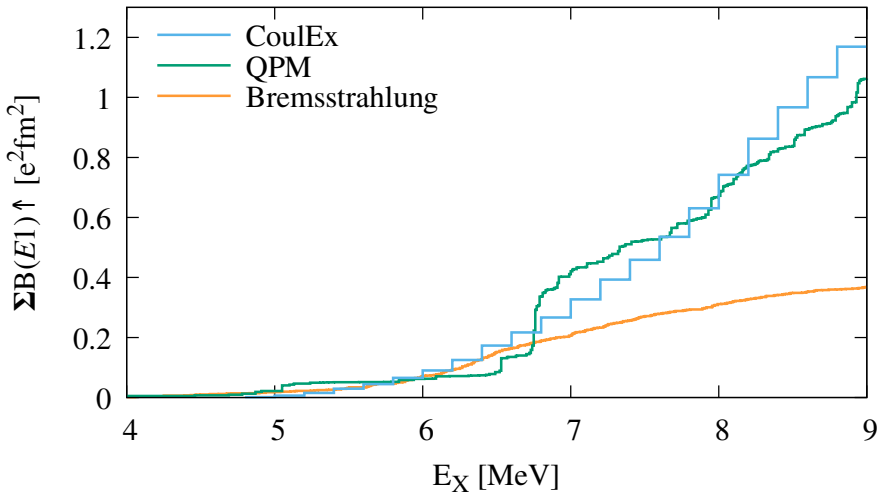

Figure 36: Running sums of the $\mathrm{B}(E1)\uparrow$ strength from (γ,γ') using bremsstrahlung [50], (p,p') Coulomb excitation [127], and the QPM calculations. The (γ,γ') data are missing strength at higher energies due to experimental reasons. The QPM shows good agreement to the CoulEx data.

manner down to about $\mathrm{E_X} = 5\,\mathrm{MeV}$. During the recent campaign on the Sn isotopic chain [79], the data from Ref. [127] were confirmed. However, a certain model dependence due to the MDA procedure remains. When extracting $\mathrm{B}(E1)\uparrow$ values from bremsstrahlung (γ,γ') experiments, a certain amount of strength can be missing due to weak transitions hiding in the spectrum, or misplaced due to the unclear identification of ground state transitions. Thus, the summed strength below S_n differs strongly between (γ,γ') and (p,p'). Figure 36 shows the running sums of the $E1$ strength determined continuously from (p,p') and from the discrete transitions observed in (γ,γ'). While the (p,p') data strongly increase in strength towards higher energies, the (γ,γ') data exhibit a comparably slow increase above 8 MeV. It was suggested that this behavior is due to increasingly complex configurations within excited states at higher energies [79], opening a variety of weaker decay paths for each state and, thus, significantly reducing the ground-state decay strength.

The summed QPM $\mathrm{B}(E1)\uparrow$ strength shown in Fig. 36 is in very good agreement with the (p,p') data. The total strengths below S_n are reported to be $\Sigma\mathrm{B}(E1)\uparrow = 0.369(49)\,\mathrm{e^2fm^2}$ for (γ,γ')[50], $\Sigma\mathrm{B}(E1)\uparrow = 1.169(12)\,\mathrm{e^2fm^2}$ for (p,p')[127], and $\Sigma\mathrm{B}(E1)\uparrow = 1.066\,\mathrm{e^2fm^2}$ from the QPM. As reported in Ref. [127], the alternative RQTBA approach gives summed strengths several times higher than the experiment. A very recent analysis of ^{120}Sn(γ,γ') data using monoenergetic photon beams also confirms the (p,p') data [80]. This rather precise reproduction of both the summed strength and the trend up to S_n supports the QPM's predictive power of the overall LEDR strength, irrespective of the underlying

structures. Thus, the next sections will investigate more deeply the nuclear-structure information obtained from the QPM.

5.2 Single-Particle Character of the LEDR

As described in Chapter 4.4, the ^{119}Sn$(d, p\gamma)$ reaction is assumed to be of direct type and states are excited in a one-step process. This assumption could have been supported by the observation of pronounced proton angular distributions and comparison to, e.g., DWBA calculations assuming pure configurations. However, only the $p-\gamma$ coincidence data are available with proton detection under backward angles. In an effort to underline the direct character of the reaction, the experimental yield of low-lying states is compared to (d, p) spectroscopic factors obtained from transfer experiments at higher energies and forward angles [123]. These values are extracted from (d, p) angular distributions and correlate to the single-particle content of a given excitation and are close to 1 when states have a strong contribution from specific 1p-1h configurations. If the $(d, p\gamma)$ reaction measured with SONIC@HORUS was of direct type, instead of a compound-like reaction, the overall yield should be roughly proportional to the (d, p) spectroscopic factors.

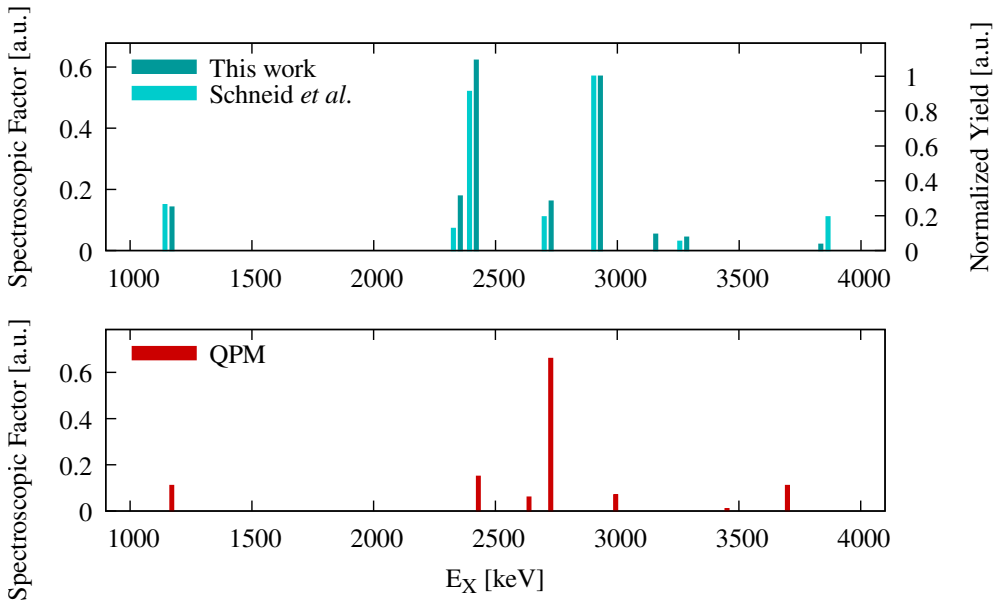

Figure 37: *Top*: Spectroscopic factors of known 2^+ states in ^{120}Sn from experiment [123] and the yield in ^{119}Sn$(d, p\gamma)$. The $(d, p\gamma)$ data were corrected for γ-decay branching and normalized to the state at 2930 keV. Good agreement between the two experiments at different energies and detection angles is found, supporting the direct reaction character of the SONIC@HORUS experiment. *Bottom*: Spectroscopic factors of 2^+ states obtained from QPM calculations for comparison.

Figure 37 presents these spectroscopic factors for several known $J^\pi = 2^+$ states, together with the $(d, p\gamma)$ yield corrected for γ-decay branching and normalized to the state with the highest spectroscopic factor at $E_X = 2930\,\text{keV}$. The data obtained in this thesis follow the same trend as the spectrometer data, supporting the assumption of a direct reaction. For completeness, Fig. 37 also shows spectroscopic factors of the first six QPM $J^\pi = 2^+$ states. A one-to-one comparison to states observed in the experiment based on the QPM energy ordering is difficult, except for the first excited state. However, the QPM predicts that the majority of 2^+ states have small spectroscopic factors, while one state around 2.5 MeV has a high value. Both features are in agreement with the experimental findings. Especially the small factor of the first 2^+ state is reproduced, owing to the collective nature of the first quadrupole vibration states commonly observed in spherical medium to heavy mass nuclei.

Fragmentation of QRPA Phonons

One of the features of the QPM is that microscopic information on the generating single-particle configurations is transported through to the final QPM states. As described in Section 4.2, hundreds of QPM states are generated by coupling QRPA phonons to one-,

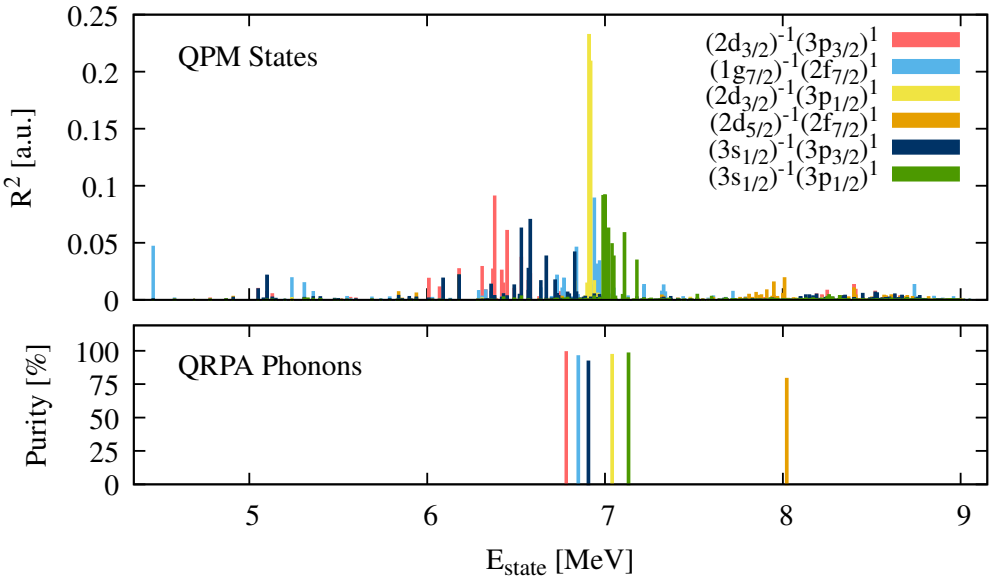

Figure 38: *Top*: Distribution of the squared QPM R values representing contributions from the six dominant QRPA one-phonon states. *Bottom*: QRPA excitation energy of each phonon and the content of the configuration that was used as a tag. The configurations / phonons shown here give significant contribution to final QPM states. Other, more complex or collective 1ph/2ph/3ph states are omitted here, but were included in the overall calculation of the 475 QPM states.

two-, and three-phonon combinations, which in turn all contribute to a given QPM state. Several of the QRPA (one-) phonon states are dominantly generated by specific 1p-1h configurations, allowing to assign each phonon to its main *ingredient*. This separates them from phonons that are generated by more than one or more complex configurations.

From all assigned 1p-1h phonons, only the six found in Fig. 38 give a significant contribution to the final QPM wave functions. The figure, thus, visualizes the prediction of a *single-particle* character of QPM 1^- states and the concentration around 6–7 MeV. This is an interesting finding concerning the open question of the degree of collectivity in the LEDR [19, 122, 128–130]. The lower panel of Fig. 38 shows the energies of the pure QRPA phonons and the corresponding 1p-1h content, or *purity*. The QPM strongly fragments the strength from each phonon, for the case of $(1g_{7/2})^{-1}(2f_{7/2})^1$ (light blue in Fig. 38) even over several MeV. Note that less pure one-phonon states as well as two- and three-phonon states contribute significantly to the QPM, but are not shown here for clarity.

One-Phonon Contribution and γ-Decay Branching

The two configurations accessible in ^{119}Sn$(d, p\gamma)$ and the interplay between the one-phonon (1ph) and two-/three-phonon (2ph+3ph) contributions is investigated in Fig. 39. Panel (*a*) presents the sum of all one-phonon R^2 values and the contribution from just the $\nu(3p_{3/2})^1$ and $\nu(3p_{1/2})^1$ phonons. Here already, the excitation in ^{119}Sn$(d, p\gamma)$ can be predicted to concentrate between 6 and 7 MeV. Panel (*b*) shows the relative contribution from 1ph and 2ph+3ph states to the final QPM states. The relative value is obtained for each state via

$$\begin{aligned} C_{rel}^{1ph} &= \sum R^2 \;\; / \;\; \sum (R^2 + P^2 + T^2) \\ C_{rel}^{2ph+3ph} &= \sum (P^2 + T^2) \;\; / \;\; \sum (R^2 + P^2 + T^2). \end{aligned} \tag{5.1}$$

It becomes clear from Panel (*b*) in Fig. 39 that 1ph configurations dominate the picture below 7 MeV, while 2ph+3ph configurations gain importance towards higher energies. As expected from these more complex configurations, the γ-decay branching to the ground state b_0 decreases towards higher energies (cf. Fig. 39 Panel (*c*)). Both of these theoretical results fit well to the lack of strength observed in bremsstrahlung experiments and the change in structure towards higher energies that was suggested from the comparison of (p, p') and (γ, γ') [79].

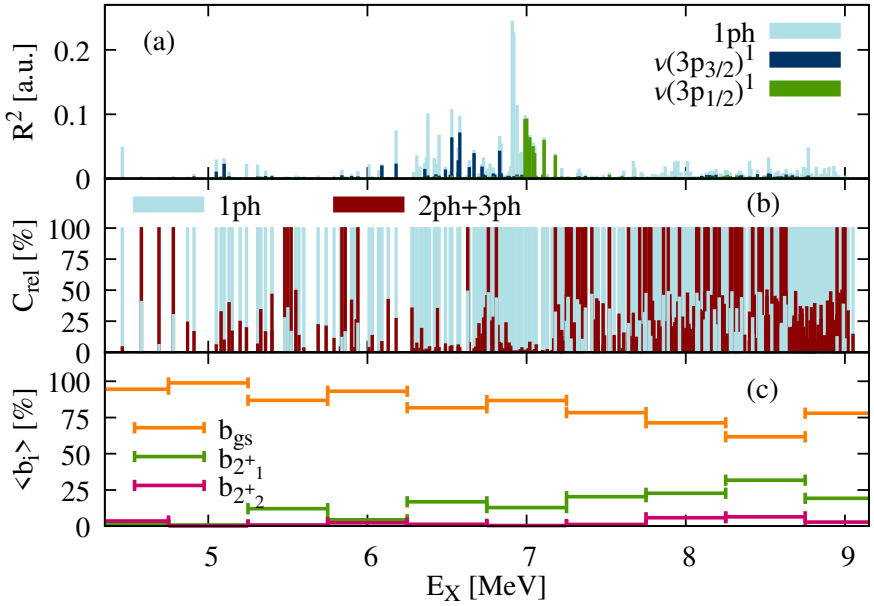

Figure 39: (*a*) Summed squared one-phonon R amplitudes for each QPM state, representing the contribution of a given configuration to the final wave function. Individual contributions of neutron 1p-1h configurations accessible in ^{119}Sn(d,p) are shown in *dark blue* and *green*, respectively. (*b*) Relative *1ph* and *2ph+3ph* contributions to the QPM wave function, as given in Eq. 5.1. (*c*) QPM γ-decay branching to the ground state and to the two lowest-lying excited 2^+ states in ^{120}Sn, averaged over all states in a window of 500 keV. Reprinted figure with permission from M. Weinert *et al.*, Phys. Rev. Lett. **127**, 242501 (2021) [76]. Copyright (2021) by the American Physical Society.

Excitation of $J^\pi = 1^-$ States in ^{119}Sn$(d,p\gamma)$

The experimental results from ^{119}Sn$(d,p\gamma)$ obtained in this thesis and from ^{120}Sn(γ,γ')[50] are presented in Panels (*a*) and (*b*) of Fig. 40 together with the cross sections predicted by the QPM and QPM+Reaction calculations in Panels (*c*) and (*d*). The $(d,p\gamma)$ data were obtained by gating on ground-state γ-ray transitions and identifying excited $J=1$ states via γ-ray angular distributions (see Chapter 3). The strength observed in (γ,γ') is also sensitive to the combination of excitation cross section and the ground-state γ decay. The sensitivity limits of both experiments are given as well. Theoretical values were calculated via the procedures presented in Chapter 4.2 and 4.4. Since no absolute cross sections could be determined from the SONIC@HORUS data, the observed and calculated $(d,p\gamma)$ yields were normalized to the strongest transition in each panel. See Fig. 44 for absolute theoretical values. Since the QPM gives access to both $\mathrm{B}(E1)\uparrow$ values and ground-state decay branchings b_0, the theoretical values for (γ,γ') could be converted to the same observable seen in the experiment, which is the energy-integrated cross section I_S (see Eq. 4.8 in Chapter 4.2). Thanks to the observation of γ-ray angular distributions in both experiments and a negligible $M1$ contribution in ^{120}Sn below S_n

[79, 80], all values shown in Fig. 40 relate to $J^\pi = 1^-$ states. A consistent comparison of theory and experiment is, therefore, possible.

The strength observed in (γ, γ') is highly fragmented between 4 and 9 MeV, with increasing level density towards higher energies. In striking contrast to this, the $(d, p\gamma)$ reaction presents a different picture with a concentration of strength between 5.5 and 7.5 MeV and very weak excitation above 7.5 MeV. This lack of strength towards higher energies cannot be attributed to unobserved ground-state transitions, as these would also affect the (γ, γ') data. The data instead show that only a specific subset of states are dominantly populated in ^{119}Sn$(d, p\gamma)$.

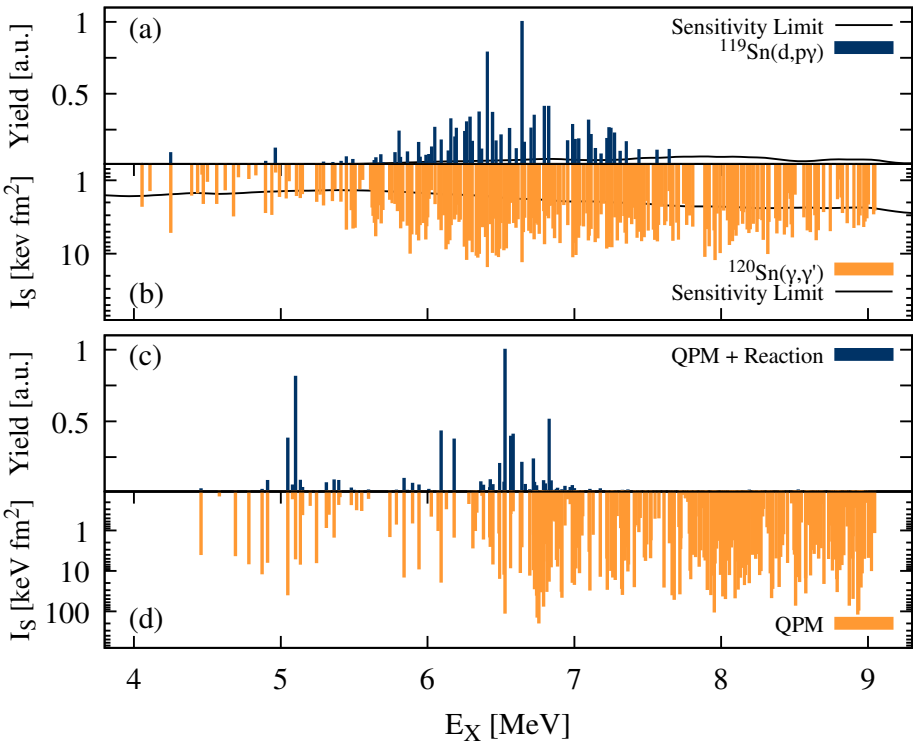

Figure 40: (*a*) relative γ-ray yields from ^{119}Sn$(d, p\gamma)$ and (*b*) energy integrated cross sections I_S for ^{120}Sn(γ, γ') adopted from Ref. [50]. All transitions shown in Panel (*a*) were also observed in the NRF experiment. Sensitivity limits are based on a maximum error on the peak area of 30%. (*c*) relative ^{119}Sn$(d, p\gamma)$ yields from the QPM+Reaction formalism and (*d*) predicted energy integrated cross sections, both taking into account γ-decay branching predicted by the QPM. Experimental and theoretical $(d, p\gamma)$ yields were normalized to the strongest transition, respectively. Reprinted figure with permission from M. Weinert *et al.*, Phys. Rev. Lett. **127**, 242501 (2021) [76]. Copyright (2021) by the American Physical Society.

The QPM reproduces the fragmentation of $E1$ strength between 4 and 9 MeV well (cf. Panel (*d*) of Fig. 40). Due to the limited model space, the experimental level of fragmentation is still out of reach and the strength per state is, thus, about a factor 10

higher than experimentally found. However, as discussed in Chapter 5.1, the summed $\mathrm{B}(E1)\uparrow$ strength below S_n is reproduced within 10 % of the CoulEx data.

Most importantly, the $(d, p\gamma)$ strength obtained from the QPM+Reaction calculations is concentrated between 5 and 7 MeV, resulting in a resonance-like accumulation of 1^- states around a centroid energy of 6.32 MeV, where also the experimental centroid is located (6.49 MeV). This finding shows not only that the QPM reproduces the selective excitation of 1p-1h configurations in (d, p), but also the correct placement of the relevant single-particle energies on the EDF and QRPA level.

In further support of the QPM predictions is the quantitative reproduction of energy-integrated (γ, γ') cross sections for the set of states that are observed both in (γ, γ') and $(d, p\gamma)$. The summed experimental value is $\sum I_S = 337(21)$ keV fm^2, with the smallest relative yield observed in $(d, p\gamma)$ in the order of 1 %. Applying similar sensitivity limits of 1 % and 0.5 % to the QPM+Reaction results, summed values for the (γ, γ') cross section of $\sum_{>1\%} I_S^{QPM} = 243$ keV fm^2 and $\sum_{>0.5\%} I_S^{QPM} = 360$ keV fm^2 are obtained, which are in good agreement to the experimental value.

It needs to be noted that, although visually similar to the comparison of $(\alpha, \alpha'\gamma)$ and (γ, γ') data previously done for ^{124}Sn [41], the different response in $^{119}\mathrm{Sn}(d, p\gamma)$ and $^{120}\mathrm{Sn}(\gamma, \gamma')$ observed for the first time in this thesis is caused by a very different nuclear-structure phenomenon. While in $^{124}\mathrm{Sn}(\alpha, \alpha'\gamma)$ a splitting based on the isospin and surface-mode character of excited states was found [42–44], the results presented here show that very specific 1p-1h configurations dominantly generate the very low-lying parts of the LEDR of ^{120}Sn. The $^{119}\mathrm{Sn}(d, p)$ reaction selects only the two configurations that are accessible from the ground state of ^{119}Sn, i.e., the $(3s_{1/2})^{-1}(3p_{3/2})^{+1}$ and $(3s_{1/2})^{-1}(3p_{1/2})^{+1}$ neutron configurations. Furthermore, the QPM predicts a strong contribution from several other 1p-1h configurations in the low-energy part of the LEDR in ^{120}Sn. A possible connection between the two distinct features discussed above is investigated in the following.

Transition Densitites – Connecting the Single-Particle and Macroscopic Picture

Within the QPM formalism, the six relevant (1p-1h) QRPA phonons are additionally interpreted to be related to a neutron-skin oscillation and are, thus, labeled as *PDR-like* states. This interpretation is based on the pure neutron character and the rough energy below S_n [131]. The label PDR was chosen to contrast the neutron-skin oscillation character with the isovector GDR character assumed to be present in the higher-energy part of the LEDR [19]. However, the neutron-skin character is also reflected in the transition densities for these QRPA phonons as can be seen in the left panel of Fig. 41. Except

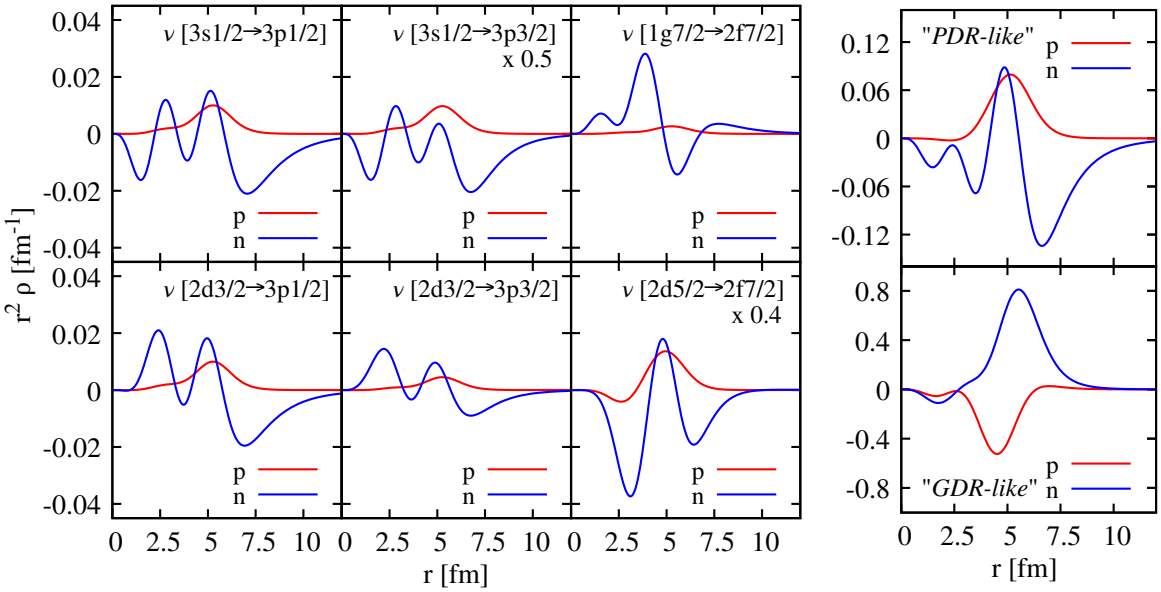

Figure 41: Transition densities for the six relevant 1p-1h QRPA phonons also shown in Fig. 38 (*left*) and average TRDs (*right*). *PDR-like* indicates the average over all QRPA phonons that were related to the PDR based on their pure neutron character and energy below S_n. See text for further explanation. *GDR-like* indicates the average of all QRPA phonons between 9 MeV and 35 MeV. Note that the average TRDs do not represent physical states and are only for visualization.

for the $(1g_{7/2})^{-1}(2f_{7/2})^{1}$ case, all TRDs represent an in-phase oscillation of protons and neutrons inside the nucleus, i.e., at smaller radii, and only a neutron contribution extending to the nuclear surface. This interpretation has previously been used to identify a neutron-skin character in theoretical wave functions [42, 63]. It is, therefore, possible to relate the single-particle character of the relevant QRPA phonons to the macroscopic picture of a neutron-skin oscillation causing (parts of) the electric dipole strength below S_n.

The right panel of Fig. 41 shows an average TRD for *PDR-like* states, exhibiting even more pronounced the in-phase, or isoscalar, behavior inside the nucleus and strong neutron contributions extending further out. In contrast, the *GDR-like* TRD is averaged over all QRPA phonons between 9 and 35 MeV and shows a strong out-of-phase oscillation or isovector behavior of protons and neutrons. Both averaged TRDs do not represent physical states, but are for visualization only. However, it should be noted that the isovector GDR character above S_n is reproduced by the QPM and, especially, that the six relevant QRPA phonons, i.e., the dominant 1p-1h configurations, do in fact resemble a neutron-skin oscillation.

From the analysis of the complex QPM results and the comparison to ^{119}Sn$(d, p\gamma)$ data

performed within the scope of this thesis, it can be concluded that the QPM suggests in the LEDR of ^{120}Sn *i)* a concentration of comparably pure single-particle configurations between 5 and 7 MeV, and *ii)* that these single-particle configurations in fact correspond to an oscillation of the excess-neutron skin. However, it is not excluded that other, more complex configurations exhibit the same neutron-skin character. The next section will discuss the isoscalar response to (α, α') in ^{120}Sn and how the six relevant single-particle configurations contribute to it.

5.3 Isoscalar Response

Experimental ^{120}Sn$(\alpha, \alpha'\gamma)$ cross sections determined in Chapter 2 are contrasted with the experimental (γ, γ') cross sections in the following section. Theoretical counterparts were predicted by the QPM+Reaction calculations introduced in Chapter 4.3.

The reaction part allows to separate the excitation into a Coulomb-only and nuclear-only part, in addition to the combined nuclear+Coulomb, or total, cross sections. However, interference between the Coulomb and nuclear parts is possible and their cross sections do not add up coherently to give total values. Figure 42 presents the three results obtained from the QPM transition densities and level energies. The given theoretical cross sections have been integrated over the experimental spectrometer acceptance by use of the deflection function shown in Fig. 35. Comparing the top and mid panel of

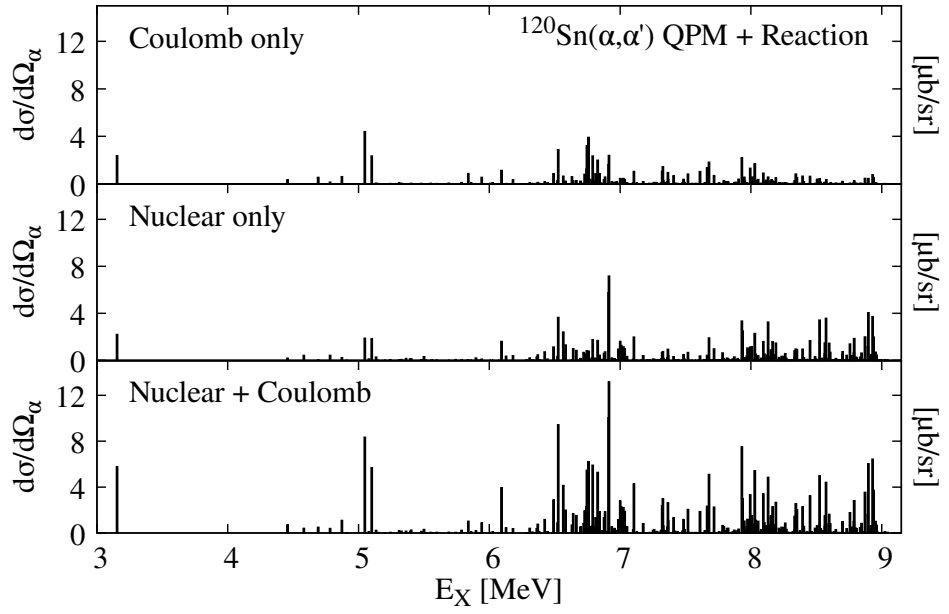

Figure 42: QPM+Reaction (α, α') cross sections for Coulomb interaction only (*top panel*), nuclear interaction only (*mid panel*), and both interactions combined (*bottom panel*). Cross sections have been integrated over the experimental spectrometer acceptance.

Fig. 42 shows the importance of the nuclear interaction, especially at higher excitation energies. Interestingly, the total cross sections presented in the bottom panel are fragmented throughout the energy range. While the cross sections vary over an order of magnitude between states, no concentration of strong states is predicted. This finding is in contrast to the theoretical predictions in ^{124}Sn performed with identical reaction calculations but nuclear-structure input from the RQTBA and an alternative QPM realization [43, 96].

The employed reaction theory predicts (α, α') cross sections based on transition densities and their response to the isoscalar dipole operator [43]. Final TRDs were obtained for each QPM state based on the one-phonon contributions, i.e., in first order from the six relevant phonons presented earlier. This means that the more complex configurations especially present above 7 MeV are not reflected in the state-by-state TRDs. However, these configurations are expected to have a more isovector character, to take place deeper inside the nucleus, and, thus, to only have minor impact on the surface-sensitive (α, α') cross sections. Instead, the six relevant TRDs shown in Fig. 41 resemble a surface mode with isoscalar contributions inside the nucleus.

Since experimental ^{120}Sn$(\alpha, \alpha'\gamma)$ cross sections were obtained in bins of 200 keV, the comparison of $(\alpha, \alpha'\gamma)$ and (γ, γ') in experiment and theory, as shown in Fig. 43, was also done in a binned manner. Panels (*a*) and (*b*) of Fig. 43 present the experimental cross sections, while Panels (*c*) and (*d*) show the theoretical predictions. Both experiments are (mostly) sensitive to the ground-state γ decay. However, the binned (γ, γ') data were obtained only from discrete transitions and do not include unresolved strength.

The (α, α') data may overestimate the cross section for 1^- states around and below 5 MeV due to the possible population of 2^+ states which could not be disentangled in the spectra with the given energy resolution. Note that the highest-lying identified transition was a $2^+ \rightarrow 0^+_1$ transition at 4524 keV. Contaminations from α scattering on ^{12}C and ^{16}O could be excluded thanks to the narrow gate on $|\mathrm{E_X} - \mathrm{E}_\gamma| \leq 150$ keV and the kinematic shift due to the much lower masses of these nuclei. Even though statistics are very low, the visible ground-state diagonal observed and above background in the coincidence matrix (see Fig. 22) indicates that these are in fact γ-rays decaying to the ground state of ^{120}Sn. The errors given in Fig. 43 (*a*) are the statistical uncertainties based on the number of events in each bin, after random-background subtraction. Thus, error bars can reach unphysical values below 0.

Comparison of the $(\alpha, \alpha'\gamma)$ and (γ, γ') experiments shows a rather similar behavior. The strength is broadly distributed and two shallow peaks form around 6.4 MeV and 8 MeV. Unfortunately, though, statistical uncertainties are large in $(\alpha, \alpha'\gamma)$, deeming the data

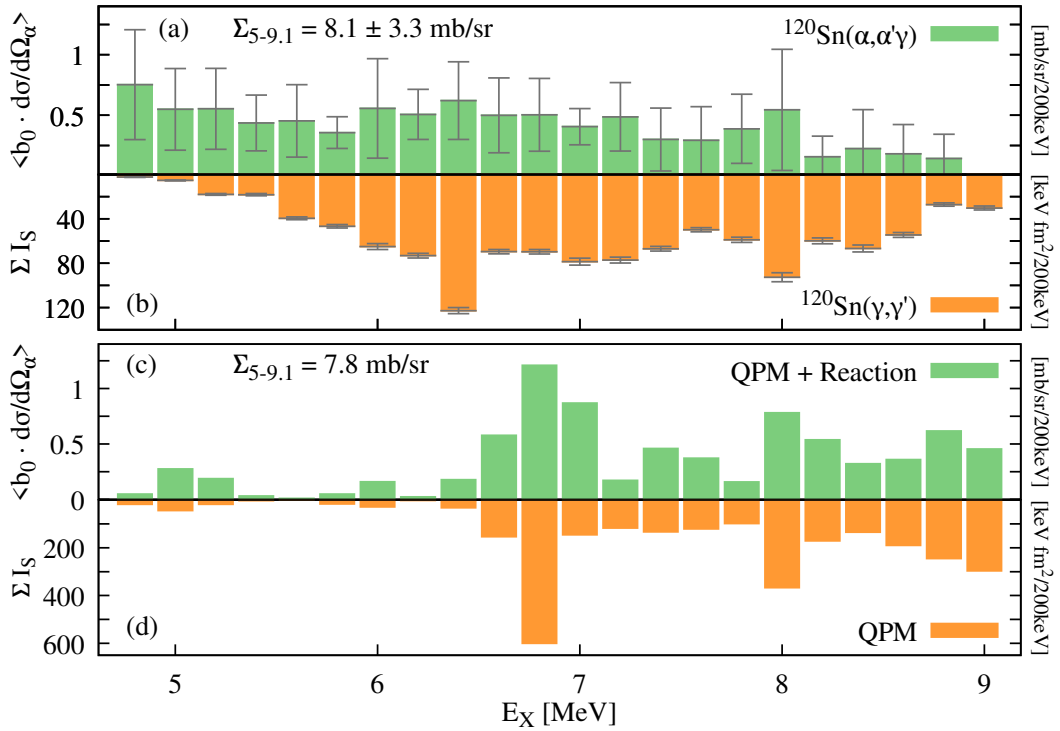

Figure 43: Experimental ^{120}Sn$(\alpha, \alpha'\gamma)$ (*a*) and ^{120}Sn(γ, γ') (*b*) cross sections and corresponding QPM(+Reaction) cross sections in bins of 200 keV (*c*, *d*). Experimental (γ, γ') values were obtained from only discrete identified transitions and do not include unresolved strength.

set inconclusive concerning such finer structures. A distinct concentration at lower energies, as observed in the continuous ^{124}Sn$(\alpha, \alpha'\gamma)$ and ^{124}Sn$(^{17}$O$, ^{17}$O$')$ analyses [42, 44], seems not to be prominent though. However, the overall response to (α, α') indicates that there is a non-negligible contribution of isoscalar strength to the LEDR in ^{120}Sn, albeit seemingly more fragmented. The data may, thus, allow to suggest a less pronounced concentration of the isoscalar response and the corresponding surface excitations in ^{120}Sn.

To further investigate this fragmentation of isoscalar strength, theoretical predictions are consulted. The QPM results presented in the lower panels of Fig. 43 seem to underestimate the binned cross sections at below 6.5 MeV. This is due to level density and binning effects, as will become clear shortly when discussing Fig. 44. Interestingly, the integrated theoretical (γ, γ') and $(\alpha, \alpha'\gamma)$ cross sections shown in Fig. 43 exhibit a similar behavior, with most of the strength between 6.5 and 9 MeV and two accumulations at 6.8 MeV and 8 MeV. No strong distinction between the two theoretical distributions is observed. The accumulation of strength around two energies can be expected to flatten out and move towards lower energies with a larger model space and increased fragmentation.

The summed theoretical $(\alpha, \alpha'\gamma)$ differential cross section between 5 and 9.1 MeV, folded with the QPM ground-state γ-decay branching, amounts to $\sum_{5-9.1}^{QPM} = 7.8\,\mathrm{mb/sr}$ and is well in agreement with the experimental value of (8.1 ± 3.3) mb/sr. Even though a structural interpretation based on the shape of the experimental response is difficult, the summed absolute value suffers less from statistics per bin and depends more on uncertainties of γ-ray efficiency, dead-time normalization, target thickness, scattering-angle calibration, and integrated beam-current values. It needs to be noted, though, that the seemingly great quantitative agreement is elusive, as the mentioned inaccuracies could, in the worst case, affect the true experimental values by up to a factor of two. However, the right order of magnitude is certainly reproduced by the QPM. Under the assumption that the summed $(\alpha, \alpha'\gamma)$ cross sections are representative, the agreement between theory and experiment is an interesting finding. It suggests that a significant part of the LEDR in ^{120}Sn not only has isoscalar and surface character, but is in fact generated by strong single-particle configurations.

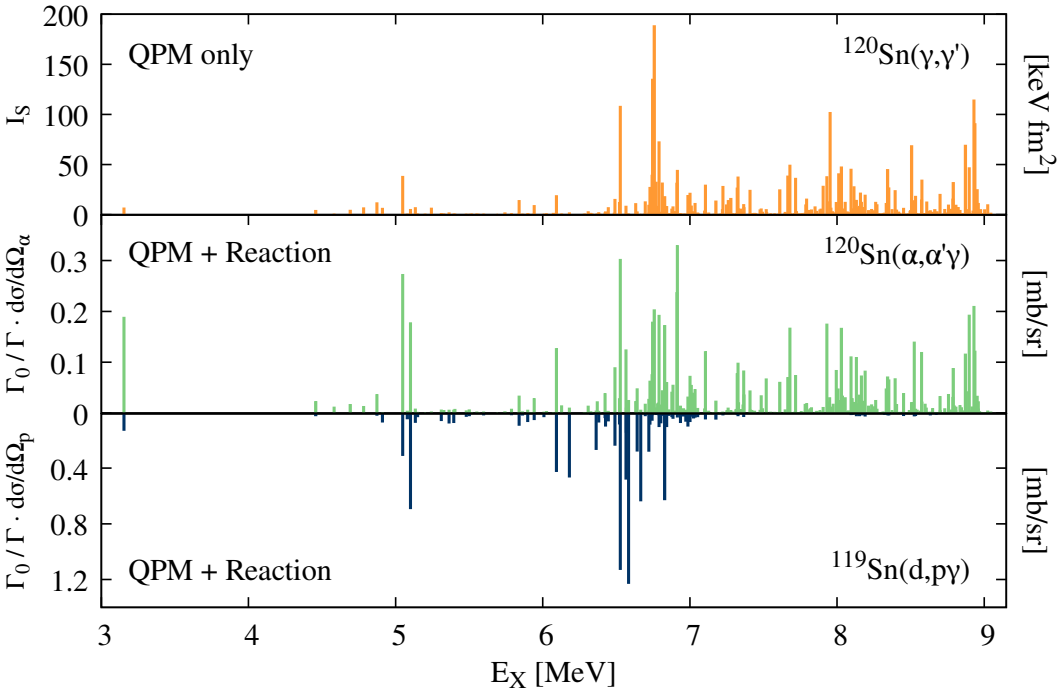

Figure 44: State-by-state comparison of QPM cross sections for (γ, γ') (*top panel*), $(\alpha, \alpha'\gamma)$ (*mid panel*), and $(d, p\gamma)$ (*bottom panel*). All data were folded with the QPM ground-state γ-decay branching.

The fragmentation of isoscalar strength within the QPM is investigated on a state-by-state basis in Fig. 44. It shows the QPM(+Reaction) differential cross sections for (γ, γ'), $(\alpha, \alpha'\gamma)$, and $(d, p\gamma)$ for each QPM state, taking into account ground-state decay branching b_0 and particle-detector solid angles $\Omega_{\alpha,p}$ from the hadronic experiments. Since the

data are not affected by rough binning, a distribution of states with comparably high $(\alpha, \alpha'\gamma)$ cross sections throughout the energy range can be seen in the center panel. Several states with a high cross section in $(\alpha, \alpha'\gamma)$ are comparably weak in (γ, γ'). While the $(d, p\gamma)$ values represent only the $(3s_{1/2})^{-1}(3p_{3/2})^{+1}$ and $(3s_{1/2})^{-1}(3p_{1/2})^{+1}$ contributions, and are shown for comparison here, the $(\alpha, \alpha'\gamma)$ values are based on all one-phonon contributions, as explained earlier. Even though 2ph+3ph contributions were excluded in the TRDs used for (α, α') reaction calculation, significant isoscalar response is reproduced throughout the LEDR of ^{120}Sn and, as discussed above, the summed cross section even matches the experimental value.

It can be concluded that the low statistics of the ^{120}Sn$(\alpha, \alpha'\gamma)$ experiment hamper a structural interpretation and deem the experimental results unsatisfactory, independent of the suboptimal γ-ray energy resolution. However, a considerable amount of γ-ray ground-state transition strength could be identified above 5 MeV and averaged γ-ray angular distributions support the $E1$ character of these decays. The assumed isovector character within the LEDR, which was attributed to the low-energy tail of the IVGDR [42], cannot be excited in the employed reaction. Thus, the observation of $E1$ strength excited via α scattering proves that an isoscalar and surface character is evident in the LEDR of ^{120}Sn.

5.4 Summary and Outlook

Electric dipole excitations are a fundamental mode of excitation in atomic nuclei across the nuclear landscape. While a vast manifestation of $E1$ strength is located above the neutron-separation energy in form of the Isovector Giant Dipole Resonance, additional nuclear-structure phenomena cause the emergence of weaker transition strengths below S_n. This strength is referred to as Low-energy Electric Dipole Response (LEDR) within this thesis, without further implication of the generating structures. Albeit much weaker, its importance to our understanding of the interaction between nucleons on the smallest scales, as well as stellar nucleosynthesis at astrophysical scales is invaluable. Common among most of the investigated stable nuclei is a concentration of $E1$ strength that emerges above 4–5 MeV and extends up to $S_n = 9.1$ MeV, which represents the majority of the LEDR. Historically, this accumulation of $E1$ strength, well below the IVGDR, was interpreted in a macroscopic three-liquid model as an oscillation of the neutron-skin against an isospin-saturated (N=Z) core. For decades, the work-horse experiments, and responsible for the broad knowledge on the LEDR strength throughout the isotopic chart, were (γ, γ') measurements using bremsstrahlung photon beams. However, throughout the last two decades, the excitation of LEDR states via hadronic probes was exploited in order to investigate the generating mechanisms, in addition to the overall $E1$ strength. The complementary investigation of (γ, γ') and $(\alpha, \alpha'\gamma)$ experiments revealed a structural distinction within the LEDR of ^{124}Sn and other nuclei, separating the states into (at least) two groups. In ^{124}Sn, the group at energies below 7.5 MeV showed a more isoscalar and surface-mode character, as was supported by theory. The other group, extending up to S_n, is believed to be generated by complex and more isovector configurations and was attributed to the low-energy tail of the IVGDR. In pursuit of the idea to find and understand more generating mechanisms in the LEDR of atomic nuclei, this thesis dealt with two new experiments and a consistent comparison to theory based on the prediction of the true experimental observables.

Within the scope of this thesis two experimental data sets investigating the LEDR of ^{120}Sn with hadronic probes were analyzed and compared to results from a high-sensitivity (γ, γ') experiment. The ^{119}Sn$(d, p\gamma)$ experiment was the first of its kind to reach the presented level of sensitivity and, together with the analysis methods developed in this thesis, constitutes a new tool to study the single-particle content within the LEDR of atomic nuclei. The combination of ground-state diagonal gate and (d, p) transfer reaction enables a level of selectivity which is unprecedented in studies on the LEDR with hadronic probes. The implemented Doppler correction allows to unambiguously identify ground-state γ decays of individual states in an energy region where the high

level density can make spectral analysis challenging in (γ, γ') experiments using bremsstrahlung. However, high-sensitivity (γ, γ') data are still preferable beforehand to chart the LEDR in a given nucleus. A spin determination for each observed state is possible via the analysis of γ-ray distributions relative to the direction of the recoiling nucleus, i.e., the Doppler angle.

The ^{120}Sn$(\alpha, \alpha'\gamma)$ experiment employed an experimental method successfully developed over the last 10 to 15 years and profited from the even longer experience with α scattering as an isoscalar surface probe. A considerable amount of isoscalar $E1$ strength was observed above 5 MeV, showing that the LEDR in ^{120}Sn does have isoscalar surface-mode contributions and separating it from both the IVGDR above S_n and the isovector part within the LEDR below S_n. The latter is expected to gain importance towards higher energies. The comparison to (γ, γ') data seems to suggest a broad fragmentation of the isoscalar strength throughout the LEDR of ^{120}Sn, but for an unambiguous conclusion and a comparison to the case of ^{124}Sn a remeasurement with an optimized setup will be necessary. As a first step, the reproduction of the ^{124}Sn$(\alpha, \alpha'\gamma)$ data by the QPM approach presented here needs to be validated. A systematic investigation of the $(\alpha, \alpha'\gamma)$ response on all stable even-even Sn isotopes could shed more light on the dependence of the isoscalar strength on neutron excess or shell-structure effects. For this, a binned analysis might be sufficient and a simpler setup with higher γ-ray detection efficiency using, e.g., LaBr scintillation detectors would be preferable.

The detailed QPM calculations analyzed in this thesis are able to reproduce the overall $E1$ response in ^{120}Sn on a quantitative level and reflect the change of structure towards higher energies and the corresponding decrease in ground-state decay branching. The latter gives an explanation for the discrepancy between (p, p') CoulEx and (γ, γ') data using bremsstrahlung. Additionally, quantitative agreement was obtained for the summed strengths populated in $(d, p\gamma)$ and $(\alpha, \alpha'\gamma)$, as well as the centroid energy of the response in $(d, p\gamma)$. Fragmentation and decay branching to higher lying states are expected to increase with a larger model space and are, thus, underestimated due to technical limitations of the QPM calculations. Single-particle energies were neither determined from nor adjusted to experimental data, but were obtained from the EDF approach directly. A satisfactory placement of the configurations accessible in ^{119}Sn$(d, p\gamma)$ was found. Furthermore, all of the strong single-particle configurations are predicted to be concentrated between 6 and 7 MeV in ^{120}Sn.

The single-particle content of states excited in ^{119}Sn$(d, p\gamma)$ was identified through the combination of QPM nuclear-structure calculations and dedicated reaction theory. Results from experiment and theory show that single-particle configurations play an im-

portant role in the low-energy part of the LEDR in ^{120}Sn. The theoretical prediction of both excitation and γ decay of LEDR states for such a transfer experiment was done for the first time in this thesis and enables further studies employing the $(d, p\gamma)$ reaction with the SONIC@HORUS setup.

The investigation of QRPA transition densities revealed that most of the relevant one-phonon contributions in ^{120}Sn exhibit the neutron-skin character expected in parts of the LEDR. Quantitative agreement to $(\alpha, \alpha'\gamma)$ was obtained from the QPM+Reaction calculations based on these one-phonon TRDs. This finding may indicate that the macroscopic picture of neutron-skin oscillation, commonly referred to as the Pygmy Dipole Resonance and historically thought to be the major cause of LEDR in atomic nuclei, is in fact generated by a few strong single-particle configurations. The latter was suggested in earlier theoretical studies [47, 48] and the combined results obtained in this thesis provide the first experimental evidence for this connection between the microscopic and macroscopic pictures.

While two- and three-phonon contributions are expected to be negligible for the (α, α') reaction, the limitation to one-phonon TRDs may obscure the interpretation of the full QPM wave functions. Deeper insight into the complexity of the LEDR will only be gained once a theoretical formalism is available that determines physical cross sections based on the full QPM input.

The QPM model space is unlikely to be increased in the near future, as the mathematical limitation arises from the high level density and overlapping level energies instead of computational power [131]. However, the reproduction of general nuclear-structure features in ^{120}Sn, as investigated in this thesis, is striking and the level of fragmentation is satisfactory. A systematic investigation of the single-particle character of QPM states throughout the Sn isotopic chain and over a wider mass region is advisable. Two $(d, p\gamma)$ experiments investigating the LEDR of ^{116,118}Sn were performed with SONIC-V3@HORUS and are currently being analyzed [132]. They will complete the systematics in the Sn chain for nuclei accessible via (d, p) reactions on stable targets. The placement of relevant single-particle energies may vastly differ in lighter nuclei and measurements on, e.g., ^{43}Ca, ^{49}Ti, and ^{61}Ni will help to understand the overall behavior. Additionally, a ^{207}Pb$(d, p\gamma)$ measurement could complement the recent ^{207}Pb(d, p) study without γ-ray detection [122]. Future experiments may also profit from a conventional magnetic-spectrometer setup using the Super-Enge Split-Pole Spectrograph available at Florida State University, which is currently being extended by an array of high-efficiency $CeBr_3$ detectors for coincident particle and γ-ray detection [133].

The importance of the $3p_{1/2}$ neutron orbital, which was accessed in ^{119}Sn$(d, p\gamma)$, for semi-

direct neutron capture in the $N = 82$ region has been pointed out in Ref. [134]. In fact, the demanded theoretical prediction of excitations in unstable neutron-rich nuclei based on this orbital might be satisfied by EDF+QPM calculations in the future. The aforementioned systematic studies on single-particle energies using SONIC@HORUS will provide a test of the robustness of QPM predictions in stable nuclei and, thus, help to extrapolate the behavior to nuclei away from the valley of stability and relevant for the *r* process.

Complementary information on other single-particle configurations might be obtained by studying $(p, d\gamma)$ neutron pick-up reaction, probing the neutron-hole content of excited states. A ^{119}Sn$(p, d\gamma)^{118}$Sn experiment using the BaGeL and K600 spectrometers at iThemba Labs in Capetown, South Africa, has been proposed and was accepted by PAC recently. The corresponding reaction theory is currently under development [135] and a comparison to the aforementioned ^{117}Sn$(d, p\gamma)^{118}$Sn data is desired.

A comparison of the ground-state decays observed in ^{120}Sn$(p, p'\gamma)$ at energies comparable to the ^{119}Sn$(d, p\gamma)$ experiments presented here might yield additional information of the structural evolution in ^{120}Sn. A corresponding data set has recently been analyzed within the *Oslo* method [136], but the direct ground-state decay strength is obtainable from the data as well.

Further confirmation of the (d, p) reaction theory at the used energies and detection angles is necessary. The upcoming ^{115,117}Sn$(d, p\gamma)$ data sets were taken triggerless and will, thus, allow to quantitatively benchmark the QPM+Reaction calculations by extracting absolute excitation cross sections via a normalization measurement performed with the target chamber for nuclear astrophysics. Reaction theory already predicts angular distributions for reaction ejecta, but the experiment presented here only detected protons at roughly one angle relative to the beam. Proton angular distributions over a wider angle range and coincident γ-ray detection will help to support theoretical predictions and may even allow to disentangle specific configurations from each other. However, a dedicated detection chamber would have to be built exploiting the symmetries of the HORUS setup and allowing to sample the proton angular distributions on several sensitive angles, also forward of 90°. Alternatively, a combination of γ-ray detectors and the flexible scattering chamber already existing at the 10 MV FN-Tandem accelerator laboratory of the University of Cologne is possible. In both scenarios, especially the light nuclei mentioned above seem reasonable candidates, as the strength is collected in fewer states, increasing statistics per transition and possibly allowing the use of LaBr scintillation detectors, depending on level density. The latter would not suffer from neutron damage and less from count-rate effects. Thus, satisfying coincidence statistics

at each proton detection angle might be acquired within reasonable experiment times, especially thanks to the highly reduced dead time of the data acquisition system presented in Chapter 6.

Part II

Digital Signal Processing for Nuclear Physics Experiments

6 NuDAQ – A High-Resolution and Low-Dead-Time Data Acquisition System

Fully digital data acquisition systems (DAQs) have become state-of-the-art over the last decade. While some setups still use existing analog electronics, the advantages of digital DAQs in terms of available channel number, dead time, flexibility, and processing speed are evident. Within this thesis, a new DAQ system was planned and commissioned for all nuclear physics experiments performed at the 10 MV FN-Tandem accelerator laboratory of the University of Cologne (UoC). It was the aim to build a system that satisfies the needs of any experimental application, is highly flexible, and easy to use for the experimentalist. The system is built around three types of commercially available modules built by CAEN S.p.A. and the corresponding acquisition software CoMPASS. One of the modules was developed specifically based on the demands posed within this thesis and excels at high-resolution γ-ray spectroscopy using High-Purity-Germanium (HPGe) detectors. A centralized server station was set up in the laboratory which allows permanent access to DAQ servers and is connected to each setup via fibre-channel cables. See Appendix C.1 for an overview of relevant connections in the laboratory. Since commissioning in early 2020, a number of experiments have utilized the system [95, 137–140] and first publications on data taken with it are in preparation or have been submitted [141, 142] at the time of writing this thesis. The following chapter introduces the system and presents the conducted performance tests.

6.1 Overview

The NuDAQ system is composed of several VX1730 and V1782 digitizers and one V2495 logic module built in the VME-format by CAEN S.p.A . Two firmware versions are available which allow to process typical preamplifier-shaped signals and to directly sample fast signals from, e.g., scintillation detectors or multi-channel-plates (MCPs). The DPP-PHA firmware is intended for pulse height analysis of preamplifier signals and is supported by both VX1730 and V1782 digitizers. The DPP-PSD firmware allows to integrate fast signals over two user-selectable time regions and perform pulse shape discrimina-

tion based on these two integrals. Especially interesting is the digital Constant-Fraction-Discriminator (CFD) implemented in the DPP-PSD firmware which gives a finer time information than the sampling frequency (see Fig. 50). The DPP-PSD firmware is only supported by the VX1730 digitizer. Lastly, the V2495 is a user programmable logic unit housing an Altera Cyclone V Field-Programmable-Gate-Array (FPGA). It is equipped with high-density input and output cards and allows to process up to 192 logic signals simultaneously in real-time. A dedicated firmware was developed within this thesis which enables an online data reduction based on multiplicity filtering, handles individual per-channel vetos, and is configurable via USB.

To give an overview of performance demands, the experimental setups currently available at the UoC 10 MV FN-Tandem accelerator laboratory are introduced in the following. Typical nuclear-physics experiments performed at UoC utilize solid-state, scintillation, or gas detectors for γ-ray and particle detection with signals shaped by dedicated preamplifiers. The three permanent nuclear-physics experimental setups are the *Plunger* setup, the *Orange* spectrometer, and the HORUS spectrometer. The *Plunger* setup consists of eleven HPGe detectors centered around the Cologne-Plunger device [143] and is used for nuclear level-lifetime determination via the Doppler-shift of γ-rays being emitted in flight. If the reaction allows, additional solar-cell particle detectors are mounted inside the Plunger to provide particle-trigger. An upgraded setup with 24 HPGe detectors is currently being built [144]. The *Orange* spectrometer allows to directly measure internal-conversion coefficients by detecting conversion electrons together with the competing γ decay [145, 146]. HPGe solid-state or LaBr scintillation detectors are used in this setup. The HORUS spectrometer consists of 14 HPGe detectors, six of which are equipped with active Anti-Compton BGO detectors [147, 148]. For a direct measurement of nuclear level-lifetimes in *fast-timing* experiments, the six HPGe detectors inside BGO shields are replaced with LaBr detectors and additional LaBr detectors are placed inside HORUS where space allows [149]. For particle-γ coincidence spectroscopy, HORUS is often combined with the *Sonic* chamber housing 12 Silicon detectors or 24 detectors coupled to 12 telescopes in the $\Delta\mathrm{E} - \mathrm{E}$ configuration [89]. The γ-ray energies of interest range from below 3 MeV for lifetime measurements up to approx. 18 MeV for nuclear astrophysics experiments. Additionally, a dedicated gas-ionization-detector with several preamplified anode signals and fast time-of-flight detectors using MCPs for signal generation are available at the Accelerator-Mass-Spectroscopy setup. With the constant modernization of setups, the number of active detectors for an experiment has reached up to 40 channels and will increase further in the future. For effective experimental campaigns, a DAQ system has to be capable of processing this number of channels simultaneously while maintaining high throughput and the best possible time

and energy resolution.

Two major caveats of the predecessor sytem built around the XIA DGF-4C Rev. F digitizers are ADC non-linearities and a high dead time caused by consecutive readout. Differential non-linearities were discussed in Refs. [81, 91] and cause severe peak distortion and unsteady energy calibration. The V1782 digitizers were specifically purchased to eradicate this issue and the linearity of the utilized Analog-Digital-Converter (ADC) is discussed in Section 6.5. The CAMAC standard used by the XIA system forces a consecutive read-out of the whole system, during which no new hits can be processed, whenever one module signals a full buffer. With the number of detector channels currently required, this may easily cause dead times in excess of 50 %, independent of the dead time induced by pile-up. Thanks to the modern and independent fibre-channel connection of each digitizer in the new system, this effect is virtually negligible, as will be shown in Section 6.8.

In contrast to the XIA system, the new VX1730 digitizers allow direct processing of fast signals from, e.g., MCPs or scintillation detectors using photomultiplier tubes (PMTs), without analog signal shaping. The precise time resolution of the digital CFD implemented in the DPP-PSD firmware is currently under investigation, but was reported to be comparable to the traditional approach using Time-to-Amplitude-Converters (TACs) [150]. Thus, the established complex signal chain for *fast-timing* experiments [151] can be drastically simplified and higher statistics can be obtained. However, a traditional configuration with TACs being sampled by the V1782 digitizers is still possible and was found to result in a comparable time resolution [150].

While the drawbacks of the DGF-4C modules are mostly related to the technology standard available at the time of development [84], the digitizers had two features useful in experiments with HPGe detectors. First, each channel had a dedicated veto input which could be fed, e.g., by logic signals from BGO detectors. The logic state on the veto input could be used to dismiss detector signals online, or stored as a flag in the raw data for offline vetoing. Secondly, each detector input had a software-selectable electronic coarse gain and a fine gain adjustment was done in firmware. This feature made the system very flexible and allowed it to be used for γ spectroscopy experiments with energies ranging between 3 MeV and 18 MeV without adjusting preamplifiers. The newly commissioned V1782 digitizer features the same flexible input and allows to dismiss hits online via external veto signals for each detector input.

The two kinds of digitizers available with NuDAQ are presented in Section 6.2 with the corresponding firmware version being introduced in Section 6.4. An overview of the acquisition software CoMPASS and the established data flow from raw data to final anal-

ysis is presented in Section 6.3. Several linearity and resolution tests were conducted in order to quantify performance of the new system and results are shown in Section 6.5. The implemented logic for direct vetoing and the online multiplicity-filter are explained in Section 6.6 and Section 6.7, respectively. An estimation of pile-up related dead time per detector is discussed in Section 6.8, while Section 6.9 gives a direct comparison of the read-out related dead time between the XIA and CAEN systems. Finally, Section 6.10 summarizes the development and performance of NuDAQ and discusses future improvements.

6.2 Digitizers and Logic Module

A front view of the VX1730 and V1782 digitizers together with the V2495 logic unit is shown in Fig. 45. The modules meet the VME standard format, which allows communication between different modules via the backplane connectors. However, in the case of NuDAQ, the VME backplane is only used as a power source. All necessary connections are accessible from the front and communication takes place via fibre channel for the digitizers or via USB for the logic unit. Both digitizer types share a similar front panel design shown in Fig. 46, except for detector inputs. Clocks are synchronized via a Phase-Locked-Loop (PLL) which is forwarded from a chosen clock-master module throughout the chain of modules via the front *CLK Out* and *CLK In* connectors. A clock signal of 50 MHz or 62.5 MHz is generated on each *CLK Out* connector, depending on the reference frequency needed by the next module in the chain. While all clocks are always synchronized, the internal timestamp counters have to be reset simultaneously at the beginning of a measurement run. This start signal ensures synchronized timestamps between modules and is propagated from the clock master module through the chain via the dedicated *Trig Out* and *Trig In* connectors. Communication with acquisition software and data readout is done via the CONET protocol through fibre-channel connectors at the front. The CONET protocol allows chaining of up to eight modules per connection to the host PC and a bandwidth of 80 MB/s is available per link. Digitizers store data in an onboard ring buffer, which is continuously read out without interrupting acquisition. This allows for sufficient data throughput for typical experiments via just one fibre-cable which is chained through the up to eight digitizers. During all experiments performed with the system so far, the total data rate rarely exceeded 20 MB/s. The clock, Trig-In/Trig-Out, and fibre chains are independent from each other, but convention was made that the left most module in a crate is always chosen as the reference or master module for all three cases. The internal clock source switch has to be set accordingly in each module, see Fig. 45. Status LEDs on the front indicate that clock and fibre chain are properly set up.

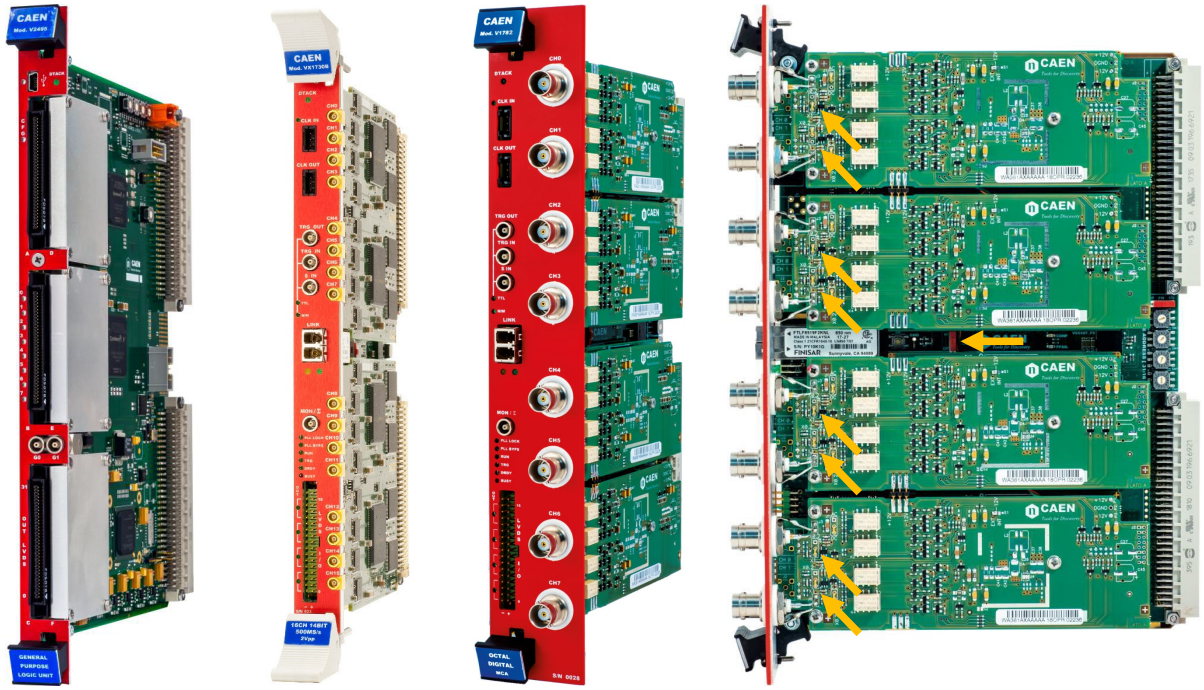

Figure 45: Front view of logic module and both digitizers (left three). Side view of V1782 internals (right most) with marked clock-source selector switch in the center and attenuation jumpers close to each BNC input. Figures adopted from Refs. [152–154].

Each digitizer offers a General-Purpuse-Input-Output front connector (GPIO) which can be used for special applications. Its behavior depends on the loaded firmware and the selected firmware settings. In any case, communication takes place via the Low-Voltage-Differential-Signaling standard (LVDS) on the 34-pin flat-cable connector. Two pins provide a grounded connection and 16 differential pairs are available for communication and can be grouped into input or output banks of four pairs each. With NuDAQ, this connector is used to either receive veto signals directly from BGO detectors or to send trigger requests to the multiplicity unit and receive trigger acknowledgements from it. In the latter case, the multiplicity module also handles veto signals.

The V1782 digitizer supports the DPP-PHA firmware (see Sec. 6.4) and offers eight single-ended BNC inputs for detector signals which are sampled via 16 bit 100 MHz ADCs (Linear Technologies *LTC2208-16*). The internal reference clock has a frequency of 50 MHz and the LVDS connecter can be used for direct veto input per channel or as a split trigger-request output and trigger-acknowledgement input. In both cases, channels acquire data independently, unless specified via firmware settings. Each detector input has an input impedance of 1 kΩ and a software-selectable electronic gain in four steps. Additionally, an attenuation factor of 5 can be enabled via an internal jumper on the digitizer circuit board. The combination allows input voltage ranges of

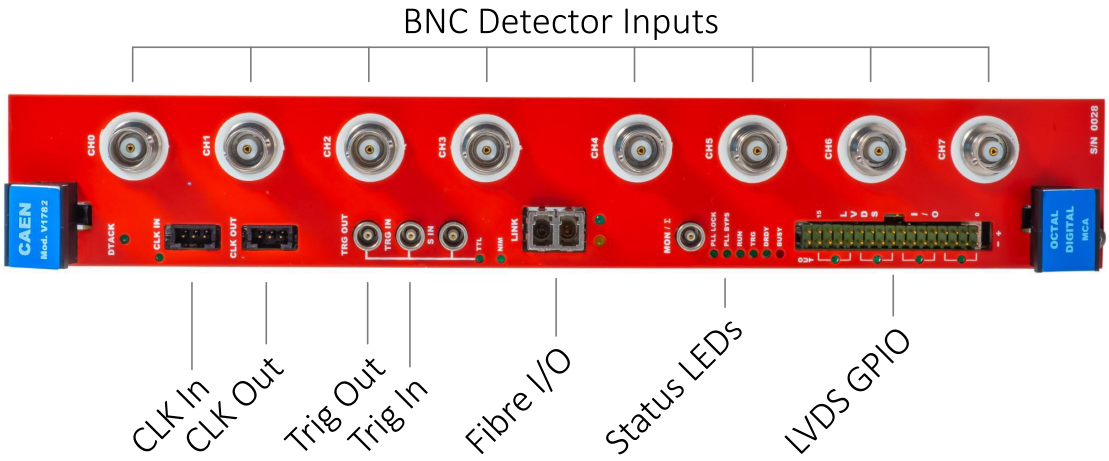

Figure 46: V1782 front connectors. The VX1730 shares the same inputs but has 16 MCX detector inputs. Figure adopted from Ref. [153].

0.125/0.25/0.5/1V and 0.625/1.25/2.5/5V, respectively. The latter option offers sufficient flexibility via the software-selectable gain for all typical experiments performed at UoC and the hardware jumpers do not have to be altered between experiments. The V1782 was recently developed by CAEN based on the demands presented in this thesis and further details on the module can be found in Ref. [153]. As will be shown in Section 6.5, it delivers optimum resolution for HPGe detector signals and is, thus, the preferred choice for γ-ray spectroscopy with HPGe detectors.

For all other applications the VX1730 digitizer with 16 MCX detector inputs and 14 bit 500 MHz ADCs (Intersil *ISLA214P50*) is used. It supports the DPP-PHA and DPP-PSD firmware versions for both fast and shaped detector signals. The internal reference clock has a frequency of 62.5 MHz and all inputs have an impedance of 1 kΩ. It offers two software-selectable input ranges of 0.5 V and 2 V and has no internal attenuation jumpers. All 16 channels can acquire data independently, but two neighbouring channels share internal trigger logic. Thus, a coupled acquisition of, e.g., telescope detectors can easily be realized with the corresponding firmware settings. The LVDS connector offers the same 16 signals as the V1782. In order to have the channels acquire data independently and make use of the multiplicity filter, only every second input (8/16) is used. In this case, the upper eight LVDS signal pairs emit the trigger-request signal for each of the eight connected detectors and the lower LVDS pairs receive trigger-acknowledgement signals. A more detailed overview of the module can be found in Ref. [152]

The V2495 logic unit offers six 68-pin high-density connectors with three serving as input and three as output. Each 68-pin LVDS connector can handle 32 LVDS logic signals and special cables were manufactured in order to split up the standard 34-pin flat ca-

bles and merge them into the corresponding 68-pin connector. The onboard FPGA is used to implement clocked logic with the system clock of 50 MHz as reference. It can be programmed directly with synthesized VHDL code, or via the graphical software SciCompiler [155] available from CAEN S.p.A. The latter allows to easily configure real-time logic in a visual design suite and automatically generate VHDL code specifically for the V2495. It was used to implement the multiplicity-filter firmware presented in Section 6.7.

6.3 CoMPASS Acquisition Software and Data Flow

The CAEN Multi-PArameter Spectroscopy Software (CoMPASS) represents the main interface for an experimentalist to work with NuDAQ. It manages the set-up of digitizer types and visualizes live detector signals and spectra to help optimizing parameters, starts and stops measurement runs, and stores statistics information after a run has properly been stopped. Being actively developed under Linux, frequent updates and improvements are currently available and no additional workload due to software maintenance or development arrises. CoMPASS runs on the centralized acquisition serves and connects to digitizers at each experimental setup via fibre-channel.

CoMPASS fills energy and, if desired, time-difference spectra with live data when acquisition is running and listmode data are stored to file either in either one continuous file, several files of a configurable maximum size, or in one file per digitizer channel. Experimental monitoring can be performed with periodic spectra which are filled and written to disk, e.g., every 10 minutes. These spectra can be investigated from within CoMPASS or with the spectrum analysis software of choice, such as the in-house developed tool *hdtv* [156]. While CoMPASS allows to apply so-called *user-selections*, i.e., software coincidence conditions, it is only used to record data and analysis is done near-line or offline in order to keep the computational load on acquisition servers low.

Several options are available to store digitizer data for offline analysis and three levels of detail can be chosen. *RAW* data contain all valid hits, pile-up and saturation events, statistics information, and special *fake-events* informing the acquisition software, e.g., about an internal counter roll-over. The *UNFILTERED* data contain only valid hits without additional information and *FILTERED* data contain only hits which have passed the software selections applied in CoMPASS, if desired. The *RAW* data should be chosen in any case to conserve as much information as possible. In all three cases, stored data will be referred to as raw data in the following, unless specified otherwise. These raw data can be stored in comma-separated-text files, in a proprietary binary format, or in a ROOT tree. The latter option uses a data format inherited from the ROOT frame-

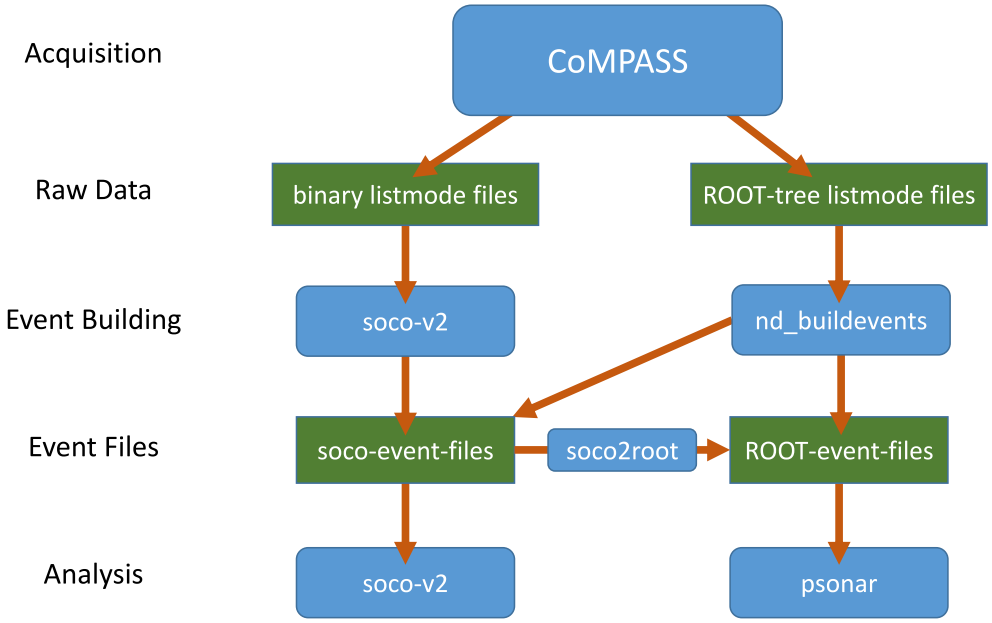

Figure 47: NuDAQ data flow chart from acquisition to analysis. Raw data taken with CoMPASS are stored in binary format or ROOT-tree files. Both *socov2* [158] and *nd-buildevents* [157] can be used to build events and store them in the *socov2* event-file format. Alternatively, events can be stored in another ROOT-tree file by *nd-buildevents* or converted via *soco2root* [159]. The general event structure is identical in both cases. Final analysis, e.g., filling of coincidence spectra and matrices, can be done with either *socov2* or *psonar* [78].

work and makes access to listmode data straightforward. Within this thesis, the standalone event-building software *nd-buildevents* was developed [157] which makes use of the ROOT file format and allows built events to be stored either in another ROOT tree or in a binary data format which is compliant with the in-house developed analysis software *socov2* [158]. Recently, the binary CoMPASS data format was also integrated into the event-building stage of *socov2* [150]. Both *socov2* and *nd-buildevents* are actively maintained and developed at the time of writing this thesis and follow slightly different approaches to event-building. However, the minute differences are beyond the scope of this thesis and should be taken from corresponding documentation found in Refs. [78, 157, 158].

An overview of the workflow from raw data to analyzed spectra is depicted in Fig. 47. It explains how data taken with NuDAQ can be sorted and timestamp-matched by both *socov2* and *nd-buildevents*. Files containing built events can be converted in either direction to make use of both analysis softwares *socov2* and *psonar*. The latter was developed within this thesis specifically for the analysis of SONIC@HORUS experiments [78]. Both tools allow to apply complex conditions to built events and fill spectra or matrices depending on the desired application.

6.4 Available Firmware Versions

6.4.1 DPP-PHA Firmware

Both digitizers support the *Digital-Pulse-Processing* firmware for *Pulse-Height-Analysis* (DPP-PHA). It is intended for use with typical preamplifier signals with short rise times in the order of 100 ns and an exponential decay with a decay constant in the order of 10–100 µs. Figure 48 illustrates how the preamplifier signal is transformed into a trapezoidal shape. The incoming signal is integrated over two time windows of equal length T_{Rise} which are separated by $T_{FlatTop}$. The difference of the two integrals is constantly calculated and forms the running filter sum. Typical values are $T_{Rise} = 5$ µs and $T_{FlatTop} = 1$ µs. Additionally, the algorithm corrects for the exponential decay of the incoming signal which ensures the trapezoid is flat and enables a precise energy determination independent of rate effects. The exponential decay constant τ is a crucial parameter for optimum resolution and is in the order of 50 µs for the HPGe detector preamplifiers used in-house. While a flat trapezoid indicates a roughly correct τ values, fine tuning is typically done by inspecting spectral energy resolution. In a second step, the continuously calculated filter sum is averaged over a region before the rising edge and a region on the flat top of the trapezoid. The length of the first region BL_{avg} determines how many filter samples are averaged to give the baseline information, and

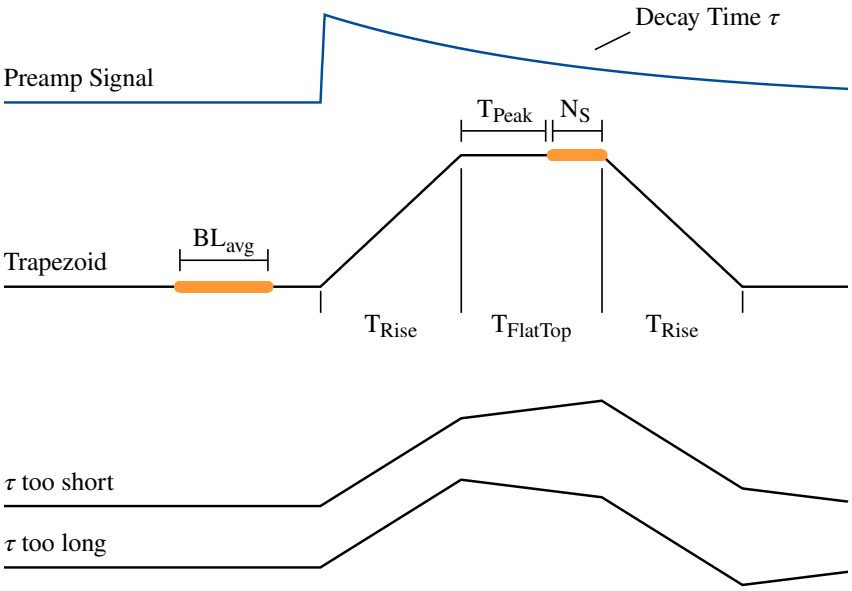

Figure 48: DPP-PHA firmware trapezoid filter (*black*) generated by integrating preamplifier input signal (*blue*). Several filter parameters are visualized and the time scale spans several µs. For further details see text. Figure adopted from [160].

the value N_S gives the number of samples to be used for pulse height determination. The second window can be delayed and moved along the flat top via the so-called *peaking time* (T_{Peak}). This ensures the N_S region is not affected by ballistic deficit or rise-time effects of the detector signal, which may distort the beginning of the flat top. The difference of both integrals gives the final pulse height, or energy value.

Triggering is done via an $\mathrm{RC}-\mathrm{CR}^2$ filter, in which the input signal is integrated once (RC) and differentiated twice (CR^2). It suffers less from pulse-height effects compared to a leading-edge trigger. The trigger is armed when the $\mathrm{RC}-\mathrm{CR}^2$ filter exceeds its threshold and released on the following zero-crossing. It takes the input rise time IRT as a parameter and crosses zero $1.5 \cdot IRT$ after the signal started to rise. For HPGe detectors used in-house, this rise time is about $IRT = 100-120$ ns, depending on detector size. A timestamp is stored which is equal to the clock cycle number at the zero crossing and is resolved in 10 ns with the V1782 digitizer or 2 ns with the VX1730 digitizer. A hit has been successfully processed by the trapezoid filter at the flat-top end and an additional hold-off time T_{HO} can be set before new triggers are accepted. This minimum time between two triggers amounts to $T_{run} = T_{Rise} + T_{FlatTop} + T_{HO}$.

Figure 49 displays how the time difference between to trigger signals $\Delta_\mathrm{T} = \mathrm{T}_2 - \mathrm{T}_1$ is

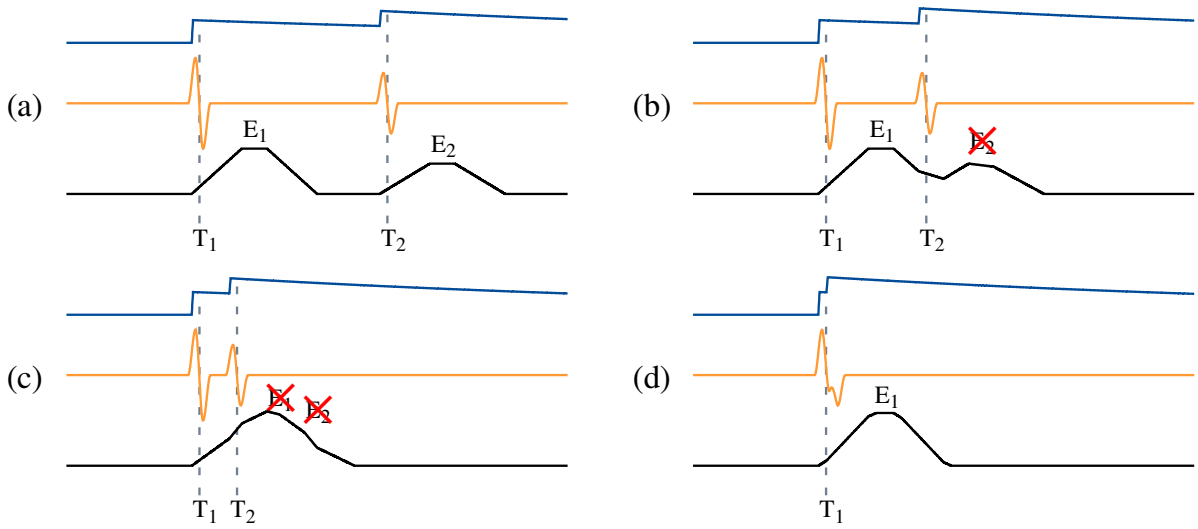

Figure 49: DPP-PHA firmware pile-up handling. Input signal (*blue*), $\mathrm{RC}-\mathrm{CR}^2$ filter (*yellow*) and trapezoid filter (*black*) for four scenarios. (*a*) Two hits are well separated in time, both are processed correctly. (*b*) Second hit closely follows the first one, but does not affect the first trapezoid. Both hits are triggered, energy information is only valid for the first hit. Second hit is marked as pile-up. (*c*) Both hits are triggered separately, but neither trapezoid information is valid. Both hits are marked as pile-up. (*d*) Two hits are so close in time that the $\mathrm{RC}-\mathrm{CR}^2$ filter cannot distinguish them. They are processed as one hit with a distorted trapezoid information. Figure adopted from [160].

used to identify and tag pile-up. The four panels correspond to the following scenarios:

a) $\Delta_{\mathrm{T}} > T_{Rise} + T_{FlatTop} + T_{HO} = T_{run}$ – Both hits are processed properly
b) $T_{Rise} + T_{FlatTop} < \Delta_{\mathrm{T}} < T_{run}$ – First hit valid, second is identified as pile-up
c) $1.5 \cdot IRT < \Delta_{\mathrm{T}} < T_{Rise} + T_{FlatTop}$ – Both hits are triggered, but unvalid / pile-up
d) $\Delta_{\mathrm{T}} < 1.5 \cdot IRT$ – Both hits are processed as one with distorted energy information

All mentioned parameters may be optimized depending on the input count rate, desired resolution, and general signal quality. However, it is beyond the scope of this thesis to give a general guideline on how to set filter parameters. Further information can be found in Refs. [153, 160].

6.4.2 DPP-PSD Firmware

The fast VX1730 digitizer supports the *Digital-Pulse-Processing* firmware for *Pulse-Shape-Discrimination* (DPP-PSD). It is intended for fast charge signals from, e.g., photomultipliers and makes use of the fast sampling frequency of 500 MHz. Figure 50 explains how information are obtained in this firmware. The incoming signal is triggered via a Constant-Fraction-Discriminator (CFD) and is integrated over two windows of length *ShortGate* and *LongGate*. Since the trigger is released slightly after the input rising edge, a part of the sampled signal is stored and the integration windows start at a time *PreGate* before trigger release. A simple pulse shape discrimination can be performed in the recorded data based on the ratio of the integrated values. For the experiments performed at UoC, however, this feature is typically not necessary and only the *LongGate* window is used for total energy determination. Similar to the DPP-PHA firmware, a trigger hold-off time can be set which extends beyond the longer integration window and pile-up is handled accordingly. However, the integration times are in the order of a few 100 ns, e.g., for LaBr detectors, and pile-up occurs much less compared to the slower DPP-PHA trapezoid filter at a given count rate.

Thanks to the digital CFD, the time information stored is much finer than the clock cycle length of 2 ns. The CFD zero crossing is interpolated between two adjacent samples, see the right panel of Fig. 50, and a timestamp is stored in units of 2 ps for the case of the VX1730 digitizer. However, the effective time resolution, i.e., the prompt time resolution, is certainly larger and is currently being investigated [150]. Further details on the DPP-PSD firmware can be found in Refs. [152, 160].

6.5 ADC Linearity and Energy Resolution

One major drawback of the established XIA system was the non-linearity of the ADC used for signal sampling. With this issue in mind, careful attention was put on the spec-

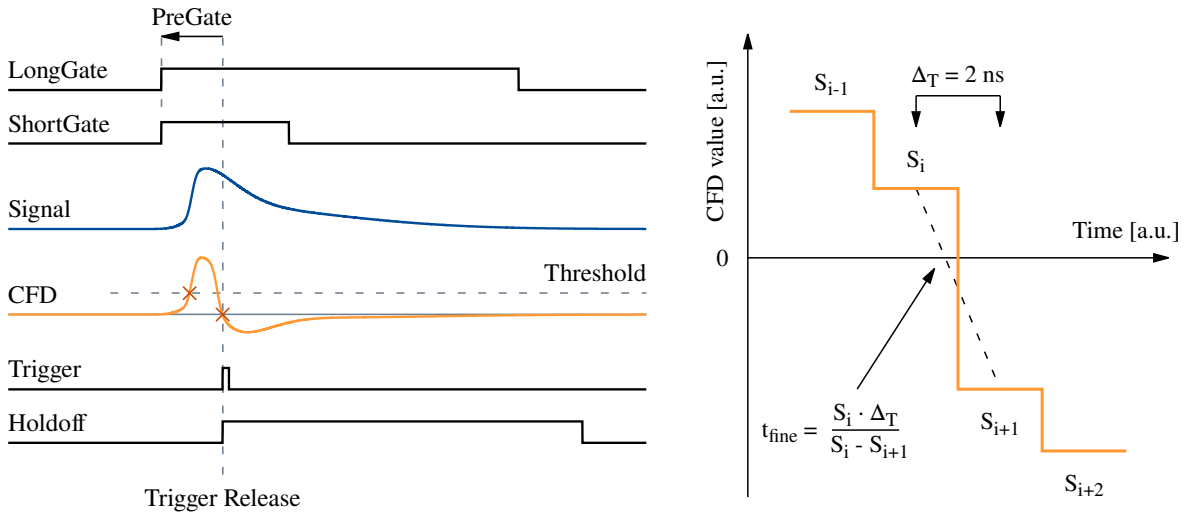

Figure 50: *Left*: Working principle of DPP-PSD firmware. Trigger is armed when CFD crosses threshold and released when consecutive zero-crossing is detected. Fast detector signals are integrated over *ShortGate* and *LongGate* intervals, starting at time *PreGate* before trigger release. The ratio of both integrals can be used for pulse-shape-discrimination. Further triggering is inhibited while *Holdoff* is high. Time scale spans a few hundred ns. *Right*: Interpolation of fine time information at zero-crossing between two CFD samples S_i and S_{i+1}. Figures adopted from Ref. [160].

tral linearity and rate-independent resolution of the new system from the beginning. One way to quantify ADC non-linearity is to take spectra of small artificial pulses with identical height and scan the DC offset, a constant voltage offset which is applied to the signal before sampling. With a perfectly linear ADC, the peak position in the energy spectra would be constant, i.e., independent of the DC offset. Any deviation from a chosen reference value indicates a non-linearity in the ADC transfer function and falsely shifts the determined pulse height to higher or lower values. Since preamplifier signals have an exponential decay, new signals often occur on the tail of a previous pulse and, thus, may have different reference baselines. Thereby, signals of identical pulse height are sampled in different regions of the ADC input range and are sometimes, but not always, affected by non-linearities. At low count rates this shift causes a step-function behavior of the energy calibration function [84], while overall peak shape may be satisfactory. At realistic count rates of 10–30 kcps, though, a severe peak distortion is observed, hampering the spectral analysis for any type of experiment.

ADC Linearity Calibration

The calibration procedure has been used to calibrate differential non-linearities (DNL) of the existing XIA system in Ref. [91] and a more detailed explanation can be found therein. The observed shifts are quantified in units of channels or least-significant-bit

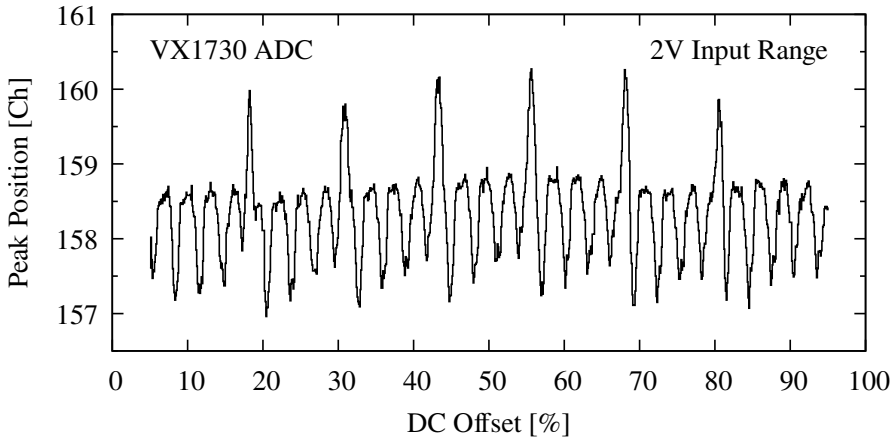

Figure 51: VX1730 digitizer ADC linearity scan as described in Ref. [91]. A maximum deviation of 3 LSB is observed. For further details see text.

(LSB) and reached up to 10 LSB in the DGF-4C modules [91]. Depending on the chosen input range in V, this corresponds to a certain energy shift in keV. For experiments with an expected maximum γ-ray energy of 12 MeV, the input range is typically set to approx. 16 MeV, accounting for enough overhead. Both the XIA and CAEN firmwares store energies as 14 bit integer values, which means that the maximum energy would correspond to $2^{14}\,\mathrm{Ch} = 16\,384\,\mathrm{Ch}$. In this scenario, one LSB would correspond to approx. 1 keV and a shift of 10 LSB would cause an energy shift of 10 keV in the final spectra.

Figure 51 presents DNL calibration results for the VX1730 ADC. The input range was set to 2 V and artificial pulses of approx. 20 mV pulse height were used to measure ADC linearity depending on the added DC offset between 0–100 % of 2 V. As can be seen, several shifts of up to 3 LSB occurr, together with dozens of smaller deviations of approx. 1.5 LSB in between. This behavior was found consistently throughout all tested digitizer input channels. While the maximum shift of 3 LSB is an improvement over the values obtained for the DGF-4C ADCs, it would still cause peak distortion at high energy ranges. Since the input range is not fine-adjustable, the 2 V range would have to be used for any experiment with expected γ-ray energies above 6–8 MeV, depending on the HPGe detector gain, representing an input range of approx. 20–25 MeV. Thus, a shift of 3 LSB would cause an energy shift of $25\,\mathrm{MeV}/2^{14} \cdot 3 = 4.5\,\mathrm{keV}$. As a result, NuDAQ uses the VX1730 for all preamplifier signals except HPGe detectors, as an optimum energy resolution is of prime interest there.

Since the VX1730 offers little flexibility and sub-optimal resolution for HPGe detectors, a request to the manufacturer CAEN S.p.A. was made within the scope of this thesis to combine features from two different digitizer modules and develop a module per-

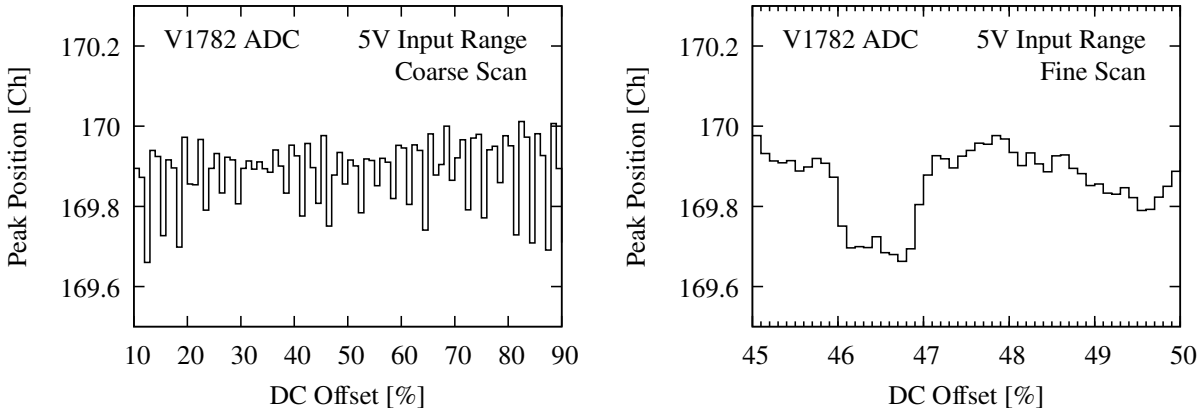

Figure 52: V1782 digitizer ADC linearity scan in coarse (*left panel*) and fine (*right panel*) steps, as described in Ref. [91]. A maximum deviation of only 0.3 LSB is found. For further details see text.

fectly suited for flexible high-resolution γ-ray spectroscopy. The desired module should combine the highly linear ADC used in the CAEN V1724 14 bit@100 MHz VME-format digitizer with the flexible input ranges available in the CAEN N6781 NIM-format Multi-Channel-Analyzer. Both modules have been tested within this thesis and the combination of their features was enticing. A prototype was delivered and tested in April 2019 and the first two V1782 production modules arrived in January 2020. The intended 14 bit ADC of the prototype was replaced by a 16 bit ADC, promising an even higher degree of linearity.

The DNL calibration procedure was also performed with a V1782 digitizer and results are shown in Fig. 52. Since the new module was not fully supported by automatic test scripts in the beginning, the DC offset scan was done by hand in coarse and fine steps. The results show a maximum shift of only 0.3 LSB at the highest possible input range of 5 V, which was consistently observed in all tested digitizer channels. At realistic experimental conditions, an input range of, e.g., 1.25 V would be chosen, for a dynamic range of approx. 12.5 MeV. The low DNL value of 0.3 LSB then corresponds to an energy shift of approx. 0.2 keV, which is negligible for such high range scenarios. In Doppler-Shift-Attenuation experiments, the dynamic range is typically set lower, and the effect of DNL is below 0.1 keV, owing to the high linearity of the employed ADC.

Energy Resolution Tests

The effect of DNL on energy resolution in γ-ray spectroscopy measurements is depicted in Figures 53 and 54 for the XIA DGF-4C modules and the CAEN V1782 digitizers, respectively. Several HPGe energy spectra were taken with both systems and a standard ^{226}Ra calibration source at count rates between 2–85 kcps. For each count rate, spectra were taken with three different input ranges, corresponding to typical applications. In each case, resolution in terms of the full width at half maximum (FWHM) and shape of the 609 keV peak were investigated.

The measurement shows that satisfying resolution can be obtained with the DGF-4C modules at the smallest dynamic range of $E_{max} = 4.5$ MeV. Here, the DNL shift still amounts to up to 10 LSB, but corresponds to very low energy shifts in terms of keV. As can be expected for any acquisition system, FWHM increases with increasing count rates. For the other two dynamic ranges, however, peak distortion occurs already at $E_{max} = 13$ MeV and 11 kcps and is severe at all count rates with $E_{max} = 26$ MeV.

The V1782 digitizer exceeds this performance by far and produces symmetric Gaussian peak shapes at all energy ranges and count rates. In a resolution sensitive scenario,

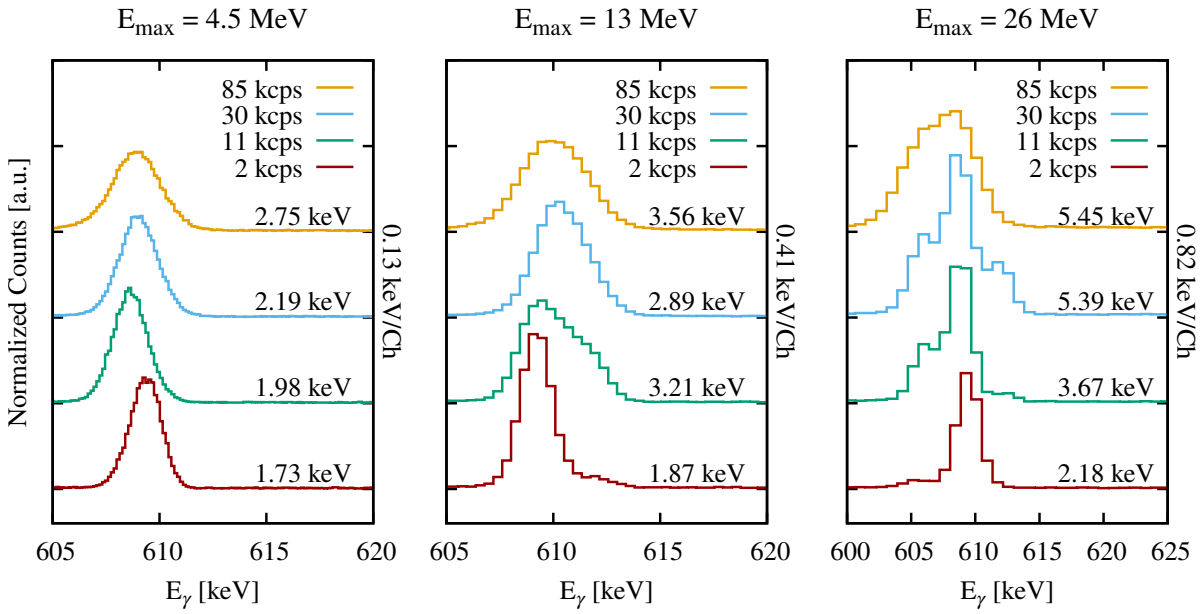

Figure 53: XIA DGF-4C Rev. F energy resolution scan. The 609 keV peak of ^{226}Ra was investigated at different count rates and dynamic ranges. Spectra have been shifted and normalized in height for visualization and FHWM is given for each peak. Overall deterioration of FWHM is observed with increasing count rate, as expected. Peak distortion sets in already at a dynamic range of $E_{max} = 13$ MeV and is most pronounced at $E_{max} = 26$ MeV

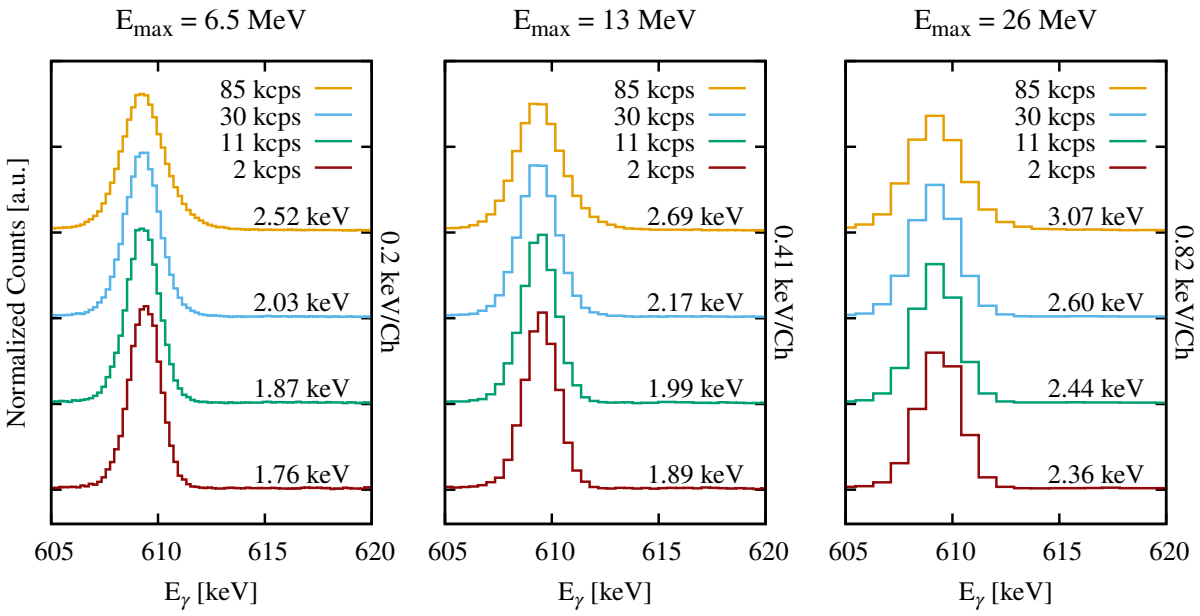

Figure 54: CAEN V1782 energy resolution scan. The 609 keV peak of ^{226}Ra was investigated at different count rates and dynamic ranges. Spectra have been shifted and normalized in height for visualization and FWHM is given for each peak. Strikingly, a symmetric Gaussian peak shape is preserved even at $E_{max} = 26$ MeV. An expected increase of FWHM with increasing count rate is observed, but resolution remains satisfactory even at the highest count rate of 85 kcps.

where lower count rates and low dynamic ranges are typically employed, the FWHM is equal to the reference value obtainable with analog electronics, i.e., around 1.7 keV. However, even at unreasonably high rates of 85 kcps and $E_{max} = 26$ MeV, the FWHM of the symmetric peak is still only 3.07 keV.

It can be concluded that differential non-linearities are still measureable in the V1782 digitizer, but their effect is negligible for any practical application in the laboratory. The module enables truly high-resolution spectroscopy with HPGe detectors in combination with a high flexibility and modern technology standards.

6.6 Direct Veto Handling

Both DPP firmware versions allow to enable a *trigger validation window*, in which an incoming detector signal can be either vetoed or acknowledged. In the case of a HPGe detector which is shielded by a BGO detector, individual vetos can be handled by digitizers directly and the internal logic is set up in a way that incoming signals are dismissed when an active veto signal arrives during the validation window. Logic BGO veto signals are then fed to each digitizer directly via the LVDS front connector on the

corresponding signal lane. A schematic overview of signal timing is given in the left panel of Fig. 55. BGO detectors have a faster response time compared to HPGe detectors and the trigger validation window is opened only after the HPGe trigger has been released. Thus, BGO signals have to be delayed slightly in order to arrive inside the trigger validation window. The validation window length has to be set long enough to account for the time jitter between HPGe and BGO signals, which is in the order of 500 ns.

The right panel of Fig. 55 shows the inverted case, where the logic BGO signal is used to inhibit the trigger validation window, i.e., the trigger request within the V2495 logic module. Here, the veto signal has to be high on the rising edge of the trigger validation window and the veto length has to be set according to the time jitter between HPGe and BGO signals. This solution is discussed in more detail in the next section.

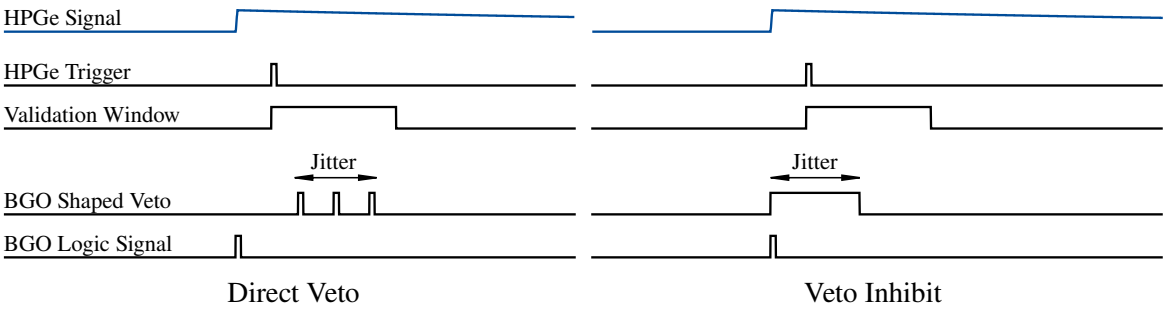

Figure 55: *Left*: Signal timing for direct vetoing. Trigger validation window is opened at the HPGe trigger release, during which incoming signals are dismissed when a rising edge of the BGO signal veto is detected on the corresponding LVDS input. Validation window length has to be set according to time jitter and logic BGO signals are delayed accordingly. *Right*: Timing for veto trigger-inhibition via the V2495 multiplicity filter. BGO logic signals are not delayed but have to be stretched according to time jitter. A high veto signal inhibits the trigger request inside the V2495 logic module, which is of equal length as the validation window.

Performance of the direct veto handling was tested with a BGO-shielded HPGe detector and a standard ^{137}Cs source, which emits γ-rays of only one energy at 661 keV. Spectra were taken for 60 s with and without active veto and the areas of full-energy-peak and Compton-continuum were integrated. Both spectra can be seen in Fig. 56. With correct timing settings, the FEP area is conserved, while the Compton-continuum is suppressed by over 50 %. Most of the remaining Compton-background is found around the Compton-edge, which represents a scattering of γ-rays around 180°. In this case, the scattered γ-ray does not pass the BGO shield and the event cannot be vetoed. The exact amount of suppression depends on the dimensions of both HPGe and BGO detector, but values of 50 % to 66 % are typical for the configurations used in-house.

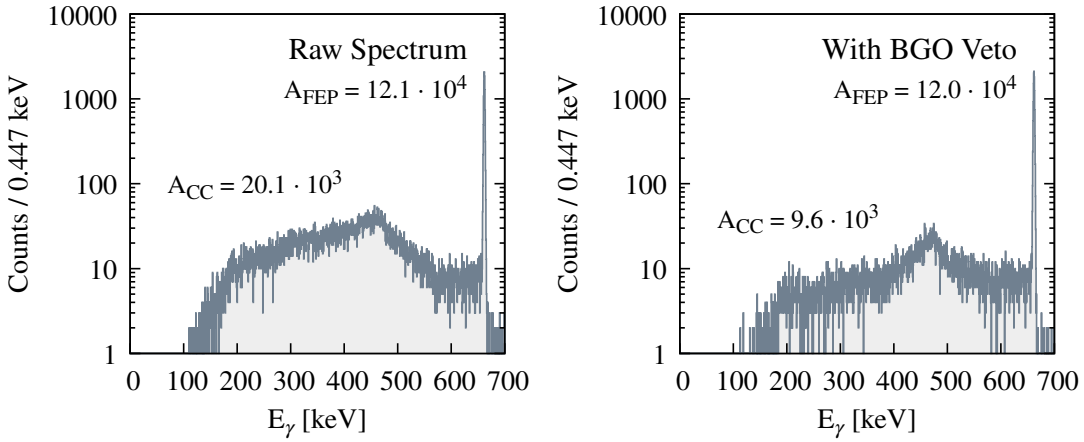

Figure 56: ^{137}Cs spectra taken for 60 s raw (*left panel*) and with direct BGO veto applied (*right panel*). Full-Energy-Peak (A_{FEP}) and the number of counts in the Compton-continuum (A_{CC}) are given in both cases. The FEP area is conserved and Compton-events are reduced by over 50 %. Mostly the Compton-edge remains in the right spectrum which cannot be vetoed by a surrounding BGO detector.

6.7 Implementation of a Combined Veto and Multiplicity Filter

With the number of detectors currently available, a large amount of data has to be read out and written to disk if data are taken without further trigger or coincidence condition. While the bare throughput was never a problem in the performed test experiments with NuDAQ, the large amount of disk space needed per experiment and the correspondingly long computation time in offline analysis induce unnecessary overhead for local IT infrastructure and scientific work. Typical data rates for triggerless experiments at the in-house laboratory with 10 to 20 detectors are in the order of 1 TB per week, depending on the exact experimental conditions. This amount can be drastically reduced for coincidence experiments by implementing an online trigger condition that allows data only to be transferred to the acquisition server when, e.g., at least two detectors triggered within a certain time window. The XIA system allowed such a multiplicity condition via the so-called *mult-out* signal, which emitted a logic signal of approx. 35 mV height and configurable length whenever a channel triggered. These signals were added electronically and a simple threshold condition could be used to detect when at least two detectors triggered, i.e., when the summed *mult-out* signal was above approx. 70 mV. A detailed explanation of this procedure is given in Refs. [84, 161].

A special firmware was developed for the V2495 logic module within this thesis, which handles trigger requests sent out by each digitizer channel, determines the current multiplicity level, and emits trigger acknowledgement signals on the corresponding output, when the desired multiplicity is reached [162]. For this application, digitizer firmwares

have to be configured to emit the trigger request signal on the front LVDS port, which is equal to the trigger validation window explained earlier and functions as an online coincidence window. Hits are only accepted if a trigger acknowledgement signal is returned on the corresponding LVDS input within the trigger validation window. In this case, the digitizer trigger logic is inverted compared to the direct veto implementation presented earlier. The specific digitizer firmware settings can be found in Refs. [163–165] and a sketch of the necessary cable connections is shown in Appendix C.2.

Since all LVDS signal lanes of a digitizer are used for trigger communication, BGO vetos have to be applied elsewhere and the V2495 handles them by inhibiting trigger request signals as shown in the right panel of Fig. 55. In the developed firmware, trigger request signals are sampled at each FPGA clock cycle, i.e., every 20 ns, and their state is forwarded to the internal multiplicity evaluation stage. If a trigger request signal arrives and the corresponding veto signal is high on the rising edge of the request signal, it is

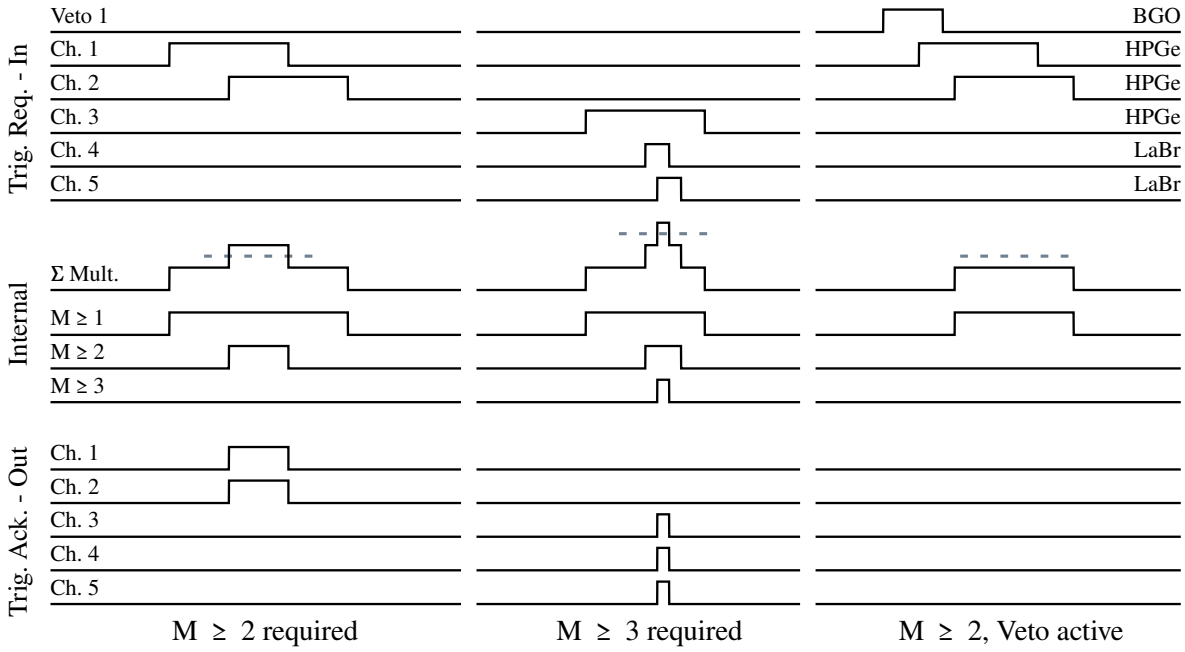

Figure 57: Exemplary cases explaining the evaluation of multiplicity in the V2495 firmware. Trigger request inputs are shown on top, internal logic in the middle and outgoing trigger acknowledgements on the bottom. Veto 1 corresponds to a BGO detector shielding the HPGe detector on Ch 1. *Left*: Two HPGe trigger requests overlap and $\mathrm{M} \geq 2$ is detected when summed multiplicity Σ Mult. exceeds threshold (dashed line). *Center*: HPGe-LaBr-LaBr triple coincidence. Validation windows for LaBr detectors are set shorter due to faster response time. *Right*: BGO veto signal inhibts HPGe trigger request and required multiplicity is not achieved. None of the requests are acknowledged.

prevented from contributing to the multiplicity evaluation. Thus, the trigger request is inhibited in the V2495. While similar to a direct veto, it requires that veto signals arrive early enough and cover the rising edge of trigger requests. The additional sampling and inhibition stage introduces a delay of two clock cycles or 40 ns. However, this delay is negligible for typical coincidence window lengths of 1 µs in experiments using HPGe detectors.

Three exemplary cases are depicted in Fig. 57, which explain how the multiplicity condition is evaluated in the V2495 firmware and when trigger acknowledgement signals are emitted. In the left panel, two HPGe trigger requests arrive at different times, but their request signals overlap partially. The summed multiplicity value $\Sigma\,\mathrm{Mult.}$ exceeds the required level of $\mathrm{M} \geq 2$ as soon as the second request arrives, and corresponding trigger acknowledgement signals are emitted as long as the condition is valid. The center panel shows an example for HPGe-LaBr-LaBr triple-coincidence measurements. Due to the faster response of LaBr detectors, their trigger validation windows can be set shorter and a corresponding triple coincidence is detected as all three trigger requests overlap. Again, trigger acknowledgements are emitted as long as the required $\mathrm{M} \geq 3$ condition is valid. Lastly, the right panel shows the case of a veto signal present for one HPGe detector and a required multiplicity of $\mathrm{M} \geq 2$. Since the veto signal covers the rising edge of the first HPGe trigger request, it is inhibited and does not contribute to the multiplicity condition. In this case no trigger acknowledgements are emitted and no hits are stored. Under any circumstance, trigger acknowledgement signals are only emitted to channels which have a valid trigger request state, i.e., it is neither zero nor inhibited. This ensures only relevant and valid hits are being stored. Should, however, a third trigger request arrive while two signals are already overlapping and $\mathrm{M} \geq 2$ is required, it will receive a trigger acknowledgement, albeit slightly later than the others. Thus, no possible coincidences are omitted and the information in the background window is conserved in the offline analysis.

The V2495 firmware is configured via USB and all input and output banks can be activated or deactivated. Additionally, the rates of all trigger inputs, veto inputs, trigger outputs, and the overall multiplicity rate are reported via USB. The latter can be a useful tool for monitoring an experiment. A multiplicity trigger signal is emitted on a front LEMO connector of the V2495, which allows to monitor the evaluated multiplicity rate on an oscilloscope. For ease of operation, a multiplicity of $\mathrm{M} \geq 1$ can be set, which makes the system acquire data triggerless while still handling veto signals in the V2945.

The effect of applying an online $\mathrm{M} \geq 2$ coincidence condition is depicted in Fig. 58. A measurement was performed with the HORUS spectrometer containing 14 HPGe detec-

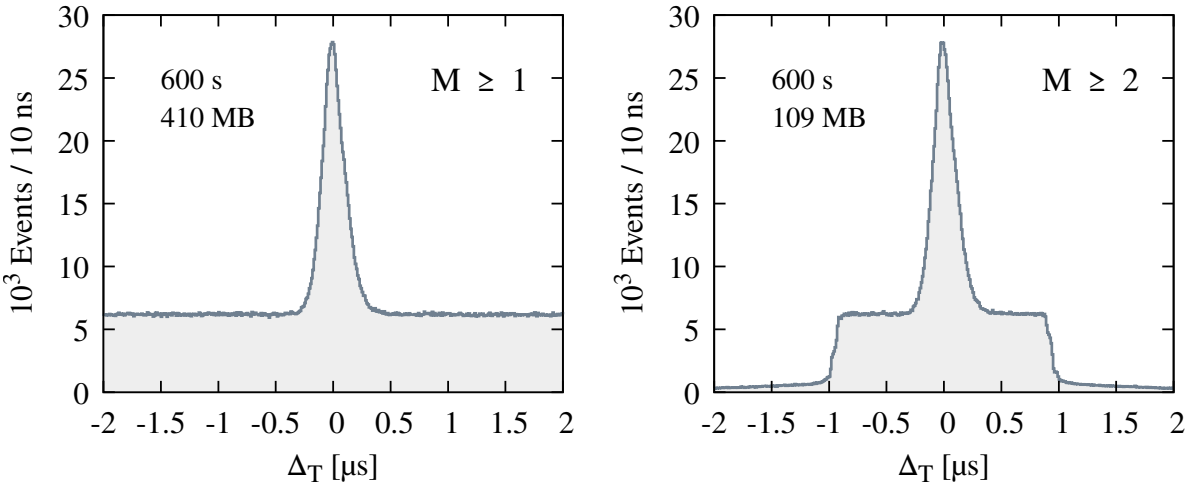

Figure 58: Time-difference spectra between two HPGe hits and data reduction via the V2495 multiplicity filter. *Left*: Size of singles data taken with a ^{226}Ra source and 14 HPGe detectors over 600 s is 410 MB. The prompt peak contains $5.14 \cdot 10^5$ $\mathrm{M} = 2$ events. *Right*: With a coincidence window of 1 µs and $\mathrm{M} \geq 2$ selected, file size is reduced to 109 MB while the number of prompt coincidences is conserved. Note how the flat background of random coincidences steeply drops after ±1 µs.

tors and a ^{226}Ra γ-ray source. Data were taken for 600 s with the multiplicity condition set to $\mathrm{M} \geq 1$ and $\mathrm{M} \geq 2$, respectively, and the trigger validation window was set to 1 µs. The time difference spectra between any combination of two HPGe detectors show the expected *prompt* peak on top of a flat *random* background. In the $\mathrm{M} \geq 1$ case 410 MB of data were recorded containing $5.14 \cdot 10^5$ $\mathrm{M} = 2$ coincidence events. By applying the $\mathrm{M} \geq 2$ condition, only 109 MB of disk space were used which contained the same amount of $\mathrm{M} = 2$ coincidences. The filtered time spectrum still contains enough background for an offline subtraction of random coincidences in the prompt window, but 74 % of disk space was saved. In a real experiment, this data reduction will depend heavily on the number of used detectors, employed online multiplicity requirement, and the multiplicity of particles and γ-rays being emitted from the nuclear reaction of interest.

For experiments which solely investigate coincidence events, the online data reduction is easy to set up and saves a considerable amount of storage space and analysis time. However, it can be useful to have several detectors acquire data triggerless for normalization purposes. In this case, the both DPP firmware versions can be configured to emit the trigger validation window signal, but not require an acknowledgement signal. By setting several detector channels accordingly, absolute experimental values, such as cross sections, can be obtained by normalizing to these triggerless detectors, while their

multiplicity information is still used for all other detector channels which require trigger acknowledgement.

6.8 Dead Time Estimation

The term dead time is often used in slightly different ways, but generally indicates the fact that an acquisition system, including detectors, cannot process signals infinitely fast and absolute measurement times or peak areas have to be corrected for this dead time. While it may not be determinable in units of time directly, it can be extracted from statistics information with digital acquisition systems and is usually expressed in terms of percentage. The CAEN CoMPASS acquisition software determines dead times per detector for both DPP firmware versions and stores them in dedicated files after a measurement has been stopped. It takes into account the number of events written to file N_{Out} and events flagged as pile-up N_{PileUp}, and even estimates the number of events not distinguished by the trigger filter $N_{Poisson}$ and events missed due to ADC saturation $N_{Sat.}$. The latter two are iteratively calculated assuming a Poisson distribution of such events within the trigger filter time or the time above ADC saturation. A detailed explanation of dead time estimation with CoMPASS can be found in Ref. [160]. Finally, the number of input events N_{In} and a dead time τ_{dead} is determined per detector via the following relation:

$$\begin{aligned} N_{In} &= N_{Out} + N_{Sat.} + N_{PileUp} + N_{Poisson} \\ \tau_{\mathrm{dead}} &= 1 - \frac{N_{Out}}{N_{In}} \end{aligned} \tag{6.1}$$

While the approaches implemented in CoMPASS are helpful and yield precise estimates, e.g., for simple γ-ray spectroscopy, the consulted statistical information are incorrect when BGO vetos are applied. In this case, additional hits are dismissed and the number of events written to file N_{Out} is lowered, though the investigated FEP areas are conserved. Thus, a HPGe signal being vetoed by BGO should not be treated as dead time since the system was able to properly process the HPGe signal and doing so results in an underestimation of τ_{dead}. To circumvent this issue, a simple estimation can be performed based on additional flags and meta events present in the raw data stored to file. Besides valid hits, the raw data contain flags which report the number of triggers counted in a given channel before validation, as well as all events flagged as pile-up or saturation events. By counting these flags and events in the offline analysis, values can be obtained for the true number of input events N_{Trig}^{RAW} and the number of valid hits stored in spectra N_{Out}^{RAW}. Assuming the per-channel dead time is dominantly generated

by pile-up effects, and no signal distortion or frequent long-term saturation occurs, τ_{dead} can simply be determined via

$$\tau_{\mathrm{dead}} = 1 - \frac{N_{Out}^{RAW}}{N_{Trig}^{RAW}} \tag{6.2}$$

Note that the Poisson-like estimation of missed triggers during saturation or within the $\mathrm{RC} - \mathrm{CR}^2$ filter time is not applied in this case, but can be implemented in the future.

Attention is needed when employing both BGO vetos and an online multiplicity condition via the V2495 module. In this case, the counted numbers of events are not only affected by statistical or rate dependent terms, but by the angular correlation between particles and γ-rays emitted from target position. A dead time correction using Eq. 6.2 can be performed, but angular correlations cannot be taken into account and the determined physics values may be falsely distorted to isotropy. Further development is needed for this application and the detailed information available in the raw data files should be exploited for this purpose.

6.9 Data Throughput

The fast connection between acquisition server and digitizers via fibre channel is complemented by an onboard ring buffer, which allows signals to be processed continuously while stored data are continuously being read out and no global dead time occurs. This feature is a major improvement over the DGF-4C modules, which could only be read out sequentially and were forced to do so as soon as one of the modules reported a full buffer. The advantage of the CAEN system over its predecessor was quantified in an in-

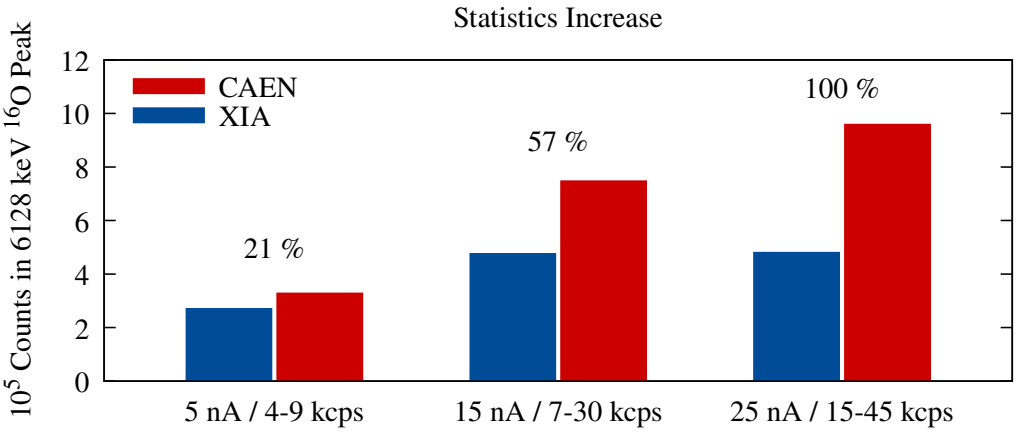

Figure 59: Data throughput with XIA and CAEN systems at three different beam currents and corresponding count rates. As measure for statistics increase, the 6128 keV peak area stemming from ^{16}O is investigated. The relative increase gained by the CAEN system is given in percent for each case.

beam measurement with the HORUS spectrometer equipped with 14 HPGe detectors. A 10 MeV proton beam impinged on a Mylar+Au target in order to produce γ radiation and high count rates per detector depending on the ion beam current. Data were taken for 20 min with both systems simultaneously at three different beam currents of 5 nA, 15 nA, and 25 nA. As a measure for the statistics increase, the area under the 6128 keV peak stemming from ^{16}O in the summed HPGe spectra was investigated. Figure 59 shows the integrated areas determined with both systems at three beam current settings and gives the range of detector count rates observed in each case. The statistics increase gained by the new system is given in percent. As can be seen, the CAEN system gains 21 % of statistics even at moderate count rates, i.e., at 5 nA in the test experiment. Since read-out related dead time increases with higher currents, a drastic improvement of 100 % is found at 25 nA and rates between 15–45 kcps. The effect of read-out induced dead time in the XIA system will increase even further with a higher number of detector channels, e.g., when using a combined setup such as SONIC@HORUS. Therefore, it can be concluded that for current experiments with a number of detectors around 20–30, the NuDAQ system enables to record at least twice as much statistics per day of beam time compared to the predecessor system, even at medium count rates. As a consequence, the necessary number of days per experiment can be reduced by a factor of two and more systematic investigations of different target materials or beam energies are possible. Alternatively, much higher statistics can be gained in conventional measurement times.

6.10 Summary and Outlook

The NuDAQ acquisition system for nuclear-physics experiments at the 10 MV accelerator laboratory of the University of Cologne was designed, tested, and commissioned within this thesis. High flexibility and compatibility to all common types of experiments performed in-house were desired from the beginning. Several CAEN VX1730 digitizers were already available at UoC and the specialized V1782 digitizers were developed by CAEN recently based on the demands which arose throughout this thesis. The fast VX1730 modules are well suited for applications where a large number of channels have to be processed or where precise digital timing is needed. Complementary, the V1782 modules provide excellent resolution and linearity for high-resolution γ-ray spectroscopy with HPGe detectors. The highly flexible system offers a wide range of maximum energies or pulse heights and allows various types of detector signals to be sampled and analyzed. In combination with the centralized acquisition architecture and CoMPASS control software, the system satisfies all current needs in the laboratory and has enough headroom for future upgrades.

ADC linearity of both digitizer types was investigated via an established procedure using small artificial pulses. The 16 bit ADC implemented in the V1782 modules exhibited a differential non-linearity of only 0.3 LSB, which is about a factor 30 lower compared to the previous system. Realistic resolution tests were performed with a standard ^{226}Ra γ-ray source at different count rates and dynamic ranges. Under all conditions, the achieved energy resolution of the V1782 outperformed the predecessor DGF-4C modules and a symmetric peak shape was maintained. Overall data throughput and correlated dead time was investigated in an ion beam experiment, using 14 HPGe detectors. At realistically high count rates, the NuDAQ system detected 100 % more valid hits than the XIA system. This effect is expected to be even more pronounced with a higher number of detectors, e.g., when using the combined particle and γ-ray spectrometers SONIC@HORUS. As a result, the new system enables much higher statistics per hour of beam time and to perform systematic studies on various reactions on conventional time scales with comparable statistics.

A dedicated firmware was developed for the V2495 FPGA logic module within this thesis. It offers a combined online veto and multiplicity filter for up to 64 detectors. The achieved data reduction saves storage space and makes offline analysis considerably less time consuming. In addition, the logic module can be used to monitor trigger, veto, and coincidence rates of each detector via a USB connection. Performance of BGO vetoing was tested with a ^{137}Cs γ-ray source and showed the expected reduction of Compton-scattering events of approx. 50–66 %.

Especially interesting for direct timing of fast signals, e.g., in *fast-timing* experiments, is the digital CFD implemented in the DPP-PSD firmware available for the VX1730 digitizers. However, its effective time resolution is still under investigation [150].

During commissioning, an error in the V1782 DPP-PHA firmware was found, which caused timestamps to jump by exactly 2^{30} clock cycles, approx. 10.7 s, to higher or lower values. Fortunately, the issue can easily be identified in the raw data and an offline correction for it was integrated into both available event-building softwares. At the time of writing this thesis, the issue was solved by manufacturer CAEN in an unofficial firmware release and no such jumps were observed in corresponding tests.

A recent update of the CoMPASS control software allows remote control of the acquisition system via user-writable software. With this feature, specialized applications can be developed in the future to tailor the experimental workflow to scientific needs and conventions. Also, exploiting the remote controlled start, stop, and readout of an acquisition run would allow to couple NuDAQ to the automatic measurement software developed recently for the AMS beamline at the 10 MV FN-Tandem system [166].

A Appendix A

A.1 CAGRA+GR Data Acquisition Flow Chart

The following flow chart describes the signal paths and triggering logic of the GR and CAGRA spectrometers. The red dashed lines indicate detector signal connections and blue arrows show the direction of trigger signals. A coincidence between Plastic 1 and Plastic 2 is used to generate a trigger for both GR and CAGRA. Figure taken from Ref. [53].

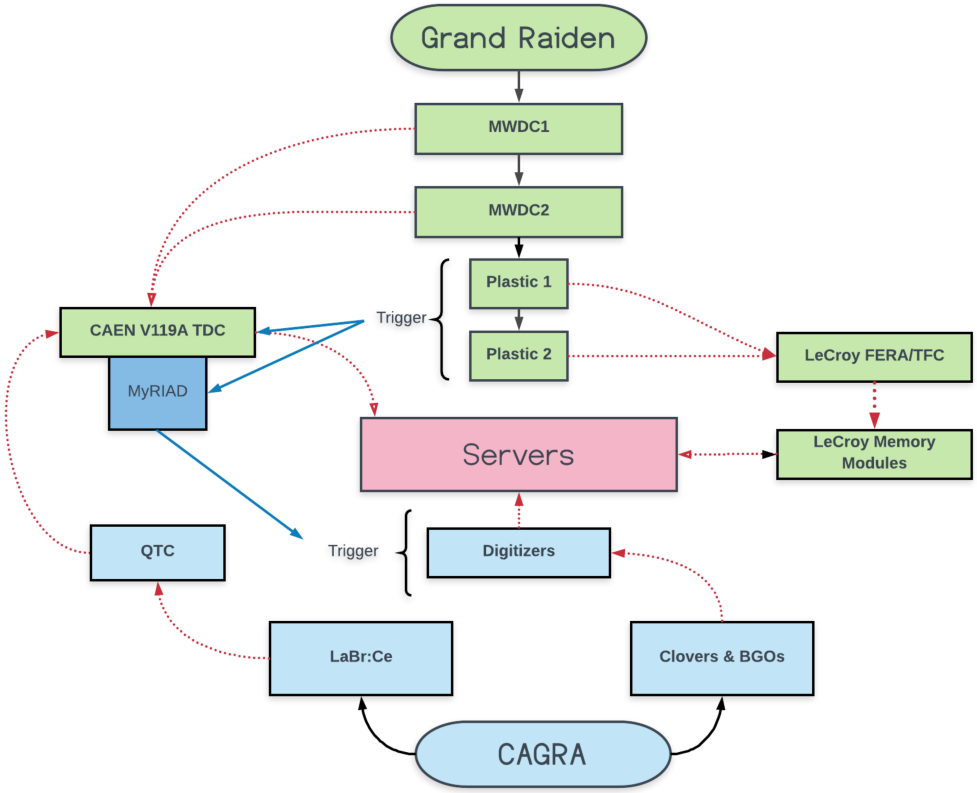

A.2 Sieve-Slit Correction Parameters

The sieve-slit correction presented in Chapter 2.2.3 was performed using the polynomial correction given in Eq. 2.4. The following table lists the determined correction parameters. Note that Θ_{tgt} was shifted by the central spectrometer angle $\Theta_{\mathrm{GR}} = 4.5°$ for the minimization procedure, i.e., $\Delta\Theta_{tgt}$ was used instead.

$$
\begin{array}{lll}
p^{00} = -0.715113188 & p^{10} = 0.304190803 & p^{20} = -0.0202445228 \\
p^{01} = 0.178417640 & p^{11} = -0.226468753 & p^{21} = 0.110116166 \\
p^{02} = -0.000541271096 & p^{12} = 0.00231584969 & p^{22} = -0.00179646628
\end{array}
$$

A.3 $\mathrm{X}(\Theta_{tgt})$ Correction Parameters

The correction of X position depending on Θ_{tgt} presented in Chapter 2.2.4 was performed using the polynomial correction given in Eq. 2.6. The following table lists the determined correction parameters. Note that Θ_{tgt} was shifted by the central spectrometer angle $\Theta_{\mathrm{GR}} = 4.5°$ for the minimization procedure, i.e., $\Delta\Theta_{tgt}$ was used instead.

$$
\begin{array}{ll}
p^{00} = -0.770448688 & p^{10} = 0.998662006 \\
p^{01} = 2.18301802 & p^{11} = -0.00206344186 \\
p^{02} = 9.96759517 & p^{12} = 0.0122513493 \\
p^{03} = -3.87819139 & p^{13} = -0.00497831199 \\
 & \\
p^{20} = -5.53532604 \cdot 10^{-7} & p^{30} = -4.40326541 \cdot 10^{-10} \\
p^{21} = -2.56365501 \cdot 10^{-5} & p^{31} = -1.47138637 \cdot 10^{-8} \\
p^{22} = 1.99378382 \cdot 10^{-5} & p^{32} = 7.70526229 \cdot 10^{-9} \\
p^{23} = 1.35059879 \cdot 10^{-6} & p^{33} = -3.25745839 \cdot 10^{-8}
\end{array}
$$

A.4 CAGRA Detector Positions

CAGRA positions of HPGe clover leafs

Det.	Θ_γ	Φ_γ	Det.	Θ_γ	Φ_γ	Det.	Θ_γ	Φ_γ
5A	96°	73.2°	9A	84°	−106.7°	13A	140°	54.0°
5B	84°	73.2°	9B	96°	−106.7°	13B	129°	52.3°
5C	84°	61.7°	9C	96°	−118.2°	13C	129°	37.6°
5D	96°	61.7°	9D	84°	−118.2°	13D	140°	35.9°
6A	96°	28.2°	10A	84°	−151.7°	14A	140°	−35.9°
6B	84°	28.2°	10B	96°	−151.7°	14B	129°	−37.6°
6C	84°	16.7°	10C	96°	−163.2°	14C	129°	−52.3°
6D	96°	16.7°	10D	84°	−163.2°	14D	140°	−54.0°
7A	96°	−16.7°	11A	84°	163.2°	15A	140°	−125.7°
7B	84°	−16.7°	11B	96°	163.2°	15B	129°	−127.4°
7C	84°	−28.2°	11C	96°	151.7°	15C	129°	−142.5°
7D	96°	−28.2°	11D	84°	151.7°	15D	140°	−144.2°
8A	96°	−61.7°	12A	84°	118.2°	16A	140°	144.2°
8B	84°	−61.7°	12B	96°	118.2°	16B	129°	142.5°
8C	84°	−73.2°	12C	96°	106.7°	16C	129°	127.4°
8D	96°	−73.2°	12D	84°	106.7°	16D	140°	125.7°

CAGRA positions of LaBr detectors

Det.	Θ_γ	Φ_γ
1	45°	45°
2	45°	−45°
3	45°	−135°
4	45°	135°

A.5 CAGRA+GR Experimental γ-ray Angular Distributions

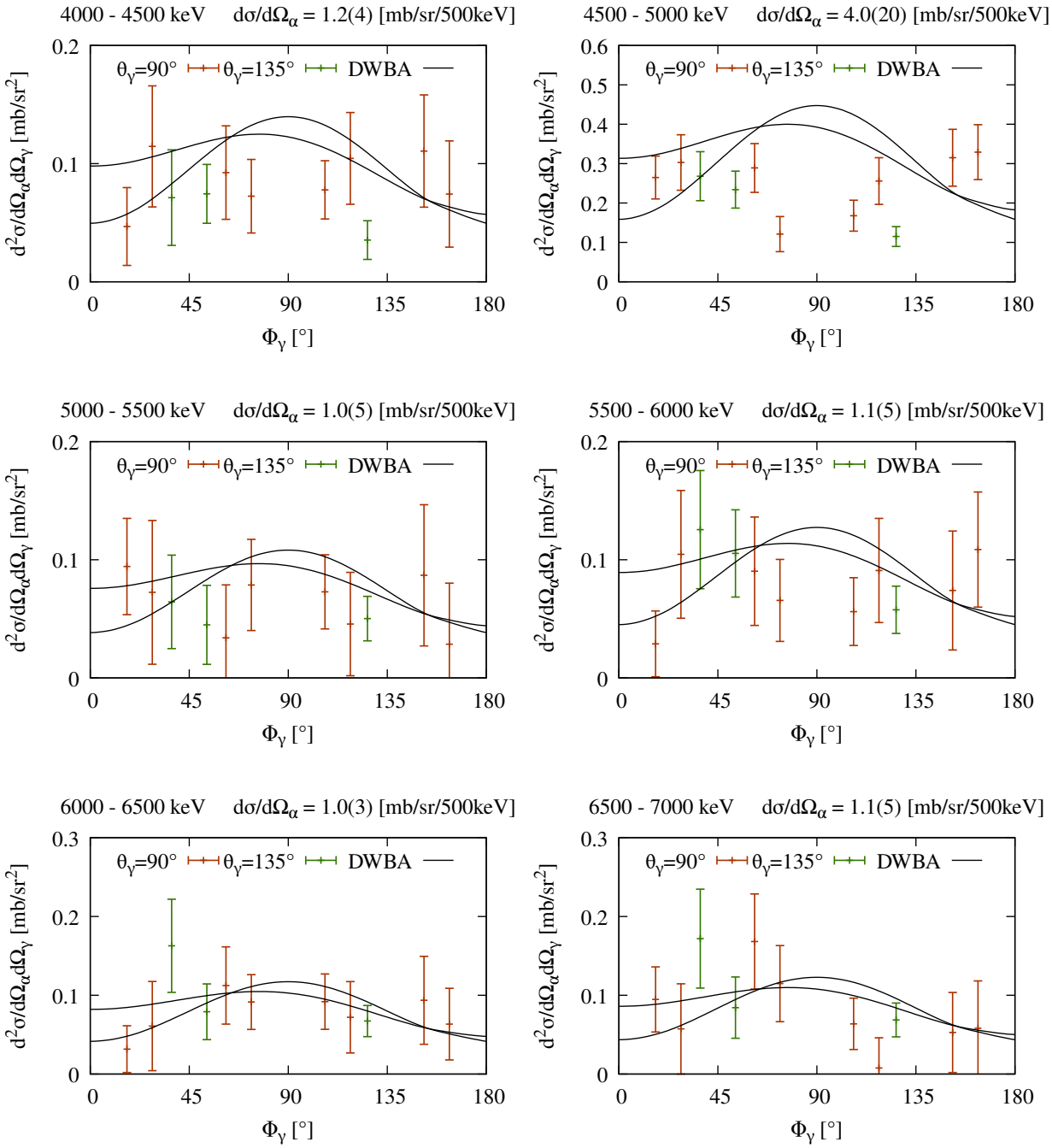

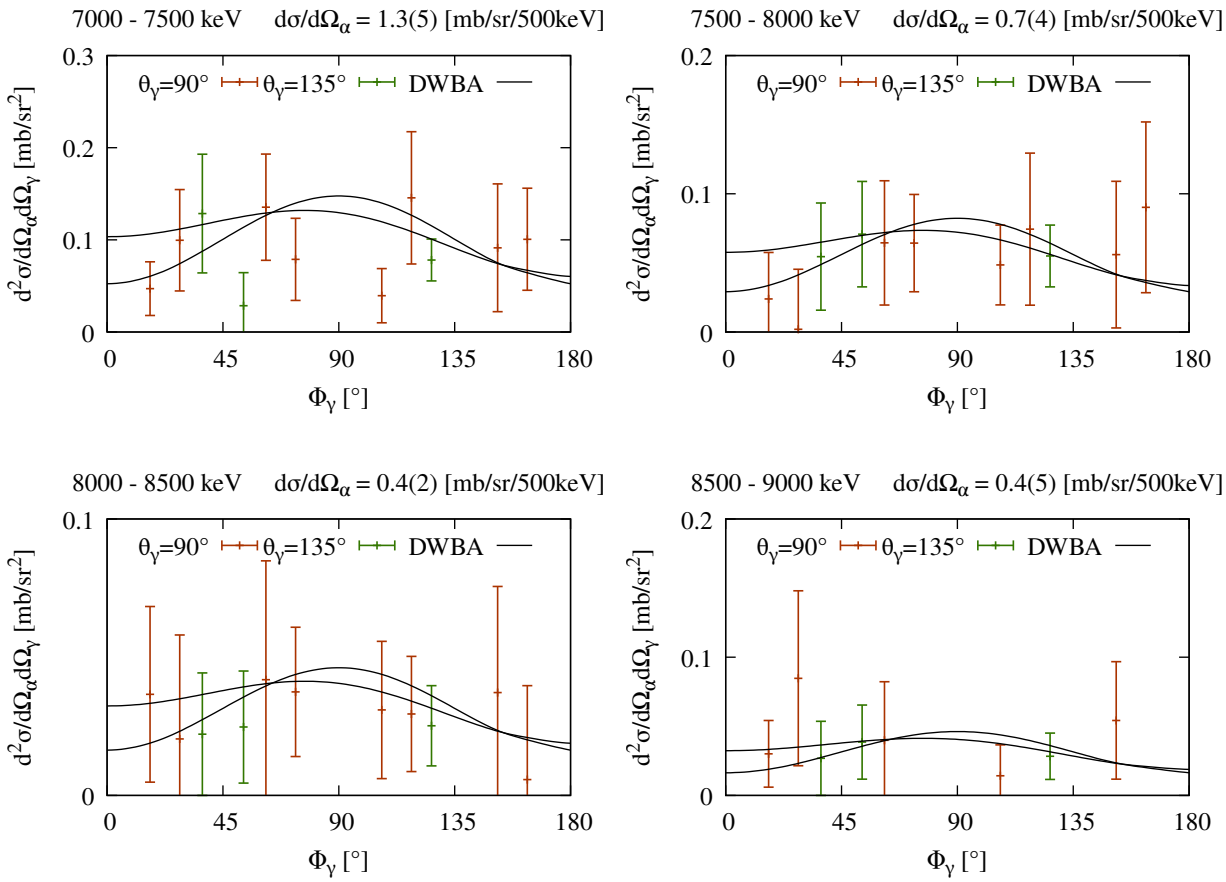

Figure 61: ^{120}Sn$(\alpha, \alpha'\gamma)$ Experimental γ-ray angular distributions for ground-state decays between 4–9 MeV in bins of 500 keV with the expected DWBA distribution for $E1$ decay.

A.6 ^{120}Sn$(\alpha, \alpha'\gamma)$ Differential Cross Sections in 500 keV wide bins

^{120}Sn$(\alpha, \alpha'\gamma)$ integrated ground-state decay cross sections in 500 keV bins between 5 MeV and 9 MeV. Error bars indicate statistical errors only.

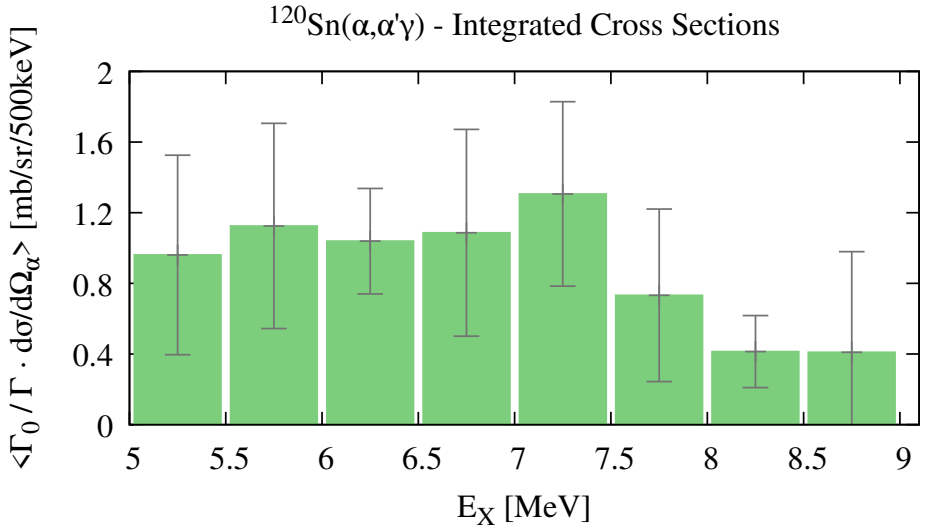

B Appendix B

B.1 Derivation of Doppler-angle θ_D and tilt-angle ϕ_t

Based on the derivation for $(p, p'\gamma)$ reactions found in the appendix of Ref. [84], the derivation is given here for the Doppler-angle θ_D between recoiling nucleus and emitted γ-ray, as well as the tilt angle ϕ_t between the *reaction plane* and the *emission plane* spanned by the direction of the recoiling nucleus and the emitted γ-ray.

Since SONIC data are usually calibrated to excitation energy instead of proton energy, the available information are the excitation energy E_X and the directions of both the ejectile (Θ_e, Φ_e) and the emitted γ-ray $(\Theta_\gamma, \Phi_\gamma)$ in the HORUS coordinate system. The Doppler-shift of a γ-ray with the initial center-of-mass energy E_γ^0 is given based on the Doppler-angle θ_D and the velocity of the recoiling nucleus $\mathrm{v_R}$ as

$$\mathrm{E}_\gamma(\theta_D) = \mathrm{E}_\gamma^0 \left(1 + F(\tau) \cdot \frac{\mathrm{v}_R}{c} \cdot \cos\theta_D\right), \tag{B.1}$$

where c is the speed of light in vacuum and $F(\tau)$ represents the livetime of the excited state and is usually assumed to be 1 for high-lying $J^\pi = 1^-$ states. In an experiment, the shifted energy $\mathrm{E}_\gamma(\theta_D)$ is detectd and the initial, unshifted energy can be determined via

$$\mathrm{E}_\gamma^0 = \frac{\mathrm{E}_\gamma(\theta_D)}{\left(1 + F(\tau) \cdot \frac{\mathrm{v}_R}{c} \cdot \cos\theta_D\right)}, \tag{B.2}$$

where expressions for v_R and $\cos\theta_D$ are needed.

Derivation of the Doppler-angle θ_D

For the general case of a reaction that can be measured with SONIC@HORUS, the projectile and ejectile do not have to be equal. Following energy and momentum conservation, we get

$$\begin{aligned} \mathrm{E}_B + Q &= \mathrm{E}_e + \mathrm{E}_R + \mathrm{E}_X \\ |\vec{P}_B| &= |\vec{P}_e| \cdot \cos\Theta_e + |\vec{P}_R| \cdot \cos\Theta_R \\ 0 &= |\vec{P}_e| \cdot \sin\Theta_e + |\vec{P}_R| \cdot \sin\Theta_R \end{aligned} \tag{B.3}$$

with beam, ejectile, and recoil energies $\mathrm{E}_B, \mathrm{E}_e, \mathrm{E}_R$, reaction Q value, the momentum of the beam projectile, ejectile, and recoil $\vec{P}_B, \vec{P}_e, \vec{P}_R$, and the polar angle of ejectile and recoil in the HORUS coordinate system Θ_e, Θ_R. Combining both momentum equations,

we get

$$\tan\Theta_R = \frac{|\vec{P}_e| \cdot \sin\Theta_e}{|\vec{P}_B| - |\vec{P}_e| \cdot \cos\Theta_e} \tag{B.4}$$

Using $|\vec{P}| = \sqrt{2m\mathrm{E}}$ and rearranging, the polar recoil angle can be expressed as

$$\Theta_R = \arctan\left(\frac{\sin\Theta_e}{\sqrt{\frac{m_B\mathrm{E}_B}{m_e\mathrm{E}_e}} - \cos\Theta_e}\right) \tag{B.5}$$

with an expression for E_e still missing. We, again, rearrange eqs. B.3 to get

$$\mathrm{E}_B + Q - \mathrm{E}_X - \frac{|\vec{P}_e|^2}{2m_e} = \frac{|\vec{P}_R|^2}{2m_R} \tag{B.6}$$

and

$$|\vec{P}_B|^2 + |\vec{P}_e|^2 - 2|\vec{P}_B||\vec{P}_e| \cdot \cos\Theta_e = |\vec{P}_R|^2 \tag{B.7}$$

Combining eqs. B.6 and B.7, we get a quadratic equation for $|\vec{P}_e|$:

$$|\vec{P}_e|^2 \cdot (1 + \frac{m_R}{m_e}) - 2|\vec{P}_e||\vec{P}_B| \cdot \cos\Theta_e + \Big(|\vec{P}_B|^2 - 2m_R(\mathrm{E}_B + Q + \mathrm{E}_X)\Big) = 0 \tag{B.8}$$

which is gives the physical solution:

$$|\vec{P}_e| = \frac{|\vec{P}_B| \cdot \cos\Theta_e + \sqrt{|\vec{P}_B|^2\cos^2\Theta_e - (1+\frac{m_R}{m_e})(|\vec{P}_B|^2 - 2m_R(\mathrm{E}_B + Q - \mathrm{E}_X))}}{(1+\frac{m_R}{m_e})} \tag{B.9}$$

Since all residual masses and energies are known, we can now calculate:

$$\begin{aligned} \mathrm{E}_e &= \frac{|\vec{P}_e|^2}{2m_e} \\ \mathrm{E}_R &= \mathrm{E}_B + Q - \mathrm{E}_X - \mathrm{E}_e \\ |\vec{P}_R| &= \sqrt{2m_R\mathrm{E}_R} \\ v_R &= \frac{|\vec{P}_R|}{m_R} = \sqrt{\frac{2\mathrm{E}_R}{m_R}} \end{aligned} \tag{B.10}$$

Still missing is an expression for $\cos\theta_D$, the Doppler-angle spanned by the direction of the recoiling nucleus and the emitted γ-ray:

$$\cos\theta_D = (\vec{e}_R \cdot \vec{e}_\gamma) \tag{B.11}$$

The unit vectors within the HORUS coordinate system are defined as:

$$\vec{e}_\gamma = \begin{pmatrix} \sin\Theta_\gamma \ \cos\Phi_\gamma \\ \sin\Theta_\gamma \ \sin\Phi_\gamma \\ \cos\Theta_\gamma \end{pmatrix}, \ \vec{e}_R = \begin{pmatrix} \sin\Theta_R \ \cos\Phi_R \\ \sin\Theta_R \ \sin\Phi_R \\ \cos\Theta_R \end{pmatrix}, \ \vec{e}_e = \begin{pmatrix} \sin\Theta_e \ \cos\Phi_e \\ \sin\Theta_e \ \sin\Phi_e \\ \cos\Theta_e \end{pmatrix} \tag{B.12}$$

From momentum conservation within the reaction plane, it follows that $\Phi_R = \Phi_e + \pi$. Using Eq. B.5 to eliminate Θ_R and $\sin(\arctan(x)) = \frac{x}{\sqrt{1+x^2}}$ and $\cos(\arctan(x)) = \frac{1}{\sqrt{1+x^2}}$, we get

$$\cos\theta_D = \frac{1}{\sqrt{1+x^2}} \left[\cos\Theta_\gamma - x \cdot (\sin\Theta_\gamma \cos\Phi_\gamma \cos\Phi_e + \sin\Theta_\gamma \sin\Phi_\gamma \sin\Phi_e)\right] \tag{B.13}$$

with

$$x = \frac{\sin\Theta_e}{\sqrt{\frac{m_B \mathrm{E}_B}{m_e \mathrm{E}_e}} - \cos\Theta_e}. \tag{B.14}$$

Finally, after applying the trigonometric identities for $\cos\alpha \cdot \cos\beta$ and $\sin\alpha \cdot \sin\beta$, the angle used for the Doppler-correction can be expressed as

$$\cos\theta_D = \frac{1}{\sqrt{1+x^2}} \cdot (\cos\Theta_\gamma - x \cdot \sin\Theta_\gamma \cdot \cos(\Phi_\gamma - \Phi_e)) \tag{B.15}$$

Derivation of the tilt-angle ϕ_t

The *reaction plane* is spanned by the recoiling nucleus and the ejectile. Its normal vector is defined by:

$$\vec{n}_{Reac} = \vec{e}_R \times \vec{e}_e \tag{B.16}$$

The *emission plane* is spanned by the recoiling nucleus and the emitted γ-ray:

$$\vec{n}_E = \vec{e}_R \times \vec{e}_\gamma \tag{B.17}$$

ϕ_t is the angle between the *reaction plane* and the *emission plane* and is given by the scalar product of their normal vectors:

$$\cos\phi_t = \vec{n}_E \cdot \vec{n}_{Reac} = (\vec{e}_R \times \vec{e}_\gamma) \cdot (\vec{e}_R \times \vec{e}_e) \tag{B.18}$$

Using the *Lagrange identity* $(\vec{a} \times \vec{b}) \cdot (\vec{c} \times \vec{d}) = (\vec{a} \cdot \vec{c})(\vec{b} \cdot \vec{d}) - (\vec{b} \cdot \vec{c})(\vec{a} \cdot \vec{d})$ and the definition

of the γ-ray Doppler angle $\cos\theta_D = (\vec{e}_\gamma \cdot \vec{e}_R)$, Eq. B.18 can be expressed as:

$$\begin{aligned}\cos\phi_t &= (\vec{e}_R \cdot \vec{e}_R)(\vec{e}_\gamma \cdot \vec{e}_e) - (\vec{e}_\gamma \cdot \vec{e}_R)(\vec{e}_R \cdot \vec{e}_e) \\ &= (\vec{e}_\gamma \cdot \vec{e}_e) - \cos\theta_D \cdot (\vec{e}_R \cdot \vec{e}_e)\end{aligned} \tag{B.19}$$

After inserting the unit vector definitions, executing the scalar products, and rearranging, we get:

$$\begin{aligned}\cos\phi_t = \sin\Theta_e\cos\Phi_e\ &[\sin\Theta_\gamma\cos\Phi_\gamma - \cos\theta\cdot\sin\Theta_R\cos\Phi_R] \\ +\sin\Theta_e\sin\Phi_e\ &[\sin\Theta_\gamma\sin\Phi_\gamma - \cos\theta\cdot\sin\Theta_R\sin\Phi_R] \\ +\cos\Theta_e\ &[\cos\Theta_\gamma - \cos\theta\cdot\cos\Theta_R]\end{aligned} \tag{B.20}$$

Using $\Phi_R = \Phi_e + \pi$ and $\sin(x+\pi) = -\sin(x)$ and $\cos(x+\pi) = -\cos(x)$, one obtains:

$$\begin{aligned}\cos\phi_t = \sin\Theta_e\cos\Phi_e\ &[\sin\Theta_\gamma\cos\Phi_\gamma + \cos\theta\cdot\sin\Theta_R\cos\Phi_e] \\ +\sin\Theta_e\sin\Phi_e\ &[\sin\Theta_\gamma\sin\Phi_\gamma + \cos\theta\cdot\sin\Theta_R\sin\Phi_e] \\ +\cos\Theta_e\ &[\cos\Theta_\gamma - \cos\theta\cdot\cos\Theta_R]\end{aligned} \tag{B.21}$$

Applying eqs. B.5 and B.14, one can write:

$$\begin{aligned}\sin\Theta_R &= \sin(\arctan(x)) \equiv \frac{x}{\sqrt{1+x^2}} \\ \cos\Theta_R &= \cos(\arctan(x)) \equiv \frac{1}{\sqrt{1+x^2}}\end{aligned} \tag{B.22}$$

Substituting Eq. B.22 within Eq. B.21, one obtains:

$$\begin{aligned}\cos\phi_t = \sin\Theta_e\cos\Phi_e\ &\left[\sin\Theta_\gamma\cos\Phi_\gamma + \cos\theta_D\cdot\cos\Phi_p\frac{x}{\sqrt{1+x^2}}\right] \\ +\sin\Theta_e\sin\Phi_e\ &\left[\sin\Theta_\gamma\sin\Phi_\gamma + \cos\theta_D\cdot\sin\Phi_p\frac{x}{\sqrt{1+x^2}}\right] \\ +\cos\Theta_e\ &\left[\cos\Theta_\gamma - \cos\theta_D\cdot\frac{1}{\sqrt{1+x^2}}\right]\end{aligned} \tag{B.23}$$

After rearranging, we finally get:

$$\begin{aligned}\cos\phi_t =& \sin\Theta_e\sin\Theta_\gamma\cos(\Phi_e - \Phi_\gamma) + \cos\Theta_e\cos\Theta_\gamma \\ &+\cos\theta\cdot\frac{1}{\sqrt{1+x^2}}\left[x\cdot\sin\Theta_e - \cos\Theta_e\right]\end{aligned} \tag{B.24}$$

B.2 ^{119}Sn$(d, p\gamma)$ Coincidence Matrix

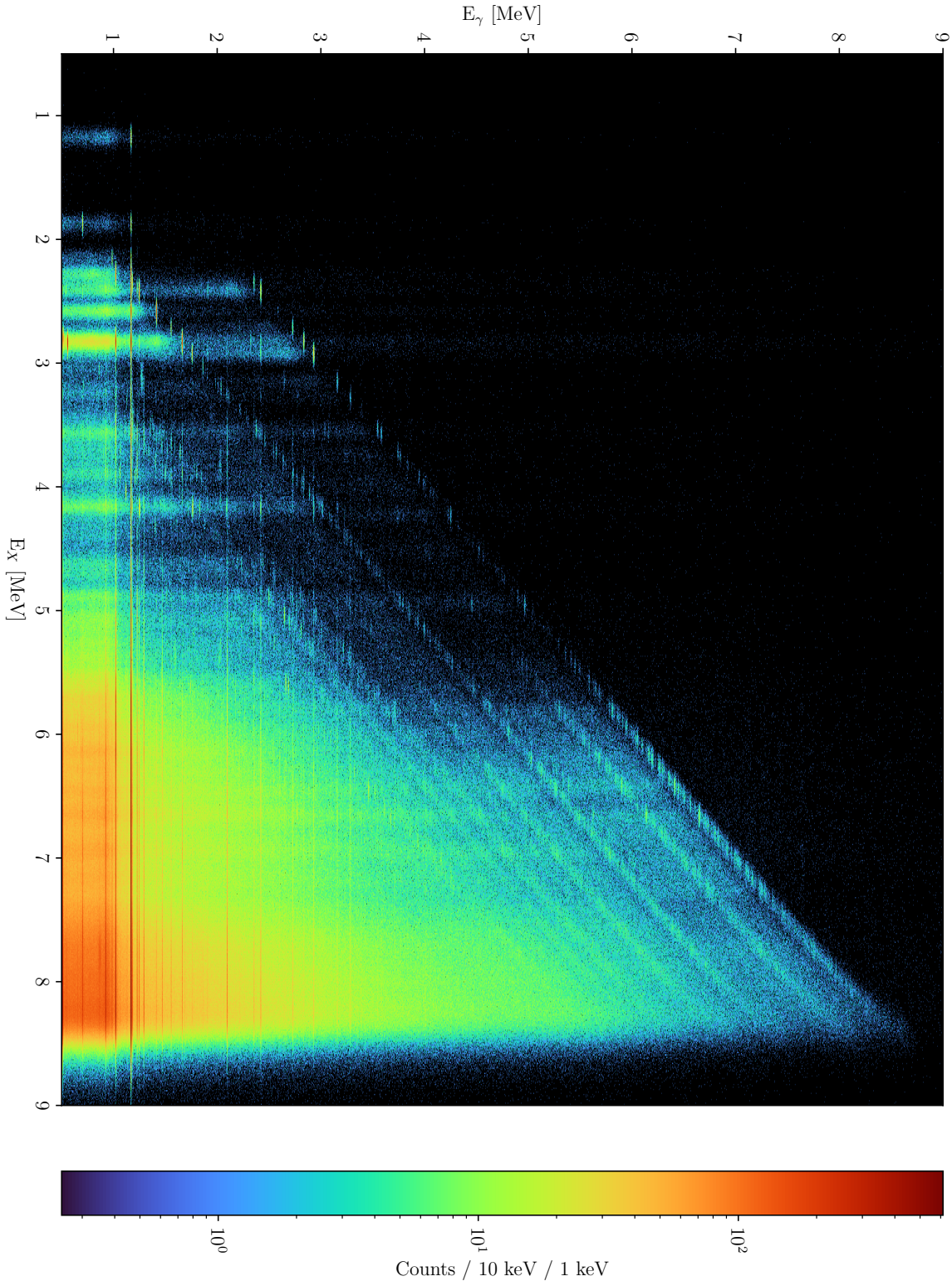

B.3 Angular-Distribution Normalization

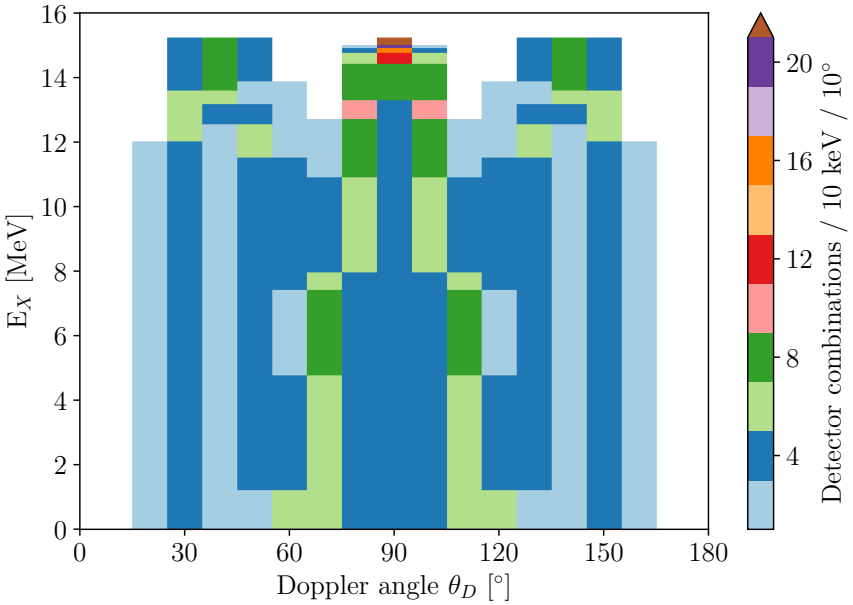

Figure 62: Distribution of ΔE $-$ E and HPGe detector combinations observing γ decay under the Doppler angle θ_D in 10° bins. See Fig. 30 and text in Chapter 3.5 for further explanation.

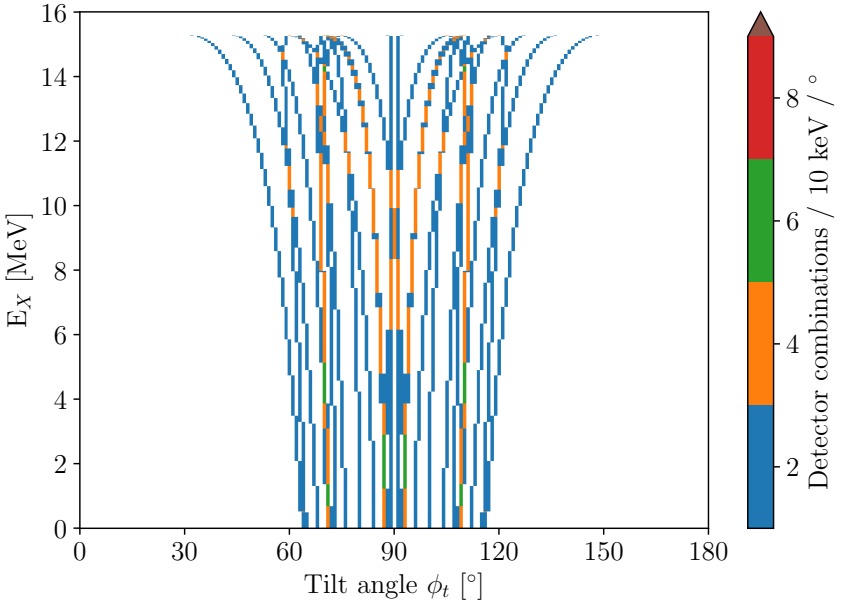

Figure 63: Available tilt angles ϕ_t between the reaction plane and γ-ray emission plane with SONIC-V1@HORUS. See Chapter 3.5 for further explanation.

B.4 ^{119}Sn$(d, p\gamma)$ Angular Distributions for Decays to the First Excited State

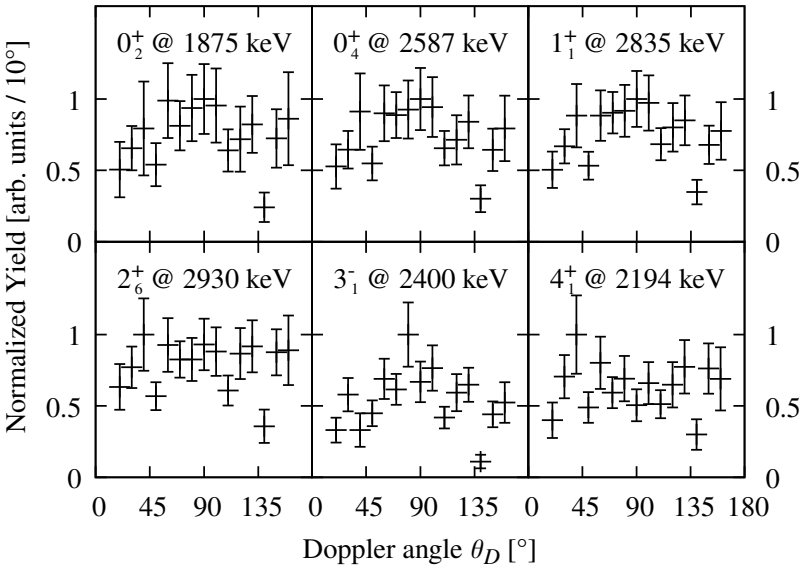

Figure 64: Angular distributions for decays to the first excited state in ^{120}Sn at 1171 keV. For each decaying level the known J^π and excitation energy are given.

B.5 ^{119}Sn$(d, p\gamma)$ Relative Experimental Yields

The following table lists experimental ^{119}Sn$(d, p\gamma)$ yields normalized to the strongest transition at 6644 keV. Spin and parity are given for known transitions (^{a}, [55]) and where angular distributions allowed an unambiguous spin identification in this work. Negative parity is assumed for all high-lying states as discussed in Chapter 3.5. Values in parentheses indicate a tentative assignment based on unclear angular distributions. The energy integrated cross section in (γ, γ'), I_S, is given where determined [50].

E_γ	J^π	$I_{(d,p\gamma)}$	I_S
1171.8	$2^{+,a}$	0.343(18)	-
2355.5	$2^{+,a}$	0.126(8)	-
2421.0	$2^{+,a}$	0.621(33)	-
2728.2	$2^{+,a}$	0.172(11)	-
2835.1	$2^{+,a}$	0.544(30)	-
2930.4	$2^{+,a}$	0.892(47)	-
3157.5	$2^{+,a}$	0.108(8)	-
3284.5	$2^{+,a}$	0.066(6)	-
3546.7	$1, 2^a$	0.082(7)	2.23(28)
3582.2	$1, 2^a$	0.082(7)	2.22(28)
3741.0	(2^+)	0.039(4)	-
3764.1	$2^{+,a}$	0.036(4)	-
3835.0	-	0.024(3)	-
3945.6	$2^{+,a}$	0.024(3)	-
3989.2	-	0.023(3)	-
4005.5	(2^+)	0.013(3)	-
4055.7	-	0.011(3)	2.23(26)
4083.6	(2^+)	0.012(3)	-
4223.7	(2^+)	0.016(3)	-
4250.2	1^-	0.086(7)	5.03(43)
4524.0	2^+	0.035(4)	-
4897.5	1^-	0.025(4)	2.70(26)
4963.3	1^-	0.118(9)	0.76(17)
5036.8	1^-	0.010(3)	1.71(21)
5290.8	1^-	0.020(3)	2.13(28)
5355.1	1^-	0.018(3)	1.86(24)
5410.6	1^-	0.025(5)	1.90(23)
5446.5	1^-	0.057(6)	4.56(38)
5490.9	1^-	0.039(6)	4.41(38)
5583.8	1^-	0.058(7)	-

E_γ	J^π	$I_{(d,p\gamma)}$	I_S
5622.9	1^-	0.010(4)	2.28(43)
5636.7	1^-	0.031(5)	3.69(36)
5647.7	1^-	0.050(7)	5.61(46)
5681.0	1^-	0.071(8)	3.75(36)
5700.0	1^-	0.017(4)	2.46(27)
5778.4	1^-	0.086(8)	2.04(25)
5805.6	1^-	0.236(18)	2.26(27)
5814.9	1^-	0.053(10)	4.37(40)
5827.8	1^-	0.052(7)	-
5853.5	1^-	0.062(9)	-
5862.8	1^-	0.092(11)	4.02(37)
5877.1	1^-	0.064(8)	-
5904.4	1^-	0.086(9)	-
5938.7	1^-	0.157(14)	6.38(53)
5949.2	1^-	0.055(9)	3.95(46)
5969.2	1^-	0.018(6)	3.71(36)
5988.9	1^-	0.067(9)	6.19(64)
6008.7	1^-	0.073(9)	1.73(27)
6028.3	1^-	0.126(14)	1.32(25)
6037.3	1^-	0.083(12)	-
6049.2	1^-	0.263(19)	2.05(28)
6092.8	1^-	0.174(15)	4.64(42)
6140.7	1^-	0.098(11)	7.22(58)
6158.6	1^-	0.322(22)	3.95(42)
6178.0	1^-	0.103(16)	-
6186.5	1^-	0.196(19)	3.32(35)
6195.9	1^-	0.255(21)	2.86(33)
6252.7	1^-	0.233(18)	7.78(62)
6265.8	1^-	0.300(22)	11.79(89)
6289.0	1^-	0.333(23)	6.45(53)

E_γ	J^π	$I_{(d,p\gamma)}$	I_S
6304.9	1^-	0.165(15)	9.22(72)
6351.2	1^-	0.369(25)	9.73(77)
6367.6	1^-	0.111(12)	3.11(38)
6381.6	1^-	0.112(12)	-
6407.2	1^-	0.787(46)	14.7(11)
6423.3	1^-	0.101(12)	-
6442.1	1^-	0.366(25)	9.48(75)
6466.2	1^-	0.168(16)	10.26(80)
6488.1	1^-	0.147(16)	-
6500.5	1^-	0.210(19)	3.71(46)
6557.9	1^-	0.255(20)	3.80(47)
6604.0	1^-	0.113(14)	4.30(42)
6643.5	1^-	1.000(57)	12.63(97)
6659.1	1^-	0.158(17)	3.14(36)
6704.4	1^-	0.258(21)	5.10(47)
6726.5	1^-	0.347(25)	6.17(56)
6795.0	1^-	0.408(28)	7.18(80)
6825.1	1^-	0.408(29)	3.2(4)
6912.9	-	0.323(24)	-
6954.0	1^-	0.170(16)	3.96(43)
6987.9	(2^+)	0.283(22)	10.86(89)
7005.1	1^-	0.179(22)	6.89(108)
7016.7	(2^+)	0.235(24)	-
7029.9	1^-	0.182(20)	5.87(65)
7043.4	-	0.177(18)	-
7096.6	1^-	0.312(28)	6.40(102)
7113.0	1^-	0.212(60)	4.46(46)
7122.2	-	0.120(66)	-
7142.6	1^-	0.115(18)	6.74(62)
7156.5	1^-	0.325(27)	-
7182.0	1^-	0.077(13)	2.82(38)
7221.0	1^-	0.185(20)	8.27(86)
7235.6	1^-	0.259(24)	7.86(76)
7249.4	1^-	0.257(25)	5.05(63)
7272.9	1^-	0.223(22)	3.11(80)
7285.5	1^-	0.129(18)	-
7311.9	1^-	0.095(14)	3.67(42)
7353.5	-	0.162(18)	7.07(66)
7439.7	-	0.107(16)	4.87(54)
7562.7	1^-	0.103(16)	6.6 (70)
7646.0	-	0.108(18)	1.36(38)

C Appendix C

C.1 NuDAQ – Centralized Server Station and Laboratory Cable Routing

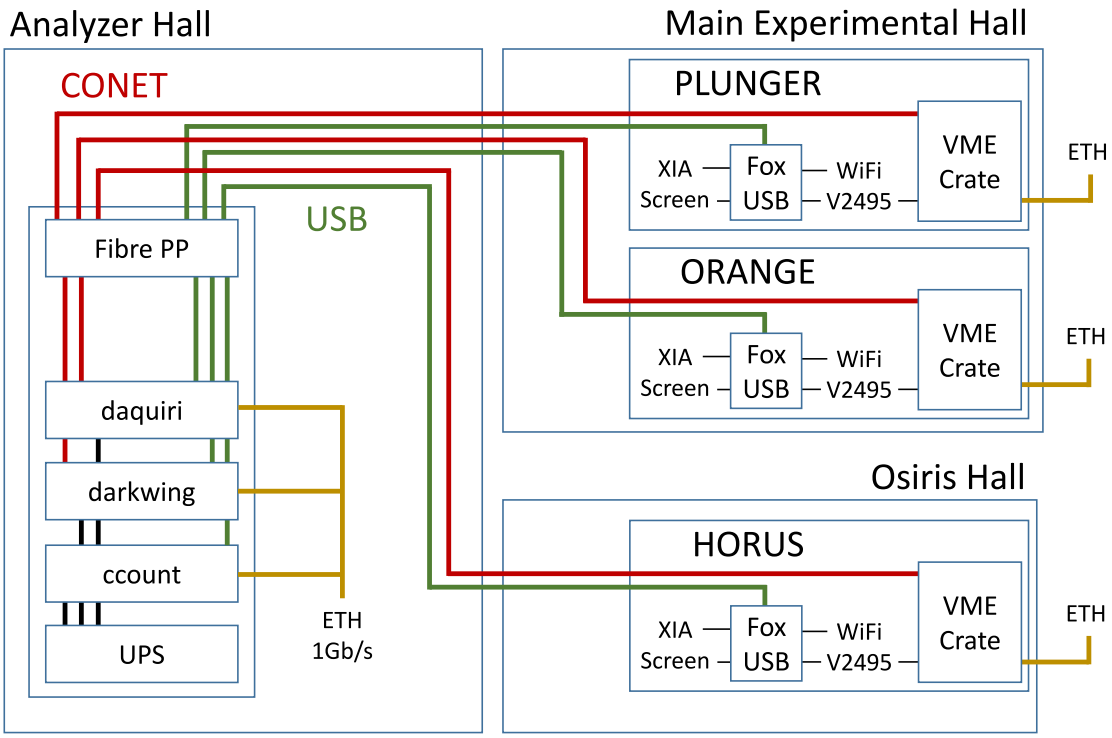

Centralized DAQ servers (daquiri, darkwing, ccount) in the Analyzer Hall are powered by an uninterruptible-power-supply (UPS) and connected via two fibre-channel cables to each setup for CONET and USB communication. A 1 Gb/s ethernet connection allows fast transfer of collected raw data to analysis servers. At each experiment, digitizers are read out via the CONET connection and auxiliary devices are accessible via USB. Each VME-Crate is remote-controllable via ethernet and the V2495 multiplicity filter is configured via the fibre-channel USB connection. Legacy support for the XIA system is provided via the fibre-channel USB connection.

C.2 NuDAQ Multiplicity Filter – Schematic Connections and Signal Flow

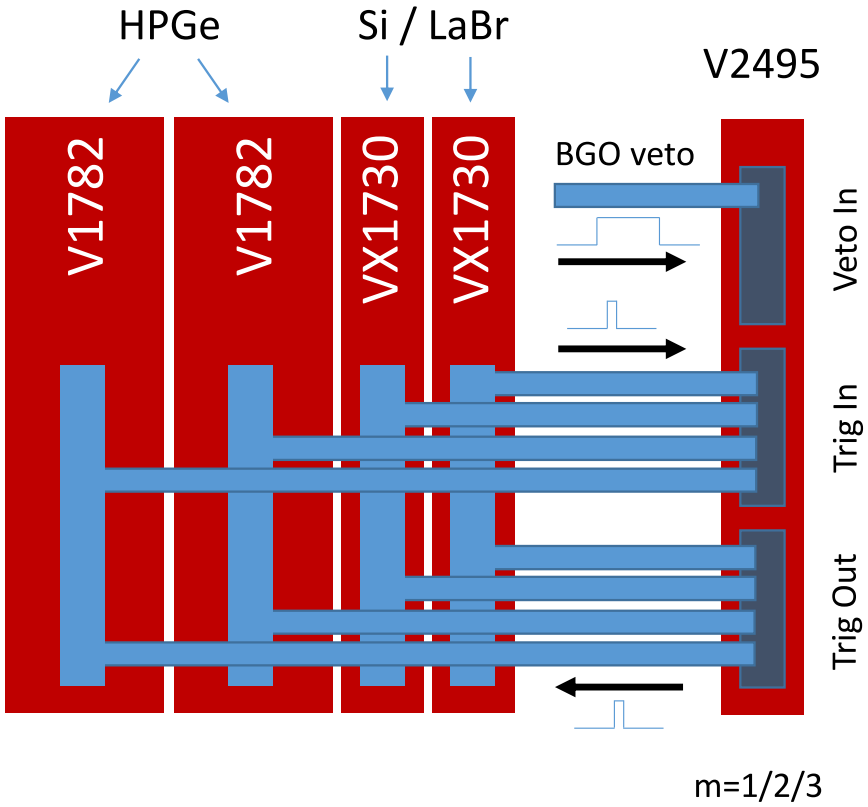

Multiplicity filter signal routing. Flat cables connect the upper LVDS outputs of each digitizer to the V2495 trigger-request inputs and the trigger-acknowledgement outputs from the V2495 back to the lower LVDS input on each digitizer. Logic BGO-vetos are fed into the dedicated veto input as differential LVDS signals. An external global veto can be fed in via the G0 input and the G1 output allows to observe the M=1/2/3 multiplicity rate via an oscilloscope (not shown).

List of Figures

References

[1] J. Chadwick, *Possible existence of a Neutron,* Nature **129**, 312 (1932)

[2] H. A. Bethe, *Energy Production in Stars,* Physical Review **55**, 434 (1939)

[3] M. Goeppert Mayer, *On Closed Shells in Nuclei,* Physical Review **74**, 235 (1948)

[4] M. N. Harakeh and A. van der Woude, *Giant Resonances - High-Frequency Modes of Nuclear Excitation*, 2nd ed. (Oxford Press, 2001)

[5] P. Bortignon, A. Bracco, and R. Broglia, *Nuclear Structure at Finite Temperature* (Harwood Academic Publishers, 1998)

[6] W. Bothe and W. Gentner, *Atomumwandlungen durch γ-Strahlen,* Zeitschrift für Physik **106**, 236 (1937)

[7] A. B. Migdal, J. Phys (USSR) **8**, 331 (1944)

[8] M. N. Harakeh, K. van der Borg, T. Ishimatsu, H. P. Morsch, A. van der Woude, and F. E. Bertrand, *Direct Evidence for a New Giant Resonance at $80A^{-1/3}$ MeV in the Lead Region,* Physical Review Letters **38**, 676 (1977)

[9] M. N. Harakeh and A. E. L. Dieperink, *Isoscalar dipole resonance: Form factor and energy weighted sum rule,* Physical Review C **23**, 2329 (1981)

[10] F. Reiche and W. Thomas, Zeitschrift für Physik **34**, 510 (1925)

[11] W. Kuhn, *Über die Gesamtstärke der von einem Zustande ausgehenden Absorptionslinien.* Zeitschrift für Physik **33**, 408 (1925)

[12] G. A. Bartholomew, *Neutron Capture Gamma Rays,* Annual Review of Nuclear Science **11**, 259 (1961)

[13] R. Mohan, M. Danos, and L. C. Biedenharn, *Three-fluid hydrodynamical model of nuclei,* Phys. Rev. C **3**, 1740 (1971)

[14] D. Vretenar, N. Paar, P. Ring, T. Nikšić, and T. Nikšić, *Toroidal dipole, resonances in the relativistic random phase approximation,* Physical Review C **65**, 021301(R) (2002)

[15] A. Repko, P. G. Reinhard, V. O. Nesterenko, and J. Kvasil, *Toroidal nature of the low-energy E1 mode,* Physical Review C **87**, 024305 (2013)

[16] F. Iachello, *Local versus Global Isospin Symmetry in Nuclei,* Physics Letters B **160**, 1 (1985)

[17] M. Spieker, S. Pascu, A. Zilges, and F. Iachello, *Origin of low-lying enhanced E1 strength in rare-earth nuclei,* Physical Review Letters **114**, 192504 (2015)

[18] D. Savran, T. Aumann, and A. Zilges, *Experimental studies of the Pygmy Dipole Resonance,* Prog. Part. Nucl. Phys. **70**, 210 (2013)

[19] A. Bracco, E. G. Lanza, and A. Tamii, *Isoscalar and isovector dipole excitations: Nuclear properties from low-lying states and from the isovector giant dipole resonance,* Prog. Part. Nucl. Phys. **106**, 360 (2019)

[20] J. S. Brzosko, E. Gierlik, A. Soltan Jr., and Z. Wilhelmi, *Effect of the pigmy resonance on the calculations of the neutron capture cross section,* Canadian Journal of Physics **47**, 2849 (1969)

[21] S. Goriely, *Radiative neutron captures by neutron-rich nuclei and the r-process nucleosynthesis,* Physics Letters B **436**, 10 (1998)

[22] S. Goriely and E. Khan, *Large-scale QRPA calculation of E1-strength and its impact on the neutron capture cross section,* Nuclear Physics A **706**, 217 (2002)

[23] S. Goriely, E. Khan, and M. Samyn, *Microscopic HFB + QRPA predictions of dipole strength for astrophysics applications,* Nuclear Physics A **739**, 331 (2004)

[24] I. Daoutidis and S. Goriely, *Large-scale continuum random-phase approximation predictions of dipole strength for astrophysical applications,* Physical Review C **86**, 034328 (2012)

[25] A. Tonchev, N. Tsoneva, C. Bhatia, C. Arnold, S. Goriely, S. Hammond, J. Kelley, E. Kwan, H. Lenske, J. Piekarewicz, R. Raut, G. Rusev, T. Shizuma, and W. Tornow, *Pygmy and core polarization dipole modes in ^{206}Pb: Connecting nuclear structure to stellar nucleosynthesis,* Physics Letters B **773**, 20 (2017)

[26] A. C. Larsen, A. Spyrou, S. N. Liddick, and M. Guttormsen, *Novel techniques for constraining neutron-capture rates relevant for r-process heavy-element nucleosynthesis,* Prog. Part. Nucl. Phys. **107**, 69 (2019)

[27] A. Spyrou, S. N. Liddick, A. C. Larsen, M. Guttormsen, K. Cooper, A. C. Dombos, D. J. Morrissey, F. Naqvi, G. Perdikakis, S. J. Quinn, T. Renstrøm, J. A. Rodriguez, A. Simon, C. S. Sumithrarachchi, and R. G. Zegers, *Novel technique for constraining r-process (n, γ) reaction rates,* Physical Review Letters **113**, 232502 (2014)

[28] H. Utsunomiya, S. Goriely, H. Akimune, H. Harada, F. Kitatani, S. Goko, H. Toyokawa, K. Yamada, T. Kondo, O. Itoh, M. Kamata, T. Yamagata, Y. W. Lui,

I. Daoutidis, D. P. Arteaga, S. Hilaire, and A. J. Koning, *γ-ray strength function method and its application to ^{107}Pd,* Physical Review C **82**, 064610 (2010)

[29] A. Arcones *et al.*, *White paper on nuclear astrophysics and low energy nuclear physics Part 1: Nuclear astrophysics,* Prog. Part. Nucl. Phys. **94**, 1 (2017)

[30] G. Potel, F. M. Nunes, and I. J. Thompson, *Establishing a theory for deuteron-induced surrogate reactions,* Physical Review C **92**, 034611 (2015)

[31] A. Ratkiewicz, J. Cizewski, J. Escher, G. Potel, J. Burke, R. Casperson, M. McCleskey, R. Austin, S. Burcher, R. Hughes, B. Manning, S. Pain, W. Peters, S. Rice, T. Ross, N. Scielzo, C. Shand, and K. Smith, *Towards Neutron Capture on Exotic Nuclei: Demonstrating $(d, p\gamma)$ as a Surrogate Reaction for (n,γ),* Physical Review Letters **122**, 052502 (2019)

[32] P. G. Reinhard and W. Nazarewicz, *Information content of a new observable: The case of the nuclear neutron skin,* Physical Review C **81**, 051303(R) (2010)

[33] J. Piekarewicz, *Pygmy resonances and neutron skins,* Physical Review C **83**, 034319 (2011)

[34] M. Baldo and G. F. Burgio, *The nuclear symmetry energy,* Prog. Part. Nucl. Phys. **91**, 203 (2016)

[35] X. Roca-Maza and N. Paar, *Nuclear equation of state from ground and collective excited state properties of nuclei,* Prog. Part. Nucl. Phys. **101**, 96 (2018)

[36] M. Thiel, C. Sfienti, J. Piekarewicz, C. J. Horowitz, and M. Vanderhaeghen, *Neutron skins of atomic nuclei: Per aspera ad astra,* J. Phys. G **46**, 093003 (2019)

[37] S. Bassauer, P. von Neumann-Cosel, P. G. Reinhard, A. Tamii, S. Adachi, C. A. Bertulani, P. Y. Chan, G. Colò, A. D'Alessio, H. Fujioka, H. Fujita, Y. Fujita, G. Gey, M. Hilcker, T. H. Hoang, A. Inoue, J. Isaak, C. Iwamoto, T. Klaus, N. Kobayashi, Y. Maeda, M. Matsuda, N. Nakatsuka, S. Noji, H. J. Ong, I. Ou, N. Paar, N. Pietralla, V. Y. Ponomarev, M. S. Reen, A. Richter, X. Roca-Maza, M. Singer, G. Steinhilber, T. Sudo, Y. Togano, M. Tsumura, Y. Watanabe, and V. Werner, *Evolution of the dipole polarizability in the stable tin isotope chain,* Physics Letters B **810**, 135804 (2020)

[38] T. W. Donnelly and J. Dubach, *Isospin Dependencies in Parity-Violating Electron Scattering,* Nuclear Physics A **503**, 589 (1989)

[39] D. Adhikari *et al.*, *Accurate Determination of the Neutron Skin Thickness of ^{208}Pb through Parity-Violation in Electron Scattering,* Physical Review Letters **126**, 172502 (2021)

[40] A. Zilges, D. L. Balabanski, J. Isaak, and N. Pietralla, *Photonuclear reactions — From basic research to applications,* Prog. Part. Nucl. Phys. **122**, 103903 (2022)

[41] J. Endres, D. Savran, A. M. v. d. Berg, P. Dendooven, M. Fritzsche, M. N. Harakeh, J. Hasper, H. J. Wörtche, and A. Zilges, *Splitting of the pygmy dipole resonance in ^{138}Ba and ^{140}Ce,* Physical Review C **80**, 034302 (2009)

[42] J. Endres, D. Savran, P. A. Butler, M. N. Harakeh, S. Harissopulos, R.-D. Herzberg, R. Krücken, A. Lagoyannis, E. Litvinova, N. Pietralla, V. Ponomarev, L. Popescu, P. Ring, M. Scheck, F. Schlüter, K. Sonnabend, V. I. Stoica, H. J. Wörtche, and A. Zilges, *Structure of the pygmy dipole resonance in ^{124}Sn,* Physical Review C **85**, 064331 (2012)

[43] E. G. Lanza, A. Vitturi, E. Litvinova, and D. Savran, *Dipole excitations via isoscalar probes: The splitting of the pygmy dipole resonance in ^{124}Sn,* Physical Review C **89**, 041601(R) (2014)

[44] L. Pellegri *et al.*, *Pygmy dipole resonance in ^{124}Sn populated by inelastic scattering of ^{17}O,* Physics Letters B **738**, 519 (2014)

[45] A. Bracco, F. C. L. Crespi, and E. G. Lanza, *Gamma decay of pygmy states from inelastic scattering of ions,* European Physical Journal A **51**, 99 (2015)

[46] D. Savran, V. Derya, S. Bagchi, J. Endres, M. Harakeh, J. Isaak, N. Kalantar-Nayestanaki, E. Lanza, B. Löher, A. Najafi, S. Pascu, S. Pickstone, N. Pietralla, V. Ponomarev, C. Rigollet, C. Romig, M. Spieker, A. Vitturi, and A. Zilges, *Multi-messenger investigation of the Pygmy Dipole Resonance in ^{140}Ce,* Physics Letters B **786**, 16 (2018)

[47] D. Vretenar, N. Paar, P. Ring, and G. A. Lalazissis, *Collectivity of the low-lying dipole strength in relativistic random phase approximation,* Nuclear Physics A **692**, 496 (2001)

[48] E. G. Lanza, F. Catara, D. Gambacurta, M. V. Andrés, and P. Chomaz, *Multiphonon excitations and pygmy resonances in tin isotopes,* Physical Review C **79**, 054615 (2009)

[49] G. A. Bartholomew, E. D. Earle, A. J. Ferguson, and I. Bergqvist, *Gamma Ray Intensity Anomaly in the $(d, p\gamma)$ Reaction,* Physics Letters B **24**, 47 (1967)

[50] M. Müscher, J. Wilhelmy, R. Massarczyk, R. Schwengner, M. Grieger, J. Isaak, A. R. Junghans, T. Kögler, F. Ludwig, D. Savran, D. Symochko, M. P. Takács, M. Tamkas, A. Wagner, and A. Zilges, *High-sensitivity investigation of low-lying dipole strengths in ^{120}Sn,* Physical Review C **102**, 014317 (2020)

[51] H. Matsubara, *Isoscalar and isovector spin-M1 transitions from the even-even, N=Z nuclei across the sd-shell region*, Ph.D. thesis, Osaka University (2009)

[52] N. Kobayashi, K. Miki, T. Hashimoto, C. Iwamoto, A. Tamii, N. Aoi, M. P. Carpenter, K. Hatanaka, J. Isaak, E. Ideguchi, S. Morinobu, S. Nakamura, and S. Noji, *Excitation and γ-decay coincidence measurements at the GRAF beamline for studies of pygmy and giant dipole resonances,* European Physical Journal A **55**, 231 (2019)

[53] L. G. Morris, *Electromagnetic transitions as a probe for Superdeformation in ^{28}Si*, Ph.D. thesis, University of York (2019)

[54] M. Shamsuzzoha Basunia, *Nuclear data sheets for A = 28,* Nuclear Data Sheets **114**, 1189 (2013)

[55] K. Kitao, Y. Tendow, and A. Hashizume, *Nuclear data sheets for A = 120,* Nuclear Data Sheets **96**, 241 (2002)

[56] I. Y. Lee, R. M. Clark, M. Cromaz, M. A. Deleplanque, M. Descovich, R. M. Diamond, P. Fallon, A. O. Macchiavelli, F. S. Stephens, and D. Ward, *GRETINA: A gamma ray energy tracking array,* Nuclear Physics A **746**, 255 (2004)

[57] I. Y. Lee, *The GAMMASPHERE,* Nuclear Physics A **520**, c641 (1990)

[58] C. Sullivan, R. G. T. Zegers, S. Noji, S. M. Austin, J. Schmitt, N. Aoi, D. Bazin, M. Carpenter, J. J. Carroll, H. Fujita, U. Garg, G. Gey, C. J. Guess, T. H. Hoang, M. N. Harakeh, E. Hudson, N. Ichige, E. Ideguchi, A. Inoue, J. Isaak, C. Iwamoto, C. Kacir, T. Koike, N. Kobayashi, S. Lipschutz, M. Liu, H. J. Ong, J. Pereira, M. K. Raju, A. Tamii, R. Titus, V. Werner, Y. Yamamoto, Y. D. Fang, J. C. Zamora, S. Zhu, and X. Zhou, *The $(^6Li,^6 Li^*[3.56MeV])$ reaction at 100 MeV / u as a probe of Gamow-Teller transition strengths in the inelastic scattering channel,* Physical Review C **98**, 015804 (2018)

[59] L. Morris, D. G. Jenkins, M. N. Harakeh, J. Isaak, N. Kobayashi, A. Tamii, S. Adachi, P. Adsley, N. Aoi, A. Bracco, A. Brown, M. P. Carpenter, J. J. Carroll, S. Courtin, F. C. L. Crespi, P. J. Davies, G. Fruet, Y. D. Fang, H. Fujita, G. Gey, T. H.

Hoang, N. Ichige, E. Ideguchi, A. Inoue, C. Iwamoto, and T. Koike, *Search for in-band transitions in the candidate superdeformed band in ^{28}Si*, Physical Review C **104**, 054323 (2021)

[60] F. Crespi, A. Bracco, E. Lanza, A. Tamii, N. Blasi, F. Camera, O. Wieland, N. Aoi, D. L. Balabanski, S. Bassauer, A. S. Brown, M. P. Carpenter, J. J. Carroll, M. Ciemała, A. Czeszumska, P. J. Davies, V. Derya, L. M. Donaldson, Y. D. Fang, M. Krzysiek, M. K. Raju, M. Liu, A. Maj, L. Morris, P. von Neumann-Cosel, S. Noji, H. J. Ong, S. G. Pickstone, N. Pietralla, D. Savran, J. M. Schmitt, M. Spieker, T. Yamamoto, R. G. T. Zegers, X. Zhou, S. Zhu, and A. Zilges, *The structure of low-lying 1$^-$ states in ^{90,94}Zr from $(\alpha, \alpha'\gamma)$ and $(p, p'\gamma)$ reactions*, Physics Letters B **816**, 136210 (2021)

[61] G. F. Knoll, *Radiation Detection and Measurement*, 4th ed. (Wiley, 2010)

[62] T. D. Poelhekken, S. K. B. Hesmondhalgh, H. J. Hofmann, A. Van Der Woude, and M. N. Harakeh, *Low-energy isoscalar dipole strength in ^{40}Ca, ^{58}Ni, ^{90}Zr and ^{208}Pb*, Physics Letters B **278**, 423 (1992)

[63] J. Endres, *Systematic studies of the Pygmy Dipole Resonance with hadronic and electromagnetic probes*, Ph.D. thesis, University of Cologne (2011)

[64] V. Derya, J. Endres, M. Elvers, M. Harakeh, N. Pietralla, C. Romig, D. Savran, M. Scheck, F. Siebenhühner, V. Stoica, H. Wörtche, and A. Zilges, *Study of the pygmy dipole resonance in ^{94}Mo using the coincidence technique*, Nuclear Physics A **906**, 94 (2013)

[65] P. D. Kunz, *CHUCK* DWBA Software, University of Colorado (unpublished)

[66] J. R. Comfort and M. N. Harakeh, *CHUCK3* DWBA Software, modified version of CHUCK, unpublished (1979)

[67] M. N. Harakeh and L. W. Put, ANGCOR, KVI internal report 67i (unpublished), (1979)

[68] P. Adsley, *AngCorPackage* Software Compilation, https://github.com/padsley/AngCorPackage (2019)

[69] G. R. Satchler, *The Distorted-Waves Theory of Direct Nuclear Reactions with Spin-Orbit Effects*, Nuclear Physics **55**, 1 (1964)

[70] H. J. Rose, *Angular Distributions of Gamma Rays in Terms of Phase-Defined Reduced Matrix Elements*, Reviews of Modern Physics **39**, 306 (1967)

[71] F. Rybicki, T. Tamura, and G. R. Satchler, *Particle-Gamma Angular Correlations following Nuclear Reactions,* Nuclear Physics A **146**, 659 (1970)

[72] J. G. Cramer and W. W. Eidson, *Angular Correlations and Nuclear Polarization from the Inelastic Scattering of Alpha Particles,* Nuclear Physics **55**, 593 (1964)

[73] W. W. Eidson, J. G. Cramer, D. E. Blatchley, and R. D. Bent, *Angular Correlation Studies of Nuclear Polarization following Inelastic Scattering of Alpha Particles from ^{12}C and ^{24}Mg,* Nuclear Physics **55**, 613 (1964)

[74] M. Nolte, H. Machner, and J. Bojowald, *Global optical potential for particles with energies above 80 MeV,* Physical Review C **36**, 1312 (1987)

[75] M. E. Rose, *Angular Correlation in Allowed Beta-Transitions,* Physical Review **91**, 197 (1953)

[76] M. Weinert, M. Spieker, G. Potel, N. Tsoneva, M. Müscher, J. Wilhelmy, and A. Zilges, *Microscopic Structure of the Low-Energy Electric Dipole Response of ^{120}Sn,* Physical Review Letters **127**, 242501 (2021)

[77] M. Weinert, *Study of the Pygmy Dipole Resonance in ^{120}Sn using the $(d, p\gamma)$ reaction*, Master's thesis, Institute for Nuclear Physics, University of Cologne (2016)

[78] M. Weinert, *psonar* Analysis Software, https://gitlab.ikp.uni-koeln.de/mweinert/psonar (2022)

[79] S. Bassauer, P. von Neumann-Cosel, P. G. Reinhard, A. Tamii, S. Adachi, C. A. Bertulani, P. Y. Chan, A. D'Alessio, H. Fujioka, H. Fujita, Y. Fujita, G. Gey, M. Hilcker, T. H. Hoang, A. Inoue, J. Isaak, C. Iwamoto, T. Klaus, N. Kobayashi, Y. Maeda, M. Matsuda, N. Nakatsuka, S. Noji, H. J. Ong, I. Ou, N. Pietralla, V. Y. Ponomarev, M. S. Reen, A. Richter, M. Singer, G. Steinhilber, T. Sudo, Y. Togano, M. Tsumura, Y. Watanabe, and V. Werner, *Electric and magnetic dipole strength in $^{112,114,116,118,120,124}Sn$,* Physical Review C **102**, 034327 (2020)

[80] P. Kuchenbrod, *Towards the reduced dipole transition strength B(E1) in ^{120}Sn below the neutron threshold*, Master's thesis, Institute for Nuclear Physics, TU Darmstadt (2022)

[81] A. Hennig, M. Spieker, V. Werner, T. Ahn, V. Anagnostatou, N. Cooper, V. Derya, M. Elvers, J. Endres, P. Goddard, A. Heinz, R. O. Hughes, G. Ilie, M. N. Mineva, P. Petkov, S. G. Pickstone, N. Pietralla, D. Radeck, T. J. Ross, D. Savran, and A. Zilges, *Mixed-symmetry octupole and hexadecapole excitations in the N=52 isotones,* Physical Review C **90**, 051302(R) (2014)

[82] A. Hennig, T. Ahn, V. Anagnostatou, A. Blazhev, N. Cooper, V. Derya, M. Elvers, J. Endres, P. Goddard, A. Heinz, R. O. Hughes, G. Ilie, M. N. Mineva, P. Petkov, S. G. Pickstone, N. Pietralla, D. Radeck, T. J. Ross, D. Savran, M. Spieker, V. Werner, and A. Zilges, *Collective excitations of ^{96}Ru by means of $(p, p'\gamma)$ experiments,* Physical Review C **92**, 064317 (2015)

[83] A. Hennig, V. Derya, M. N. Mineva, P. Petkov, S. G. Pickstone, M. Spieker, and A. Zilges, *Lifetime measurement of excited low-spin states via the $(p, p'\gamma)$ reaction,* Nucl. Instr. Meth. A **794**, 171 (2015)

[84] A. Hennig, *Study of Proton-Neutron Mixed-Symmetry Excitations in ^{96}Ru by Means of Inelastic Proton Scattering and Digital Pulse Processing of Semiconductor Detector Signals*, Ph.D. thesis, University of Cologne (2014)

[85] M. Spieker, N. Tsoneva, V. Derya, J. Endres, D. Savran, M. Harakeh, S. Harissopulos, R.-D. Herzberg, A. Lagoyannis, H. Lenske, N. Pietralla, L. Popescu, M. Scheck, F. Schlüter, K. Sonnabend, V. Stoica, H. Wörtche, and A. Zilges, *The pygmy quadrupole resonance and neutron-skin modes in ^{124}Sn,* Physics Letters B **752**, 102 (2016)

[86] M. Spieker, P. Petkov, E. Litvinova, S. G. Pickstone, S. Prill, P. Scholz, and A. Zilges, *Shape coexistence and collective low-spin states in ^{112,114}Sn studied with the $(p, p'\gamma)$ Doppler-shift attenuation coincidence technique,* Physical Review C **97**, 054319 (2018)

[87] M. Färber, M. Weinert, M. Müscher, M. Spieker, J. Wilhelmy, and A. Zilges, *Low-energy excitations and γ-decay branchings in ^{124}Sn via $(p, p'\gamma)$ at E_p = 15 MeV,* European Physical Journal A **57**, 191 (2021)

[88] S. Prill, A. Bohn, V. Everwyn, G. Häfner, F. Heim, M. Spieker, M. Weinert, J. Wilhelmy, and A. Zilges, *Lifetime analysis of ^{128,130}Te via the Doppler-shift attenuation method,* Physical Review C **105**, 034319 (2022)

[89] S. G. Pickstone, M. Weinert, M. Färber, F. Heim, E. Hoemann, J. Mayer, M. Müscher, S. Prill, P. Scholz, M. Spieker, V. Vielmetter, J. Wilhelmy, and A. Zilges, *Combining γ-ray and particle spectroscopy with SONIC@HORUS,* Nucl. Instr. Meth. A **875**, 104 (2017)

[90] S. G. Pickstone, *Upgrading the particle spectrometer SONIC and $(p, p'\gamma)$ coincidence measurements on ^{92}Mo, ^{94}Mo and ^{60}Ni*, Ph.D. thesis, University of Cologne (2018)

[91] M. Weinert, *Untersuchung und Korrektur differentieller Nichtlinearitäten in Analog-zu-Digital-Konvertern*, Bachelor's thesis, Institute für Kernphysik, University of Cologne (2013)

[92] J. Allison *et al.*, *Recent developments in GEANT4*, Nucl. Instr. Meth. A **835**, 186 (2016)

[93] J. Mayer, *G4Horus* Simulation Software Package, https://gitlab.ikp.uni-koeln.de/jmayer/g4horus (2020)

[94] P. J. Nolan and J. F. Sharpey-Schafer, *The measurement of the lifetimes of excited nuclear states,* Rep. Prog. Phys. **42**, 1 (1979)

[95] A. Bohn, *Lifetime determination of excited states in ^{104}Ru via the Doppler-shift attenuation method*, Master's thesis, Institute for Nuclear Physics, University of Cologne (2021)

[96] J. Endres, E. Litvinova, D. Savran, P. A. Butler, M. N. Harakeh, S. Harissopulos, R. D. Herzberg, R. Krücken, A. Lagoyannis, N. Pietralla, V. Ponomarev, L. Popescu, P. Ring, M. Scheck, K. Sonnabend, V. I. Stoica, H. J. Wörtche, and A. Zilges, *Isospin character of the pygmy dipole resonance in ^{124}Sn,* Physical Review Letters **105**, 212503 (2010)

[97] J. A. Wilhelmy, *Protonen-Gamma-Winkelverteilungen für den kombinierten Aufbau SONIC&HORUS*, Bachelor's thesis, Institute for Nuclear Physics, University of Cologne (2014)

[98] M. Färber, *Study of $^{60}Ni(p, p\gamma)$ angular correlations and the dipole response of ^{124}Sn using SONIC@HORUS*, Master's thesis, Institute for Nuclear Physics, University of Cologne (2019)

[99] B. Wasilewska, private communication (2022)

[100] A. Bohn, private communication (2022)

[101] R. F. Casten, *Nuclear Structure from a Simple Perspective* (Oxford University Press, 2001)

[102] P. Ring and P. Schuck, *The Nuclear Many-Body Problem*, 2nd ed. (Springer, 2004)

[103] E. G. Lanza and A. Vitturi, *Handbook on Nuclear Physics - Theoretical Description of Pygmy (Dipole) Resonances* (Springer - In Preparation, 2022)

[104] H. Hergert, *A Guided Tour of ab initio Nuclear Many-Body Theory,* Frontiers in Physics **8**, 379 (2020)

[105] S. R. Stroberg, J. D. Holt, A. Schwenk, and J. Simonis, *Ab Initio Limits of Atomic Nuclei,* Physical Review Letters **126**, 022501 (2021)

[106] B. Hu, W. Jiang, T. Miyagi, Z. Sun, A. Ekström, C. Forssén, G. Hagen, J. D. Holt, T. Papenbrock, S. R. Stroberg, and I. Vernon, *Ab initio predictions link the neutron skin of ^{208}Pb to nuclear forces,* Nature Physics (2022), 10.1038/s41567-022-01715-8

[107] D. Hartree, *The Wave Mechanics of an Atom with a Non-Coulomb Central Field Part II,* Mathematical Proceedings of the Cambridge Philosophical Society **24**, 111 (1928)

[108] V. Fock, *Näherungsmethode zur Lösung des quantenmechanischen Mehrkörperproblems,* Zeitschrift für Physik **61**, 126 (1930)

[109] T. H. Skyrme, *The effective nuclear potential,* Nuclear Physics **9**, 615 (1958)

[110] J. Dechargé and D. Gogny, *Hartree-Fock-Bogolyubov calculations with the D1 effective interaction on spherical nuclei,* Physical Review C **21**, 1568 (1980)

[111] V. I. Tselyaev, *Quasiparticle time blocking approximation within the framework of generalized Green function formalism,* Physical Review C **75**, 024306 (2007)

[112] E. Litvinova, P. Ring, and V. Tselyaev, *Relativistic quasiparticle time blocking approximation: Dipole response of open-shell nuclei,* Physical Review C **78**, 014312 (2008)

[113] E. Litvinova, P. Ring, and V. Tselyaev, *Relativistic two-phonon model for the low-energy nuclear response,* Physical Review C **88**, 044320 (2013)

[114] N. Tsoneva and H. Lenske, *Energy–density functional plus quasiparticle–phonon model theory as a powerful tool for nuclear structure and astrophysics,* Physics of Atomic Nuclei **79**, 885 (2016)

[115] V. G. Soloviev, *Theory of Complex Nuclei* (Pergamon Press, Oxford, 1976)

[116] V. Y. Ponomarev, C. Stoyanov, N. Tsoneva, and M. Grinberg, *Boson forbidden low-energy E1-transitions in spherical nuclei,* Nuclear Physics A **635**, 470 (1998)

[117] M. Grinberg, C. Stoyanov, and N. Tsoneva, *Interplay of collective and noncollective modes at low excitation energy in spherical nuclei,* Physics of Particles and Nuclei **29**, 606 (1998)

[118] B. Löher, D. Savran, T. Aumann, J. Beller, M. Bhike, N. Cooper, V. Derya, M. Duchêne, J. Endres, A. Hennig, P. Humby, J. Isaak, J. H. Kelley, M. Knörzer, N. Pietralla, V. Y. Ponomarev, C. Romig, M. Scheck, H. Scheit, J. Silva, A. P.

Tonchev, W. Tornow, F. Wamers, H. Weller, V. Werner, and A. Zilges, *The decay pattern of the Pygmy Dipole Resonance of ^{140}Ce,* Physics Letters B **756**, 72 (2016)

[119] E. G. Lanza, A. Vitturi, and M. V. Andrés, *Microscopic nuclear form factors for the pygmy dipole resonance,* Physical Review C **91**, 054607 (2015)

[120] G. Satchler, *Direct Nuclear Reactions* (Oxford University Press, 1983)

[121] E. G. Lanza, private communication (2022)

[122] M. Spieker, A. Heusler, B. A. Brown, T. Faestermann, R. Hertenberger, G. Potel, M. Scheck, N. Tsoneva, M. Weinert, H. F. Wirth, and A. Zilges, *Accessing the Single-Particle Structure of the Pygmy Dipole Resonance in ^{208}Pb,* Physical Review Letters **125**, 102503 (2020)

[123] E. J. Schneid, A. Prakash, and B. L. Cohen, *(D,P) and (D,T) Reactions on the Isotopes of Tin,* Physical Review **156**, 1316 (1967)

[124] R. Chapman, M. Hyland, J. L. Durell, J. N. Mo, M. Macphail, H. Sharma, and N. H. Merrill, *Neutron Orbit Sizes in the Isotopes of Tin*, Nuclear Physics A **316**, 40 (1979)

[125] N. Tsoneva and H. Lenske, *Pygmy dipole resonances in the tin region,* Phys. Rev. C **77**, 024321 (2008)

[126] B. P. Abbot *et al.*, *Multi-messenger Observations of a Binary Neutron Star Merger*, Astrophysical Journal Letters **848**, L12 (2017)

[127] A. Krumbholz, P. von Neumann-Cosel, T. Hashimoto, A. Tamii, T. Adachi, C. Bertulani, H. Fujita, Y. Fujita, E. Ganioglu, K. Hatanaka, C. Iwamoto, T. Kawabata, N. Khai, A. Krugmann, D. Martin, H. Matsubara, R. Neveling, H. Okamura, H. Ong, I. Poltoratska, V. Ponomarev, A. Richter, H. Sakaguchi, Y. Shimbara, Y. Shimizu, J. Simonis, F. Smit, G. Susoy, J. Thies, T. Suzuki, M. Yosoi, and J. Zenihiro, *Low-energy electric dipole response in ^{120}Sn,* Physics Letters B **744**, 7 (2015)

[128] D. Vretenar, N. Paar, P. Ring, and G. A. Lalazissis, *Pygmy dipole resonances in the relativistic random phase approximation,* Physical Review C **63**, 047301 (2001)

[129] D. Vretenar, Y. F. Niu, N. Paar, and J. Meng, *Low-energy isovector and isoscalar dipole response in neutron-rich nuclei,* Physical Review C **85**, 044317 (2012)

[130] X. Roca-Maza, G. Pozzi, M. Brenna, K. Mizuyama, and G. Colò, *Low-lying dipole response: Isospin character and collectivity in ^{68}Ni, ^{132}Sn, and ^{208}Pb,* Physical Review C **85**, 024601 (2012)

[131] N. Tsoneva, private communication (2022)

[132] M. Müllenmeister, *Systematic Investigation of the low energy electric dipole response in ^{116,118}Sn using the $(d, p\gamma)$ reaction*, Master's thesis, Institute for Nuclear Physics, University of Cologne (2022)

[133] M. Spieker, private communication (2022)

[134] B. Manning, G. Arbanas, J. A. Cizewski, R. L. Kozub, S. Ahn, J. M. Allmond, D. W. Bardayan, K. Y. Chae, K. A. Chipps, M. E. Howard, K. L. Jones, J. F. Liang, M. Matos, C. D. Nesaraja, F. M. Nunes, P. D. O'Malley, S. D. Pain, W. A. Peters, S. T. Pittman, A. Ratkiewicz, K. T. Schmitt, D. Shapira, M. S. Smith, and L. Titus, *Informing direct neutron capture on tin isotopes near the N=82 shell closure,* Physical Review C **99**, 041302(R) (2019)

[135] G. Potel, private communication (2022)

[136] M. Markova, P. von Neumann-Cosel, A. C. Larsen, S. Bassauer, A. Görgen, M. Guttormsen, F. L. Bello Garrote, H. C. Berg, M. M. Bjørøen, T. Dahl-Jacobsen, T. K. Eriksen, D. Gjestvang, J. Isaak, M. Mbabane, W. Paulsen, L. G. Pedersen, N. I. Pettersen, A. Richter, E. Sahin, P. Scholz, S. Siem, G. M. Tveten, V. M. Valsdottir, M. Wiedeking, and F. Zeiser, *Comprehensive Test of the Brink-Axel Hypothesis in the Energy Region of the Pygmy Dipole Resonance,* Physical Review Letters **127**, 182501 (2021)

[137] H. Kleis, *Lebensdaueranalyse angeregter Zustände in ^{57}Mn*, Bachelor's thesis, Institute for Nuclear Physics, University of Cologne (2022)

[138] E. Gaßmus, *Lebensdaueranalyse angeregter Zustände in ^{57}Fe*, Bachelor's thesis, Institute for Nuclear Physics, University of Cologne (2022)

[139] R. Burggraf, *Vorläufige Analyse einer Lebensdauermessung in ^{59}Ni*, Bachelor's thesis, Institute for Nuclear Physics, University of Cologne (2022)

[140] P. Koch, *Lifetime Measurements for ^{166}Dy*, Master's thesis, Institute for Nuclear Physics, University of Cologne (2022)

[141] A. Harter *et al.*, *In Preparation,* Nucl. Instr. Meth. A (2022)

[142] A. Esmaylzadeh *et al.*, *Investigation of γ-softness: Lifetime measurements in ^{104,106}Ru,* Submitted to Physical Review C (2022)

[143] A. Dewald, O. Möller, and P. Petkov, *Developing the Recoil Distance Doppler-Shift technique towards a versatile tool for lifetime measurements of excited nuclear states,* Prog. Part. Nucl. Phys. **67**, 786 (2012)

[144] C. Fransen, private communication (2022)

[145] J. M. Régis, T. Materna, S. Christen, C. Bernards, N. Braun, G. Breuer, C. Fransen, S. Heinze, J. Jolie, T. Meersschaut, G. Pascovici, M. Rudigier, L. Steinert, S. Thiel, N. Warr, and K. O. Zell, *Sub-nanosecond lifetime measurements using the Double Orange Spectrometer at the cologne 10 MV Tandem accelerator,* Nucl. Instr. Meth. A **606**, 466 (2009)

[146] A. Harter, L. Knafla, G. Frießner, G. Häfner, J. Jolie, A. Blazhev, A. Dewald, F. Dunkel, A. Esmaylzadeh, C. Fransen, V. Karayonchev, K. Lawless, M. Ley, J.-M. Régis, and K. O. Zell, *Lifetime measurements in the tungsten isotopes* $^{176,178,180}W$, Physical Review C **106**, 024326 (2022)

[147] L. Netterdon, V. Derya, J. Endres, C. Fransen, A. Hennig, J. Mayer, C. Müller-Gatermann, A. Sauerwein, P. Scholz, M. Spieker, and A. Zilges, *The γ-ray spectrometer HORUS and its applications for nuclear astrophysics,* Nucl. Instr. Meth. A **754**, 94 (2014)

[148] F. Heim, J. Mayer, M. Müller, P. Scholz, M. Weinert, and A. Zilges, *Experimental techniques to study the γ process for nuclear astrophysics at the Cologne accelerator laboratory,* Nucl. Instr. Meth. A **966**, 163854 (2020)

[149] J. M. Régis, H. Mach, G. S. Simpson, J. Jolie, G. Pascovici, N. Saed-Samii, N. Warr, A. Bruce, J. Degenkolb, L. M. Fraile, C. Fransen, D. G. Ghita, S. Kisyov, U. Koester, A. Korgul, S. Lalkovski, N. Mărginean, P. Mutti, B. Olaizola, Z. Podolyak, P. H. Regan, O. J. Roberts, M. Rudigier, L. Stroe, W. Urban, and D. Wilmsen, *The generalized centroid difference method for picosecond sensitive determination of lifetimes of nuclear excited states using large fast-timing arrays,* Nucl. Instr. Meth. A **726**, 191 (2013)

[150] A. Harter, private communication (2022)

[151] J. M. Régis, N. Saed-Samii, M. Rudigier, S. Ansari, M. Dannhoff, A. Esmaylzadeh, C. Fransen, R. B. Gerst, J. Jolie, V. Karayonchev, C. Müller-Gatermann, and S. Stegemann, *Reduced γ-γ Time walk to below 50 ps using the multiplexed-start and multiplexed-stop fast-timing technique with LaBr3(Ce) detectors,* Nucl. Instr. Meth. A **823**, 72 (2016)

[152] CAEN S.p.A., *User Manual UM2792 - V1730/VX1730 & V1725/VX1725*, https://www.caen.it/ (Rev. 6, May 2021)

[153] CAEN S.p.A., *User Manual UM6875 - V1782 Octal Digital MCA*, https://www.caen.it/ (Rev. 3, December 2021)

[154] CAEN S.p.A., *User Manual UM5175 - V2495/VX2495*, https://www.caen.it/ (Rev. 3, August 2019)

[155] CAEN S.p.A., *SciCompiler* User Firmware Generator, https://www.caen.it/products/sci-compiler/ (2018)

[156] M. Mayer, U. Friman-Gayer, J. Kleemann, O. Papst, *et al.*, *hdtv* Nuclear Spectrum Analysis Tool, https://github.com/janmayer/hdtv (2022)

[157] M. Weinert, *nd-buildevents* Eventbuilding Software for NuDAQ, https://gitlab.ikp.uni-koeln.de/mweinert/nd-buildevents (2022)

[158] N. Saed-Samii and A. Harter, *socov2* Eventbuilding and Analysis Software, https://gitlab.ikp.uni-koeln.de/nima/soco-v2 (2022)

[159] J. Mayer, *soco2root* ROOT-Tree Converter for socov2 Events, https://gitlab.ikp.uni-koeln.de/jmayer/soco2root (2018)

[160] CAEN S.p.A., *User Manual UM5960 - CoMPASS Multiparametric DAQ Software for Physics Applications*, https://www.caen.it/ (Rev. 19, July 2022)

[161] XIA LLC, *User's Manual - Digital Gamma Finder DGF-4C Rev. F, v4.03* (2009)

[162] M. Weinert, *nd-coinc-config* Multiplicity Filter and Veto Firmware for the CAEN V2495, https://gitlab.ikp.uni-koeln.de/mweinert/nd_coinc_config (2021)

[163] CAEN S.p.A., *User Manual UM6769 - 724-781-782 DPP-PHA Register Description and Data Format*, https://www.caen.it/ (Rev. 4, August 2022)

[164] CAEN S.p.A., *User Manual UM5678 - 725-730 DPP-PHA Register Description and Data Format*, https://www.caen.it/ (Rev. 3, June 2021)

[165] CAEN S.p.A., *User Manual UM4380 - 725 and 730 DPP-PSD Register Description and Data Format*, https://www.caen.it/ (Rev. 6, April 2020)

[166] S. Herb, *Developments at the Cologne 10 MV AMS system for ^{60}Fe measurements*, Ph.D. thesis, University of Cologne (2022)

Danksagung

Wie im Zitat am Anfang dieser Arbeit beschrieben, so ist nichts wirklich neu und alles geht aus dem hervor, was vorher war. Deshalb möchte ich mich bei denen bedanken, die mir den Weg auf meiner Reise bereiteten, oder ihn mit mir bestritten haben.

Ich möchte mich bedanken bei Prof. Dr. Andreas Zilges, der es geschafft hat das wunderbare Klima in seiner Arbeitsgruppe über Jahre aufrecht zu halten und zu pflegen. In dieser kollegialen und anspornenden Umgebung durfte ich nun fast zehn Jahre lernen, ausprobieren, wachsen, und weitergeben was mir einmal beigebracht wurde. Ich hatte stets die Freiheit meinen Interessen und meiner Intuition nachzugehen, wodurch ich viele Dinge lernen konnte, die in keinem Lehrplan stehen. Ich bereue keine Nacht im Labor, keinen Probevortrag, und schon gar kein Eisstockschießen. Danke Azi.

Bei Prof. Dr. Peter Reiter bedanke ich mich für die Begutachtung meiner Dissertation.

Ich bedanke mich bei Prof. Dr. Stephan Schlemmer für den Vorsitz meiner Disputation und das ehrliche Interesse an meiner Arbeit.

Bei allen Professoren und Verantwortlichen des Instituts bedanke ich mich für das entgegengebrachte Vertrauen und die freie Hand bei der Entwicklung des neuen Datenaufnahme-Systems.

Ich bedanke mich bei Dr. Mark Spieker, der mich oft angespornt hat die Dinge vernünftig zu machen, mich nicht in Details zu verlieren, und der ein gutes Auge für die wichtigen Details hatte. Bei ihm in der Lehre gewesen zu sein war nicht immer leicht, aber ich bin froh ihn zu meinen Mentoren zählen zu können.

Ein besonderer Dank gebührt meinem langjährigen Hotelzimmer-Kollegen und Freund Dr. Philipp Scholz, dessen musikalische und tatkräftige Unterstützung mir immer in Erinnerung bleiben werden. Ob in hitzigen Grundsatzdiskussionen oder in den lyrisch-melankolischen Momenten, im Labor oder auf Reisen, es war mir immer eine große Freude Zeit mit ihm zu verbringen. Ich hoffe, dass wir uns noch lange erhalten bleiben.

Ich bedanke mich bei Dr. Julius Wilhelmy, mit dem ich mir viele Jahre ein Büro sowie die Aufs und Abs der Promotion teilen durfte. Er hat mich in Kontakt mit Gregory Potel gebracht, und so den Stein ins Rollen gebracht der einen Großteil meiner Arbeit ausgemacht hat. Danke für die vielen wichtigen Diskussionen, die geteilten Meinungen über Musik und Mode, sowie die gemeinsame Neigung zum Kaffeekonsum.

Ich bedanke mich bei M. Sc. Miriam Müscher, die meine Verbindung zur Kernresonanzfluoreszenz war und deren akribische Arbeit auch meine Ergebnisse bereichern. Danke, dass ich so gut mit dir zusammenarbeiten konnte, mein eigenes Verständnis in unseren

Diskussionen verbessern konnte, und für die Versorgung mit den leckersten Keksen.

Bei Dr. Felix Heim bedanke ich mich für seine geleistete Arbeit als Assistent in den letzten Jahren. Sein starker Sportsgeist und sein Händchen für effizienztes Arbeiten halfen ihm die vielen organisatiorischen und wissenschaftlichen Aufgaben zu meistern, wovon die gesamte Gruppe profitiert hat.

Bei Dr. Lars Netterdon bedanke ich mich für die Korrektur meiner Arbeit, die gemeinsame Zeit in der Astrokammer, und die anhaltend gute Nachbarschaft.

Ich bedanke mich bei allen ehemaligen und derzeitigen Mitgliedern der AG, die den Spirit aufrecht halten und die mir in den letzten Jahren ein wundervolles Umfeld waren.

Ich bedanke mich ber Dr. Johann Isaak aus Darmstadt für die Unterstützung bei der Auswertung, die schöne Zeit in Japan, und den guten Kontakt.

I am sincerely grateful for the collaboration with Prof. Dr. Muhsin N. Harakeh from Groningen. My work gained a lot from the scientific efforts he has made over decades and his tireless contribution to conferences and collaborations.

Ich möchte mich bei den stets hilfsbereiten Mitarbeitenden der Feinmechanik-Werkstatt und der Elektronik-Werkstatt, sowie den Operateuren im Beschleunigerbereich bedanken. Ohne ihre zuverlässige Arbeit wäre die Forschung in unserem Institut unmöglich.

Bei Dr. Christoph Fransen bedanke ich mich für seine unermüdliche Arbeit in vielen Bereichen, vor allem unter den erschwerten Bedingungen der letzten zwei Jahre.

Bei allen ehemaligen und derzeiten SysOps bedanke ich mich für die exzellente Infrastruktur und die viele unsichtbare Arbeit.

Ich möchte mich bei Daniel Förster bedanken, den ich seit langer Zeit zu meinen engsten Freunden zählen kann. Die vielen gemeinsamen Jahre und Erlebnisse mit dir haben mein Leben bereichert und werden immer ein Teil meiner Geschichte sein. Danke, dass es dich gibt.

Ganz am Anfang meiner Geschichte stehen meine Eltern, denen ich unendlich dankbar bin für die nie endende Unterstützung, das stets offene Ohr, die lange Leine, und die Gewissheit, dass sie immer da sind. Ihr habt mir all das ermöglicht, was mich heute ausmacht.

Während der für mich schweren Zeit in der Pandemie und unserer gemeinsamen Abgabephase war ein besonderer Mensch stets für mich da. Mit meiner Partnerin Susan gehe ich nun schon ein paar Jahre Hand in Hand durch's Leben und bei jedem Schritt rücken wir näher aneinander. Ich habe viel von dir gelernt und bin dir unendlich Dankbar für die schöne Zeit, deine Unterstützung, und deine Ehrlichkeit.